192

Finite Element Modelling for Marine Electromagnetic Petroleum Exploration

by

Trevor T. M. Boyce

Department of Geological Sciences
University of Manitoba
Winnipeg, MB

A Thesis
submitted to Graduate Studies
in Partial Fulfilment of the requirements
for the Degree of

MASTER OF SCIENCE
at the University of Manitoba

ISBN 0-612-12996-9

Name _____

Dissertation Abstracts International and *Masters Abstracts International* are arranged by broad, general subject categories. Please select the one subject which most nearly describes the content of your dissertation or thesis. Enter the corresponding four-digit code in the spaces provided.

GEOPHYSICS
SUBJECT TERM

0373
SUBJECT CODE

UMI

Subject Categories

THE HUMANITIES AND SOCIAL SCIENCES

COMMUNICATIONS AND THE ARTS
Architecture 0729
Art History 0377
Cinema 0900
Dance 0378
Fine Arts 0357
Information Science 0723
Journalism 0391
Library Science 0399
Mass Communications 0708
Music 0413
Speech Communication 0459
Theater 0465

EDUCATION
General 0515
Administration 0514
Adult and Continuing 0516
Agricultural 0517
Art 0273
Bilingual and Multicultural 0282
Business 0688
Community College 0275
Curriculum and Instruction 0727
Early Childhood 0518
Elementary 0524
Finance 0277
Guidance and Counseling 0519
Health 0680
Higher 0745
History of 0520
Home Economics 0278
Industrial 0521
Language and Literature 0279
Mathematics 0280
Music 0522
Philosophy of 0998
Physical 0523
Psychology 0525
Reading 0535
Religious 0527
Sciences 0714
Secondary 0533
Social Sciences 0534
Sociology of 0340
Special 0529
Teacher Training 0530
Technology 0710
Tests and Measurements 0288
Vocational 0747

LANGUAGE, LITERATURE AND LINGUISTICS
Language
- General 0679
- Ancient 0289
- Linguistics 0290
- Modern 0291

Literature
- General 0401
- Classical 0294
- Comparative 0295
- Medieval 0297
- Modern 0298
- African 0316
- American 0591
- Asian 0305
- Canadian (English) 0352
- Canadian (French) 0355
- English 0593
- Germanic 0311
- Latin American 0312
- Middle Eastern 0315
- Romance 0313
- Slavic and East European 0314

PHILOSOPHY, RELIGION AND THEOLOGY
Philosophy 0422
Religion
- General 0318
- Biblical Studies 0321
- Clergy 0319
- History of 0320
- Philosophy of 0322

Theology 0469

SOCIAL SCIENCES
American Studies 0323
Anthropology
- Archaeology 0324
- Cultural 0326
- Physical 0327

Business Administration
- General 0310
- Accounting 0272
- Banking 0770
- Management 0454
- Marketing 0338

Canadian Studies 0385
Economics
- General 0501
- Agricultural 0503
- Commerce-Business 0505
- Finance 0508
- History 0509
- Labor 0510
- Theory 0511

Folklore 0358
Geography 0366
Gerontology 0351
History
- General 0578
- Ancient 0579
- Medieval 0581
- Modern 0582
- Black 0328
- African 0331
- Asia, Australia and Oceania 0332
- Canadian 0334
- European 0335
- Latin American 0336
- Middle Eastern 0333
- United States 0337

History of Science 0585
Law 0398
Political Science
- General 0615
- International Law and Relations 0616
- Public Administration 0617

Recreation 0814
Social Work 0452
Sociology
- General 0626
- Criminology and Penology ... 0627
- Demography 0938
- Ethnic and Racial Studies 0631
- Individual and Family Studies 0628
- Industrial and Labor Relations 0629
- Public and Social Welfare 0630
- Social Structure and Development 0700
- Theory and Methods 0344

Transportation 0709
Urban and Regional Planning 0999
Women's Studies 0453

THE SCIENCES AND ENGINEERING

BIOLOGICAL SCIENCES
Agriculture
- General 0473
- Agronomy 0285
- Animal Culture and Nutrition 0475
- Animal Pathology 0476
- Food Science and Technology 0359
- Forestry and Wildlife 0478
- Plant Culture 0479
- Plant Pathology 0480
- Plant Physiology 0817
- Range Management 0777
- Wood Technology 0746

Biology
- General 0306
- Anatomy 0287
- Biostatistics 0308
- Botany 0309
- Cell 0379
- Ecology 0329
- Entomology 0353
- Genetics 0369
- Limnology 0793
- Microbiology 0410
- Molecular 0307
- Neuroscience 0317
- Oceanography 0416
- Physiology 0433
- Radiation 0821
- Veterinary Science 0778
- Zoology 0472

Biophysics
- General 0786
- Medical 0760

EARTH SCIENCES
Biogeochemistry 0425
Geochemistry 0996
Geodesy 0370
Geology 0372
Geophysics 0373
Hydrology 0388
Mineralogy 0411
Paleobotany 0345
Paleoecology 0426
Paleontology 0418
Paleozoology 0985
Palynology 0427
Physical Geography 0368
Physical Oceanography 0415

HEALTH AND ENVIRONMENTAL SCIENCES
Environmental Sciences 0768
Health Sciences
- General 0566
- Audiology 0300
- Chemotherapy 0992
- Dentistry 0567
- Education 0350
- Hospital Management 0769
- Human Development 0758
- Immunology 0982
- Medicine and Surgery 0564
- Mental Health 0347
- Nursing 0569
- Nutrition 0570
- Obstetrics and Gynecology .. 0380
- Occupational Health and Therapy 0354
- Ophthalmology 0381
- Pathology 0571
- Pharmacology 0419
- Pharmacy 0572
- Physical Therapy 0382
- Public Health 0573
- Radiology 0574
- Recreation 0575
- Speech Pathology 0460
- Toxicology 0383

Home Economics 0386

PHYSICAL SCIENCES
Pure Sciences
Chemistry
- General 0485
- Agricultural 0749
- Analytical 0486
- Biochemistry 0487
- Inorganic 0488
- Nuclear 0738
- Organic 0490
- Pharmaceutical 0491
- Physical 0494
- Polymer 0495
- Radiation 0754

Mathematics 0405
Physics
- General 0605
- Acoustics 0986
- Astronomy and Astrophysics 0606
- Atmospheric Science 0608
- Atomic 0748
- Electronics and Electricity 0607
- Elementary Particles and High Energy 0798
- Fluid and Plasma 0759
- Molecular 0609
- Nuclear 0610
- Optics 0752
- Radiation 0756
- Solid State 0611

Statistics 0463

Applied Sciences
Applied Mechanics 0346
Computer Science 0984
Engineering
- General 0537
- Aerospace 0538
- Agricultural 0539
- Automotive 0540
- Biomedical 0541
- Chemical 0542
- Civil 0543
- Electronics and Electrical 0544
- Heat and Thermodynamics ... 0348
- Hydraulic 0545
- Industrial 0546
- Marine 0547
- Materials Science 0794
- Mechanical 0548
- Metallurgy 0743
- Mining 0551
- Nuclear 0552
- Packaging 0549
- Petroleum 0765
- Sanitary and Municipal 0554
- System Science 0790

Geotechnology 0428
Operations Research 0796
Plastics Technology 0795
Textile Technology 0994

PSYCHOLOGY
General 0621
Behavioral 0384
Clinical 0622
Developmental 0620
Experimental 0623
Industrial 0624
Personality 0625
Physiological 0989
Psychobiology 0349
Psychometrics 0632
Social 0451

THE UNIVERSITY OF MANITOBA

FACUTY OF GRADUATE STUDIES

COPYRIGHT PERMISSION

FINITE ELEMENT MODELLING FOR MARINE ELECTROMAGNETIC PETROLEUM EXPLORATION

BY

TREVOR T.M. BOYCE

A Thesis/Practicum submitted to the Faculty of Graduate Studies of the University of Manitoba in partial fulfillment of the requirements for the degree of

MASTER OF SCIENCE

Abstract

Controlled-source EM surveys are logistically complex and expensive to perform in a marine environment. Therefore, numerical design studies are needed before an experimental survey is considered, both to examine the feasibility of the method as an exploration tool and to provide estimates of the signal levels to be expected.

A finite-element numerical modelling computer program is used to calculate the time-domain electric and magnetic field responses to several petroleum-relavent 2-D conductivity models. These models include single or multiple layers, faults, stratigraphic changes, and near-surface resistive layers. The EM system employed consists of a horizontal electric source-dipole and inline horizontal electric and magnetic field receivers oriented perpendicular to the source-dipole. The finite element program solves an EM boundary value problem based on the governing Maxwell's equations in the Laplace s, and wavenumber q domains. The fields are transformed back to the time and space-domains via an inverse Laplace transform and cosine and sine transforms respectively. The response curves for the electric and magnetic fields are analyzed to determine the sensitivity of the system to various model conductivity structures.

Generally, the modelling results show that the CSEM system modelled is more sensitive to conductivity structures with large vertical extent than to thin, layered structures. The results also show a greater sensitivity to near-surface structures than to deep ones. In particular, the CSEM system is capable of resolving whether a discontinuity in conductivity is present across a subsurface fault, provided that the displacement on the fault is comparable to the fault depth. In contrast, relatively small changes in conductivity due to changes in stratigraphy appear to have virtually no affect on the EM response. The most promising target in terms of hydrocarbon exploration appears to be near-surface resistive zones, which have a large EM response, making the determination of the location and size of the zone possible. A resistive layer can be created by hydrocarbon induced alteration or gas hydrates; both are of recent interest in hydrocarbon exploration. To detect such a resistive zone, a source dipole moment of 10^4 A.m, an electric receiver with length of 100 m, and an induction coil sampling the fields at 100 Hz are sufficient.

Acknowledgements

I would like to take this opportunity to recognize and thank a number of people for their contributions to this thesis. Firstly, I express my deep thanks to Dr. Ian J. Ferguson for his support, constructive comments and patience over the years. His excellence as an M.Sc. thesis advisor and Shortstop in baseball are appreciated. I would also like to thank Dr. Wooil Moon (Geol. Sc.), Dr. Bill Last (Geol. Sc.), and Dr. Abdel Sebak (Elect. Eng.) for taking time out of their busy schedules to be a part of my examining committee.

I thank Dr. Mark Everett for providing me with a copy of the computer code for his finite element program that was used as the modelling vehicle for this thesis. I would also like to acknowledge the High Performance Computing Centre and Fujitsu Canada in Calgary, Alberta for their generous support in the form of a scholarship of free computer time on their Fujitsu VPX240/10 supercomputer.

In my years as a grad student, I enjoyed great geological discussions and many fun times with my fellow grads; Henry Odwar, Eli Kostelnyk, Dan MacDonald Kyla Arden, Lisa Sack, John Rayburn, and Pascal Gervais.

I thank Dr. M. Rayburn for his generosity in lending a copy of his LaTeX software to me, allowing for the quality of the typesetting in the thesis. I would also like to thank Samson Canada for providing me clear motivation for putting the finishing touches on the thesis.

Many thanks to my parents for their undying support throughout my education. Lastly, and most importantly, I would like to express my sincere gratitude to my wife Lorelei for putting up with me and not giving up on me while I was working on my research.

Table of Contents

List of Figures and Tables

Chapter 2

Chapter 3

Chapter 4

Chapter 5

Chapter 6

Chapter 7

Chapter 8

Table of Acronyms

Electromagnetic Terms

EM	**E**lectro**M**agnetic
CS	**C**ontrolled-**S**ource
NS	**N**atural-**S**ource
CSEM	**C**ontrolled-**S**ource **E**lectro**M**agnetics
MT	**M**agneto**T**ellurics
CSAMT	**C**ontrolled-**S**ource **A**udio-**F**requency **M**agneto**T**ellurics
ZSBZ	**Z**ondirovanie **S**tanovleniem polia v **B**lizhned **Z**one -Russian system
IP	**I**nduced **P**olarization
ERER	Inline electric dipole-dipole survey system
HRHR	Inline magnetic dipole-dipole survey system
HED	**H**orizontal **E**lectric **D**ipole
HMD	**H**orizontal **M**agnetic **D**ipole
SQUID	**S**uperconducting **QU**antum **I**nterference **D**evice

Numerical Terms

PDE	**P**artial **D**ifferential **E**quation
BVP	**B**oundary **V**alue **P**roblem
FE	**F**inite **E**lement
SA	**S**emi-**A**nalytic
GS	**G**aver-**S**tehfest
NAG	**N**umerical **A**lgorithms **G**roup (software library)

Other Terms

MOR	**M**id-**O**cean **R**idge
DHS	**D**ouble **H**alf-**S**pace
LHS	**L**ayered **H**alf-**S**pace
cph	**c**ycles **p**er **h**our

Table of Symbols

b_y, ie_y	Magnetic and electric fields in the wavenumber domain
$\mathbf{B}_y$, $\mathbf{E}_y$	Magnetic and electric fields in the y-domain
$\mathbf{B}_y$, $\mathbf{E}_y$	Time derivitive of magnetic and electric fields in the y-domain
$\mathbf{J}_S$	Applied (source) current density
$\mathbf{J}_D$	Displacement current density
ϵ_0	Permittivity of free space
μ_0	Permeability of free space
Ω	FE solution domain
h	FE mesh triangle size
q	Wavenumber in the along-strike direction
s	Laplace frequency

Chapter 1

Introduction

1.1 Introduction

The objective of many geophysical methods is to determine, through remote measurement, the physical properties of the Earth's subsurface. These measurements are important not only in the purely scientific sense, but also in the exploration for economic minerals and hydrocarbons since the vast majority of such deposits are beneath the surface. The detection of these deposits depends on the characterisitic physical properties which differentiate them from the surrounding media (*e.g.* density, electrical conductivity). The most common tools used by geophysicists are the seismic, gravity, magnetic, and electromagnetic methods which detect the elastic properties, density, magnetic, and electrical properties of the Earth's subsurface, respectively. In all cases, useful information is provided to aid in determining the most favourable places for locating the deposits being sought.

Most electromagnetic (EM) geophysical methods involve the propagation of time-varying electromagnetic fields in and over the earth for the purpose of determining its electrical conductivity. These fields may have natural or artificial (man-made) sources. Natural source (NS) EM fields may be generated by the variations in ionospheric and magnetospheric currents caused by solar emissions, aurora, and thunderstorms. These ionospheric currents induce current flow in the earth. Controlled-source (CS) EM sys-

tems use an artificial energy source to induce current flow in the earth.

Historically, CSEM methods have been employed mainly in the mining industry to find metallic ore deposits which often have large contrasts in electrical properties with respect to the country rock (*e.g.* Ward, 1980). To date, the mining industry uses mostly land-based systems. Relatively recently, land-based CSEM has found application in petroleum exploration (Nekut & Spies, 1989).

The application of CSEM techniques to the marine environment was first examined by Bannister (1968). Since then, three groups have emerged in the study of seafloor CSEM; Cambridge University (UK), University of Toronto/Pacific Geoscience Centre (Canada), and Scripps Institute of Oceanography (USA). More recently, these schools have generated large quantities of background theory for both frequency domain (*e.g.* Unsworth *et al.*, 1993; Chave & Cox, 1982) and time domain (*e.g.* Cheesman *et al.*, 1987) seafloor CSEM methods.

In the last few years, these groups have reported results of experiments which successfully mapped the seafloor conductivity using both frequency domain (Evans *et al.*, 1991; Cox *et al.*, 1986; Young & Cox, 1981) and time domain systems (Webb *et al.*, 1993; Cheesman *et al.*, 1990). These surveys have included studies at the East Pacific Rise to determine the conductivity structure of the upper several kilometres of both newly formed and 100 000 year old oceanic crust (Evans *et al.*, 1991), and to place constraints on rise crest thermal models (Young & Cox, 1981). Surveys near the Juan de Fuca Ridge have been conducted to determine the conductivity of the 20-30 m of sediment overlying the basaltic basement (Webb *et al.*, 1993; Cheesman *et al.*, 1990). However, examination of the literature dealing with marine CSEM techniques indicates very little work has been done to study the feasibility of applying CSEM to hydrocarbon exploration at the seafloor. Investigation of this feasibility is the purpose of this thesis.

1.2 Motivation for this study

Seismic methods are the most common exploration technique used in the oil industry, accounting for about 95% of expenditures (*e.g.* Vozoff *et al.*, 1985). However, seismic methods are not always successful. For example, in areas with thick volcanic cover or highly complex structures, the seismic reflection technique often provides poor results (Keller, 1983). Considering the costs and difficulty of offshore hydrocarbon exploration, new methods must be sought as a compliment to the seismic technique. As the electromagnetic methods lack the resolution of the seismic reflection technique, it is unlikely that these methods will become a substitute for seismics, but they may provide useful information which may be applied in a combined interpretation with the seismic data.

There are numerous situations in which EM methods may be useful in land and marine soundings. One question that sometimes arises in oil exploration is whether or not a significantly thick layer of potentially petroliferous sedimentary rock exists beneath a surface cover of volcanic rock (Keller, 1983). Application of electric and electromagnetic methods is an obvious approach to explore the porous marine sedimentary rocks in which petroleum normally occurs since they are as much as two orders of magnitude more conductive than the overlying volcanic rocks (Palacky, 1987). Another important problem in oil exploration is the mapping of porosity variations in carbonates (Strack *et al.*, 1991). These lateral changes in porosity produce variations in the electrical conductivity which may be detectable by a surface electromagnetic method.

Petroleum reservoirs often occur at great depths, therefore it is necessary to use an electrical or EM method that is capable of penetrating to great depths. Two types of methods are available: the magnetotelluric (MT) method and the controlled-source electromagnetic methods. The magnetotelluric method is often used in areas that are

logistically difficult to obtain seismic data in order to map changes in subsurface conductivity to great depth (Orange, 1989). Controlled-source EM methods have not been tested as extensively as the MT method, but on theoretical grounds such methods should be able to offer the potential of higher precision and resolution (Keller, 1983).

Controlled-source EM surveys are logistically complex and expensive to perform in a marine environment. These surveys require the use of a large ocean-going ship for an extended period of time and many seafloor magnetic and electric field receivers, all of which are very costly. Therefore, numerical modelling is desirable before an experimental survey is considered, both to examine the feasibility of the method as an exploration tool for hydrocarbons and to provide some estimates on the signal levels to be expected at the EM receivers. The aim of this research is to use finite-element modelling to predict the EM fields which would be measured in realistic seafloor CSEM soundings, to investigate the sensitivity of the response to the underlying geological structure, and furthermore, to provide some constraints on the survey parameters for future seafloor EM surveys.

1.3 Outline of the Thesis

The following chapters examine the feasibility of using time domain CSEM as a tool for hydrocarbon exploration in a marine environment. A horizontal electric dipole (HED) will be used as the EM source. The theoretical response of several models to the HED source will be studied using a 2.5D forward modelling computer program written by Everett (1990). The program uses the finite element method to solve the governing vector EM diffusion equations at the sea-seafloor interface for the purpose of modelling the subsurface response to a selection of conductivity models.

In Chapter 2, I discuss marine electromagnetic methods in greater detail and pro-

vide a brief review of petroleum geology and the electrical conductivity of the marine environment. In Chapter 3, I review the past and present use of electromagnetic and electrical methods in hydrocarbon exploration to provide a framework for the marine EM modelling. In Chapter 4, I present the necessary electromagnetic theory and formulation of the 2D electromagnetic boundary value problem. Analytical solutions which may be used to test the accuracy of the computer modelling program are also presented in this chapter. In Chapter 5, I introduce the finite element method and the algorithm used to calculate the magnetic and electric fields in a 2D structure. The computer program implementing this algorithm is tested for accuracy on a double half-space. Results for this double half-space and a simple layered half-space are displayed. Results for three types of seafloor models are presented and discussed in Chapters 6, 7, and 8. Conclusions from the modelling are presented in Chapter 9.

Chapter 2

Marine EM and Petroleum Geology

2.1 Electrical Properties of Rock

The electrical properties of rock include the primary properties of conductivity (σ) and permittivity (ε), and secondary properties such as the coefficients which define the rate of change of the primary properties with frequency, temperature, pressure, etc. In the case of EM diffusion, the electrical conductivity is by far the most important (Keller, 1987). The electric conductivity is the measure of the abiltiy of rock (or any material) to permit the flow of electric current. The MKS unit for conductivity is Siemens per metre (Sm^{-1}). Electric conductivity is highly variable and may span many orders of magnitude in common materials (10^{-7} to 10^{5} Sm^{-1}). It is common, in geophysics, to use the reciprocal of conductivity, called resistivity (ρ), which is measured in Ohm-metres (Ω.m).

Minerals separate naturally into 2 groups; a) metallic conductors and semiconductors, and b) electrical insulators. The insulators are characterized by ionic bonding, thus the charge carrying ions must overcome large barrier potentials to move. These two types of conduction are briefly discussed below and in greater depth in Keller (1987).

Metallic conduction is the normal type of current flow in minerals containing free electrons, such as graphite (about 10^{8} Sm^{-1}), native copper (about 10^{7} Sm^{-1}), and arsenopyrite (about 10^{5} Sm^{-1}). Although minerals displaying metallic conduction are

rare, they can greatly effect the conductivity of a rock if present in even small quantities. Much more common and economically important than metals are the semiconductors (usually sulphides and oxides). Conduction in semiconductors requires some energy to drive the electrons into conduction bands. This energy may be provided by heating. Semiconductors generally have conductivities on the order of 10^{-4} to 10^{6} Sm^{-1}.

Most dry rocks are electrical insulators, with very high resistivity. In insulating materials, electrolytic conduction dominates. Electrolytic conduction in solids is the result of the displacement of ions from their normal position in the crystal lattice of a mineral. Such ions move through the crystal lattice when an electric field is applied. The flow of electric current by means of electrolytic conduction in solids, however, is very slow. A much more efficient and effective method of conduction is through an aqueous electrolyte (*e.g.* water).

In general, conduction in rocks is electrolytic and takes place through the fluid-filled pores and passages which are contained within the insulating rock matrix. Nearly all hydrocarbon reservoirs occur in unmetamorphosed sedimentary rocks, and most of them in sandstones, limestones, and dolostones (North, 1985). These rock types are porous, with porosities ranging from 5-30%. The porosity may range up to 40-85% for freshly deposited marine sediments (North, 1985). The pores of rocks are most often filled or partially filled with water. Since water is a polar solvent, in nature it often exists as an electrolyte with a wide variety of salts in solution. Although unmineralized water is a relatively poor conductor, the dissolved salts provide considerable amounts of ions which add to the conductivity of the water. The conductivity of the electrolytic solution is given by

$$\sigma_w = 96500 \sum C_i M_i \tag{2.1}$$

(McNeill, 1990) where C_i is the number of grams equivalent weight of i^{th} ion per m^3

of water, and M_i is the ionic mobility (the terminal velocity of the ions under a constant electric field) of the i^{th} ion ($m^2s^{-1}V^{-1}$). An empirical formula relating the conductivity of a water-saturated rock is Archie's law (Keller, 1987):

$$\sigma = a\sigma_w W^m \tag{2.2}$$

where σ is the rock conductivity, σ_w is the conductivity of the pore water, W is the volume fraction of pore water in the rock, and a and m are empirically determined constants which depend on the type of rock. If the pore volume in the rock is not completely filled with water, Archie's law is modified to

$$\sigma = a\sigma_w S^n \Phi^m \tag{2.3}$$

where S is the fraction of the pore spaces that is filled with water, Φ is the porosity of the rock and n is empirically determined. The conductivity of most water-bearing rocks ranges between 10^{-5} to 10^{-1} Sm^{-1}. In contrast, dry rocks have conductivities a few orders of magnitude smaller. Seawater has a conductivity of about 3.0-4.0 Sm^{-1}.

Figure 2.1 illustrates the typical conductivity ranges of sedimentary rocks in relation to other earth materials. The conductivity values given in figure 2.1 are meant mainly to indicate the relative resistivity of limestones, sandstones, and shales. However, clay-rich sedimentary rocks such as shales are always relatively conductive (0.2 to 0.03 Sm^{-1}) while sandstones and limestones may span several orders of magnitude. Most determinations of conductivity in sedimentary basins come from well-logging operations performed during exploration for oil and gas. An example of a resistivity log from an oil well in the North Sea is shown in figure 2.2. This figure shows that the shale units are approximately one order of magnitude more conductive than the sandstones. The water-saturation log shows that clay-rich shale is 100% water saturated, whereas the shaly sandstone with a medium clay content is only 60% water saturated and is therefore more

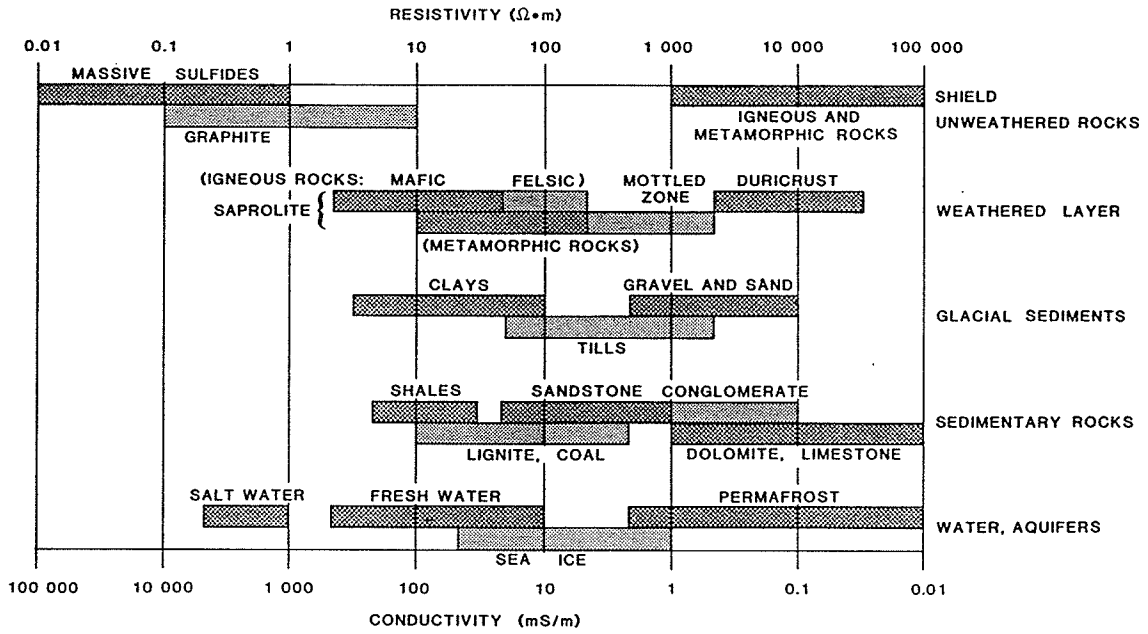

Figure 2.1 Typical ranges of conductivities of earth materials (from Palacky, 1987).

resistive (15 Sm^{-1}) than the shale. There is clearly a correlation between conductivity, water saturation and clay content.

2.2 Seafloor Electromagnetics

In terms of EM surveys, the marine environment is a world turned upside-down (Constable, 1990). The survey is carried out within the highly conducting sea for the purpose of studying the less conductive seafloor. This places some restrictions on the type of EM method that may be employed. The seafloor magnetotelluric (MT) method mentioned in Chapter 1 is a long established method which uses the naturally varying electric currents in the Earth's ionosphere as an energy source. Although MT can be used in shallow waters (Constable *et al.*, 1994), measurements made in a deeper marine environment are of limited use in determining the conductivity of the oceanic crust. Due to the presence of the overlying conductive ocean, the amplitude of all high frequency

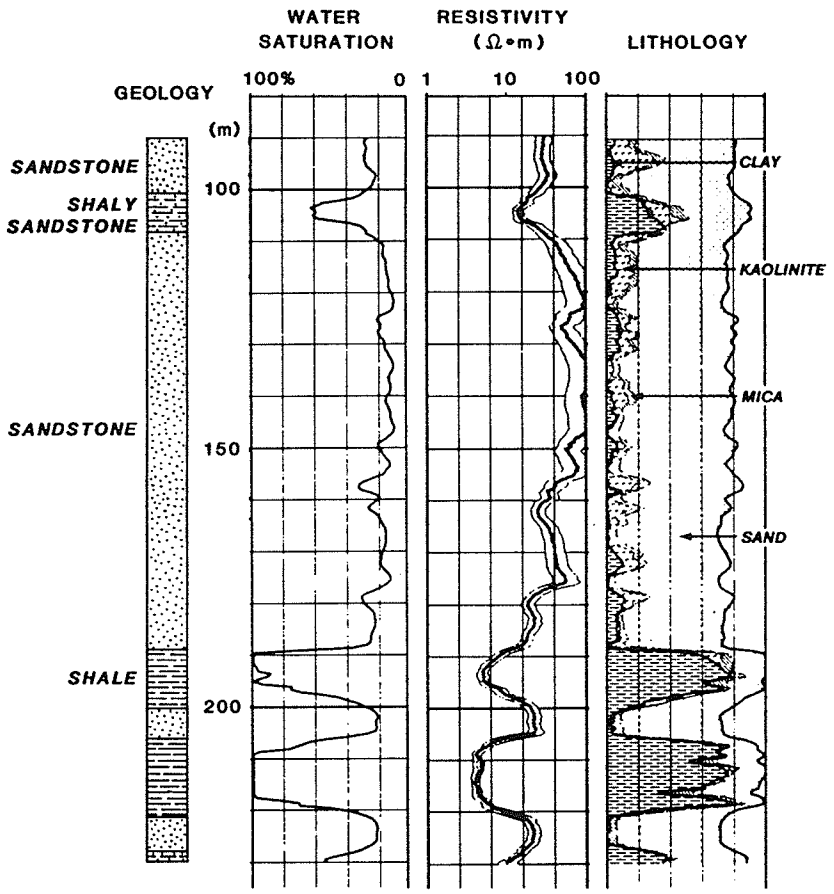

Figure 2.2 Log showing geology, resistivity, and water saturation of a portion of an oil well in the North Sea (from Palacky, 1987).

components ($>10^{-2}$ Hz) from the ionosphere are severely attenuated at the seafloor below a few thousand metres of seawater. In fact, for frequencies greater than 10^{-1} Hz, the electric and magnetic fields are reduced to about $0.1^{\%}$ (Constable, 1990). This leads to a limited MT frequency spectrum ($<10^{-2}$ Hz), which best resolves structure at upper mantle (>50 km) depths (Constable, 1990). However, the depth range that is of interest in petroleum exploration is about 500 m to 6 km (Tissot & Welte, 1978).

The conductive seafloor environment does have an advantage. Since the thick cover of conducting ocean acts to attenuate the natural EM signal from the ionosphere,

a very quiet EM environment is available for CSEM surveys (Chave *et al.*, 1991). To explore the conductivity structure of the upper oceanic crust, we must use a controlled EM source at the seafloor to generate the frequencies greater than 10^{-2} Hz.

2.3 Time-Domain CSEM Systems

Theoretically, an EM measurement in the frequency domain and the time domain can provide the same information. However, most electromagnetic theory for seafloor geophysical systems has been developed in the frequency domain (*e.g.* Bannister, 1968; Coggon & Morrison, 1970; Chave & Cox, 1982). In the frequency domain on land, measurements of the secondary EM fields (which result from the induction of currents in the earth by the primary fields) must be made in the presence of the primary field (fields propagating throught the air). These measurements are usually expressed as the amplitude change and phase shift relative to the primary field. To obtain an accurate assessment of the secondary fields, the primary field must be carefully removed from the total observed field. More recently, it has been recognized that there are practical advantages to work in the time domain. By transmitting a transient signal (a non-periodic signal, *e.g.* pulse or step function) the measurements may be made in the absence of the primary field, thus eliminating the problem of its removal. It has been found that less effort is required to record a single transient waveform than the frequency response for the many separate transmitted frequencies (Swift, 1987). One possible disadvantage is that time domain measurements can be wide-band and therefore more susceptible to noise which can be filtered out in frequency domain measurements.

Marine EM systems consist of a source antenna and one or more receiver antennae deployed on the seafloor. The receivers measure either the electric or magnetic fields induced in the Earth by the source. There are many types of marine EM system configu-

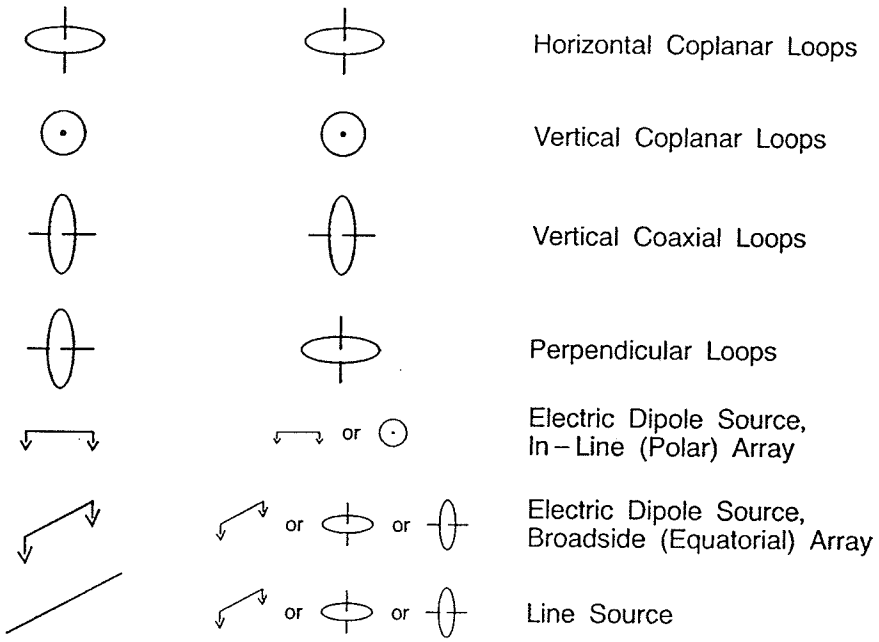

Figure 2.3 An example of several diffferent types of sources and receivers that may be used in a transient system (Spies & Frischneckt, 1991).The vertical coaxial loop system and the electric dipole source, in-line array are both commonly used in marine CSEM surveys.

rations possible, some of which are illustrated in figure 2.3. Two systems that have been found to be well suited for use on the seafloor are the ERER and HRHR configurations. The ERER system consists of a coaxial horizontal electric dipole (HED) source and receiver. The HRHR system consists of a coaxial horizontal magnetic dipole (HMD) source and receiver. These systems are suited to seafloor surveying as both systems generate and receive vertical as well as horizontal current flow (Cheesman *et al.*, 1987). The ERER system in particular is useful when trying to detect relatively thin horizontal resistive layers as the resistive layer deflects the electric field by electric charge build-up (Cheesman *et al.*, 1987).

Edwards and Chave (1986) computed the response of a relatively resistive crustal

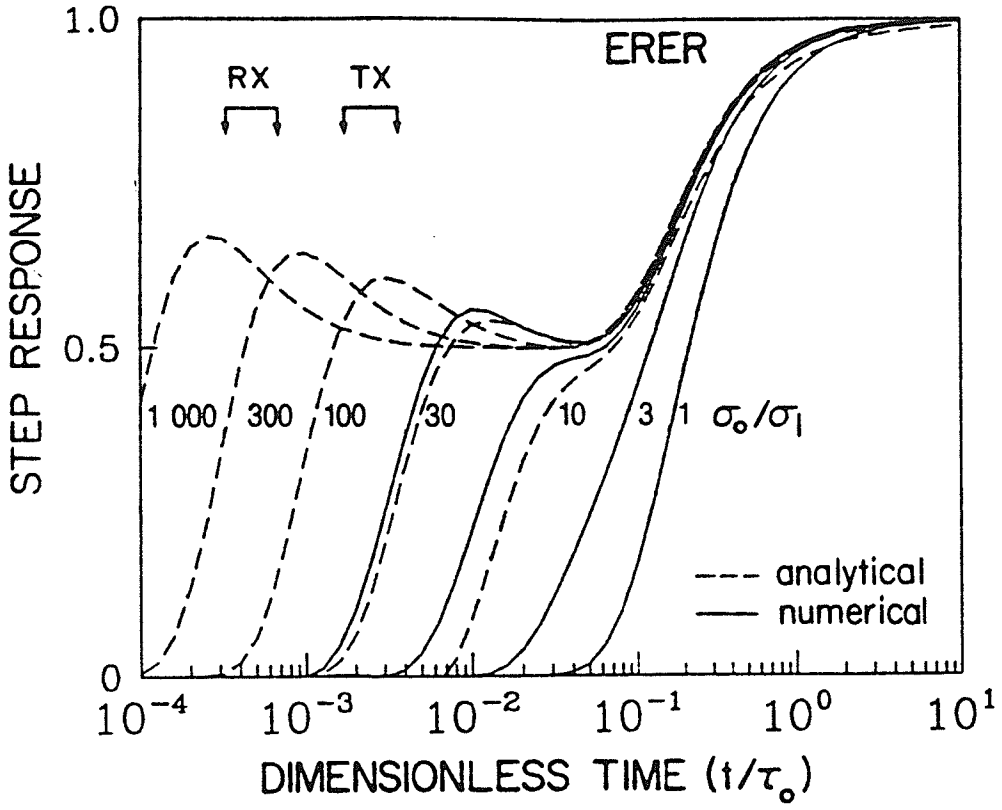

Figure 2.4 The step-on response of the ERER system for a range of values of the conductivity ratio between the seawater and the seafloor (from Cheesman *et al.*, 1987). The conductivity of seawater is denoted as σ_0, and the conductivity of the seafloor is σ_1. The response is normalized to the late time response.

half-space below a conductive half-space of seawater to a transient electric dipole-dipole (ERER) system. The electromagnetic fields diffuse outward from the transmitter much like a smoke ring (Nabighian, 1979). The "smoke rings" of induced current become less dense as the ring grows, but keep the same shape. The rate at which the fields diffuse through the seafloor and seawater is inversely proportional to the conductivity of the medium. Therefore, the first signal to reach the receiver is through the seafloor. A later signal arrives through the more conductive seawater. The step-response of the ERER system is plotted in figure 2.4 for different conductivity ratios between seafloor and seawater (Edwards & Chave, 1986). The fields have been normalized with respect

to the late time arrival through the seawater. The arrival time of the first signal varies with the seafloor conductivity and therefore it can be used to resolve the conductivity of the diffusion path through the seafloor.

2.4 CSEM Sources and Receivers

The system modelled in this thesis employs an HED (x-directed) for the source. An HED and an HMD are located at the seafloor to measure the electric and magnetic fields respectively. The receiver dipoles are oriented perpendicular to the source dipole (*i.e.* y-directed) to detect the transverse components of the electric and magnetic fields. The CSEM setup being employed is discussed in greater detail in §4.2 and shown in figure 4.1. Figure 2.5 shows a "plan view" of the electric and magnetic fields at the seafloor generated by the HED. Note how the horizontal y-component of the electric field is zero at y=0 whereas the y-component of the magnetic field is maximum at y=0. These plots help to indicate the locations to best place receivers with respect to the transmitter in a real survey.

In real seafloor EM surveys, the source dipole may be towed along the seafloor by a ship. One source dipole used in seafloor studies consists of an insulated armoured cable up to 1000 m in length coupled to the seafloor by 15 m of bared cable at the ends (*e.g.* Cox *et al.*, 1986). The dipole is energized with 50-100 A DC. Thus, the electric dipole moment of the source (the product of the current and dipole length) in a typical seafloor survey may be as large as 10^5 Am. However, since the strength of the source varies from survey to survey and may increase as technology advances, all the modelling in this thesis will employ a source with a unit dipole moment. It is then a simple task to scale the modelled field responses by the appropriate scale factor.

The receiver antenna for the electric field is an insulated electric wire up to 1000 m

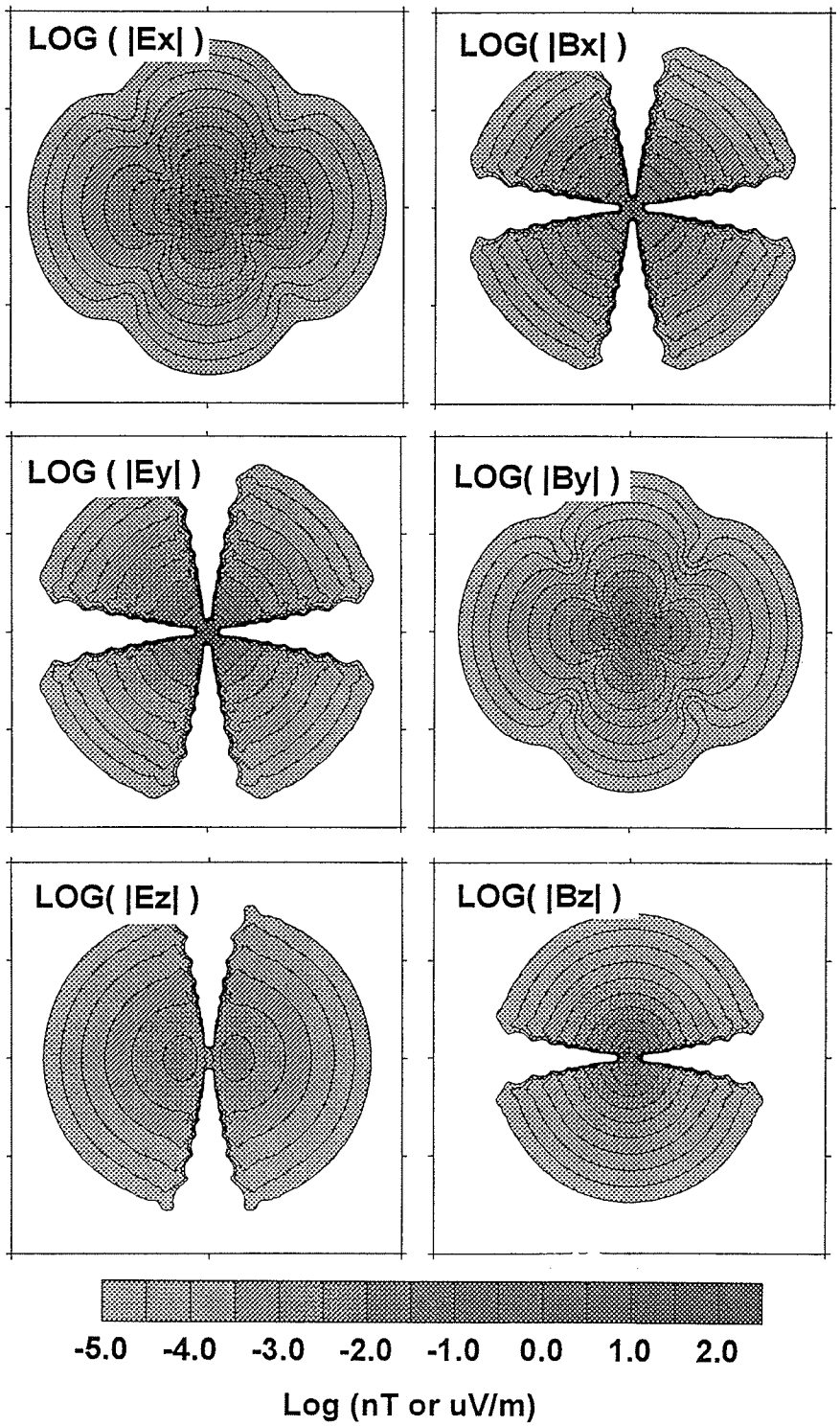

Figure 2.5 Six components of the electromagnetic fields on the interface of a double half-space (plan view of interface). The HED source is located at the centre of each plot and has a dipole moment of 1000 Am. (Ferguson, pers. comm., 1995) The upper and lower half-spaces have conductivities 3.0 and 0.3 Sm^{-1} respectively. Each plot is 12 km $\times$ 12 km .

in length (typically about 500 m). The antenna is coupled with the seafloor by low-noise, silver/silver chloride electrodes (Cox *et al.*, 1986; Webb *et al.*, 1985). The electrodes are the main source of the instrumental noise which is about 10^{-24} $V^2m^{-2}Hz^{-1}$ at frequencies above 1 Hz (Webb *et al.*, 1985). For controlled-source signal data, synchronous stacking techniques may be used to enhance the signal to noise ratio allowing small electric signals to be detected. Webb *et al.* (1985) have measured electric field signals at the seafloor as small as 10^{-12} Vm^{-1} with a signal to noise ratio of 10. A half-hour's stacking allowed the signal to be measured to within 10^{-14} Vm^{-1}. In general, the stacking time will depend on the period of the stacking cycle.

The magnetic field is detected using one of a variety of magnetometer types. Two types that are in general use for seafloor EM surveys are induction coils and SQUID magnetometers (*e.g.* Vozoff, 1991). An induction coil in its simplest form is an insulated, closed loop of wire which produces a voltage proportional to its area multiplied by the time derivative of the magnetic field normal to the area. The signal can be increased by increasing the area of the loop, or by increasing the number of turns of wire on the loop. Typical sensitivities for an induction coil magnetometer are 5×10^{-4} Hz, 10^{-5} Hz and 10^{-4} Hz at frequencies of 0.1 Hz, 10 Hz and 100 Hz respectively (Breiner, 1981). In the laboratory and in theoretical calculations SQUID magnetometers are much more sensitive, with detection levels as low as 10^{-5} nT at all frequencies (Vozoff, 1991). However, in the field, the noise level is about 10 times larger. The operating principles of a SQUID are not as simple as for an induction coil and the reader is referred to Vozoff (1991) for a detailed description.

Figure 2.6 shows the noise levels reported for various magnetometers. At present, induction coils have lower noise levels than SQUIDS above 100 Hz, and it is not yet clear which is superior in the 0.1-10 Hz band (Vozoff, 1991).

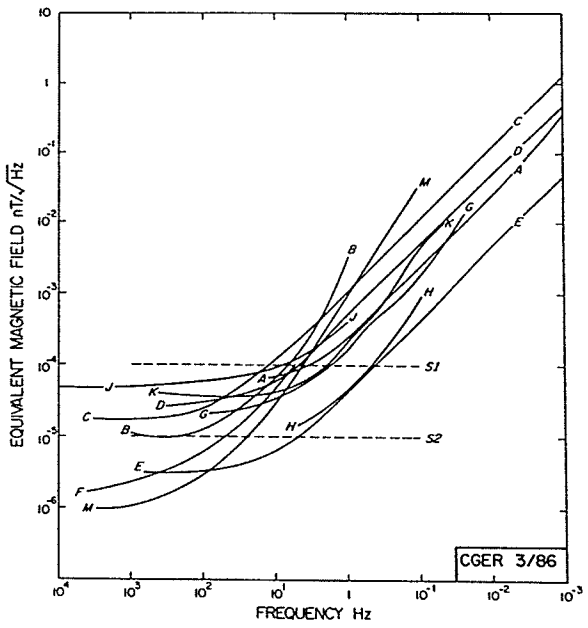

Figure 2.6 Noise figures reported for various magnetometers (Vozoff, 1991). S1 and S2 are, respectively, the typical observed and theoretical figures for SQUIDS.

2.5 Ambient Noise at the Seafloor

Electric fields are induced in the oceans mainly by two physical mechanisms (Filloux, 1974). The first mechanism is that of electromagnetic induction by time-varying source fields which are external to the Earth. The second mechanism is that of ocean water motion in the Earth's steady magnetic field. At frequencies > 1 cph, the first mechanism plays a much larger role than the ocean currents (Bindoff *et al.*, 1986).

In a test of their new seafloor electric field instrument off the west coast of the United States, Webb *et al.* (1985) measured the natural seafloor electric field at two different locations. Curve B in figure 2.7 shows the electric field measured by a 600 m antenna in 3700 m of water. Curve C shows a similar measurment at a second location in 4300 m of water. Curve A shows the instrument noise level measured when the two

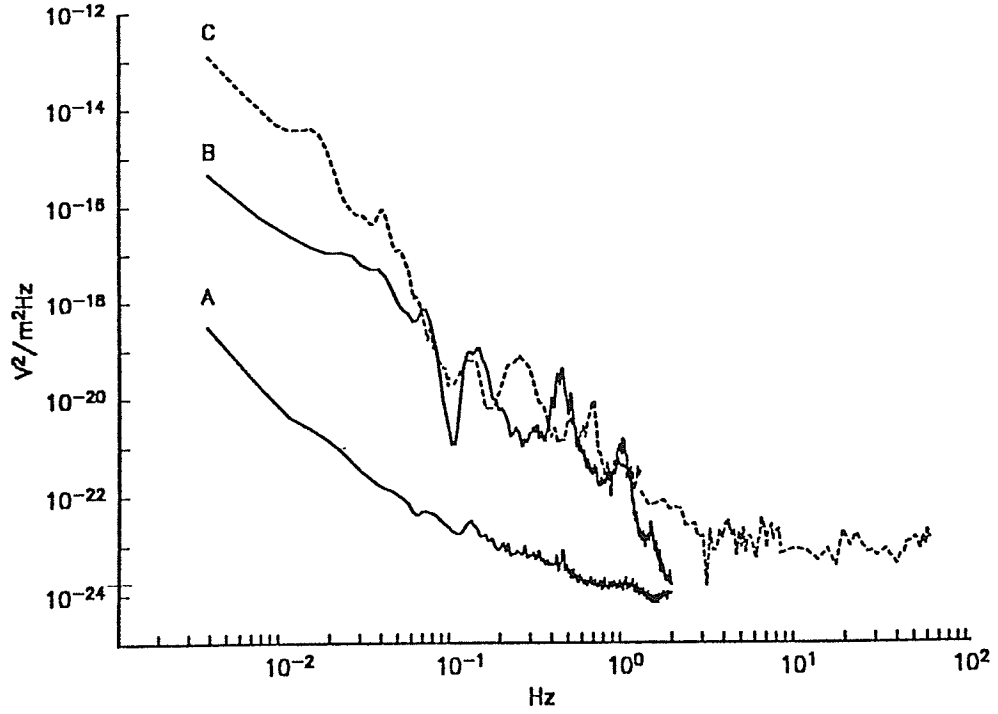

Figure 2.7 Plot of Electric field spectra (Webb *et al.*, 1985). Curve 'A' is an example of electrode noise (where the electrodes were placed close together). Curve 'B' is a spectrum of the seafloor electric field signal over a single 600 m antenna. Curve 'C' is from an experiment where the seafloor electric field signal was measured over a twinned 680 m antenna, allowing a cross-spectrum to be calculated. All curves are normalized to a 1000 m antenna.

electrodes were placed 1 m apart. The leveling off of curve C at 10^{-23} $V^2m^{-2}Hz^{-1}$ is thought by Webb *et al.* to be due to instrument electronics. Thus, above a few Hertz, the ambient electric field probably has a power level of $\leq 10^{-24}$ $V^2m^{-2}Hz^{-1}$ which is comparable to the instrumental noise levels shown in curve A. This indicates that an artificial electric field can be detectable to $\leq 10^{-12}$ Vm^{-1} (Webb *et al.*, 1985).

Assuming a white-noise model at frequencies $< f_{max}$, and the application of an antialiasing filter to remove signal at frequencies $> f_{max}$, the standard deviation of the noise may be shown through Parseval's Theorem to be

$$\sigma = \sqrt{2S_0 f_{\max}} \tag{2.4}$$

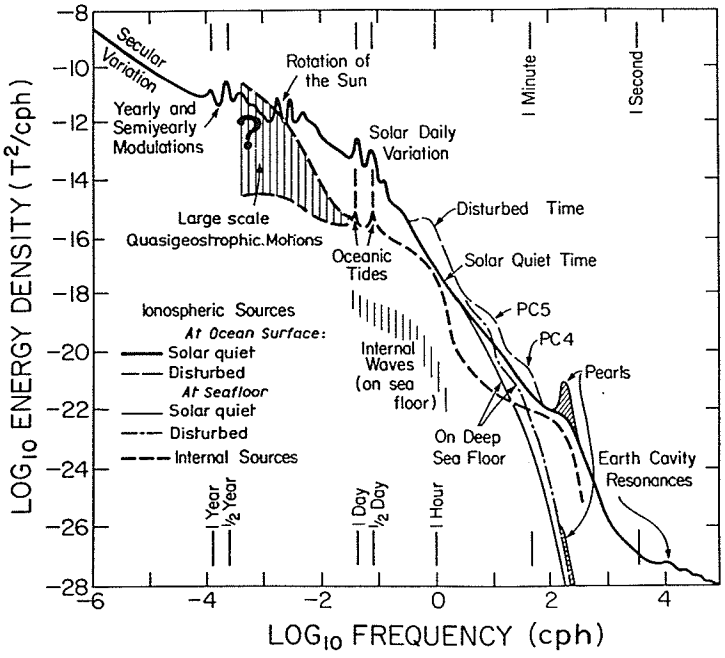

Figure 2.8 Spectra of natural magnetic fluctuations (noise) observable in the oceans (from Filloux, 1987).

for both the electric and magnetic fields. In figure 2.7, the electric field noise power at around 100 Hz is approximately 10^{-23} $V^2m^{-2}Hz^{-1}$. Therefore, assuming a sampling rate of 100 Hz and that all frequencies > 1000 Hz are removed by filtering, the standard deviation for a white electric field noise level is σ_e=0.14 nVm^{-1}. Figure 2.8 illustrates the power level of the natural magnetic field at the seafloor. At 100 Hz (3.6×10^5 cph), the magnetic field noise is $\leq10^{-7}$ nT^2Hz^{-1}. This yeilds a standard deviation for a white magnetic field noise level of σ_m=0.014 nT.

Signal stacking of n waveforms will reduce the noise level by a factor of $n^{-1/2}$. Assuming 1024 cycles are stacked, the standard deviations of the electric and magnetic field noise levels would be about 0.004 nVm^{-1} and 4×10^{-4} nT respectively. The value of σ_e is the same order of magnitude as the instrumental noise found by Webb *et al.* (1985). The value of σ_m is similar to the practical detection limit of SQUID

magnetometers in figure 2.6.

2.6 Petroleum Geology

The occurrence of petroleum (oil and gas) is the result of chemical, physical, and geological factors controlled by origin, migration, and entrapment (North, 1985). It is important to have at least a minimum knowledge of these factors during exploration for undiscovered resources. The purpose of this section is to provide a very brief review of some of the principles of petroleum geology to build a framework for the modelling in later chapters. Chapter 3 builds on the information given here, illustrating how electromagnetic methods may be used in the exploration for petroleum.

Petroleum is a naturally occuring mixture of hydrocarbons and non-hydrocarbons. Carbon and hydrogen are the only elements essential to its composition. Although there are many differences in opinion on the details of petroleum formation, most theories agree on its organic origin (*e.g.* North, 1985; Tissot & Welte, 1978). Petroleum originates in a chemically reducing environment, in organic-rich shales or carbonates (source rocks) that were deposited as muds. However, petroleum is found today in porous, permeable strata (reservoir rocks) that were commonly deposited in well-oxygenated environments such as shorelines. Therefore, the petroleum must have migrated from the point of origin into a porous reservoir rock. Since oil and gas are lighter than water, the migration normally has an upward tendency. When the oil or gas in the reservoir rock reaches a permeability barrier (cap rock), it may accumulate into an economically significant concentration (North, 1985). The end of the migration path is a called a trap.

Hydrocarbon traps may be classified according to the type of structure that produces the cap. Two main groups of traps are obvious; traps formed by structural deformation (structural traps) and traps related to primary features in the sedimentary sequence (strati-

graphic traps). Combination traps contain elements of these two basic trap types. Figure 2.9 shows a few simplified examples of trap types. Structural traps may be the result of rocks being folded into domes or anticlines (a), faulted (b and c), or the result of salt domes rising into a layered sedimentary sequence (d). Stratigraphic traps may be the result of events during the deposition of sediments (e and f), for example channels, beaches or reefs. A change in depositional environment from deep marine to shallow marine and back again (g), or the development of an uncomformity (g) are other examples of stratigraphic traps. Combination traps contain elements of the two basic trap types (h). Changes in the structure or stratigraphy of the subsurface will often mean changes in the electrical conductivity. In such cases, electromagnetic methods may be used as an exploration tool in the search for petroleum.

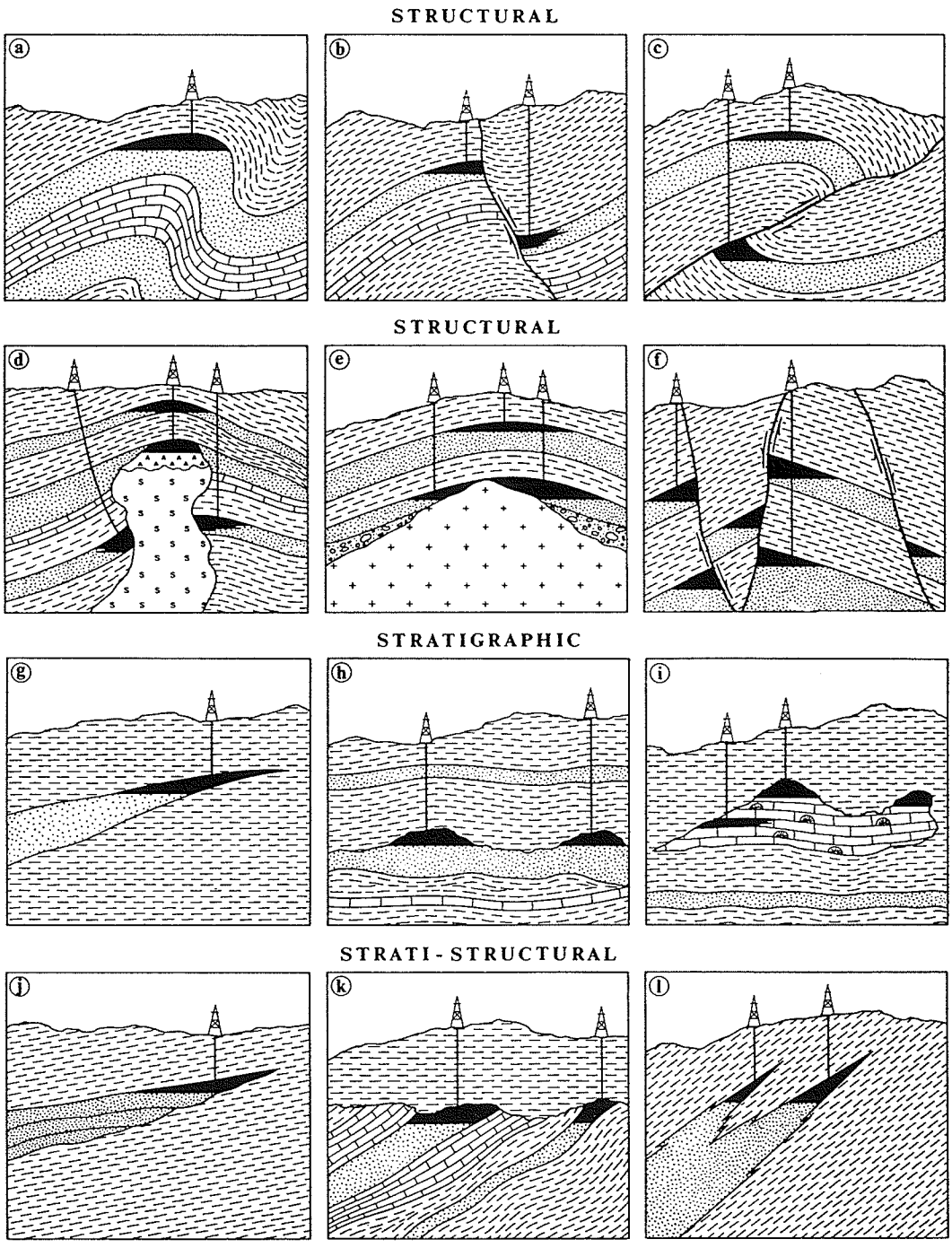

Figure 2.9 Examples of petroleum traps (from LeRoy, 1977). Anticlines (a), faults (b, c), and salt domes (d) are examples of structural traps. Traps due to events during deposition (e, f) or changes in depositional environment (g) are examples of stratigraphic traps. Many traps have some features of both structural and stratigraphic traps (h-l).

Chapter 3

EM Methods in Petroleum Exploration

3.1 Introduction

The importance of EM methods is growing rapidly in the continuing and increasingly more difficult search for hydrocarbon deposits. To date, there has been no application of CSEM techniques to the search for an offshore oil and gas deposit, however, many different land-based EM methods have been used in the last two decades with varying success (*e.g.* Orange, 1989; Nekut & Spies, 1989; Spies, 1983).

Although it is recognized that seismic methods are by far the most widely used geophysical tool for petroleum exploration worldwide, there are several reasons that may make seismic data difficult or impossible to interpret. For example, interpretation of seismic data is difficult in regions dominated by scattering or the high reflectivity that are often associated with carbonate reefs or volcanic cover (Chave *et al.*, 1991). The latter situation is a frustrating problem in exploration, as it is known or suspected in many cases that oil-bearing horizons exist beneath the near-surface volcanics (*e.g.* Orange, 1989; Keller, 1983). In these situations, EM methods are well suited for exploration, as the cover rocks are more resistive than the underlying sedimentary rocks. The EM method has proven to be a useful tool for identifying the existence of the deep sedimentary rocks and for giving an estimate of the thickness of both the sediments and the volcanic cover (Orange, 1989). This chapter presents a summary of the use and applications of some

of the EM methods used in oil and gas exploration worldwide.

Applications of EM methods in petroleum exploration may be divided into four categories: mapping geological structure, mapping stratigraphy, mapping hydrocarbon alteration, and combined analysis with other geophysical methods (Nekut & Spies, 1989). Obviously this categorization is not steadfast as the distinction between structural and stratigraphic elements is not always clear, and most models must contain elements of each.

3.2 Mapping Structure

A typical structural model as used in EM mapping, features zones of variable geometry with the individual zones having constant electrical properties throughout. Examples of structural models were illustrated in figure 2.9. In this section, three examples of the application of EM methods for mapping subsurface structure for petroleum exploration will be shown.

The first case presented involves a range of mountains consisting of volcanic rocks adjacent to a basin of hydrocarbon-bearing sedimentary rocks (Orange, 1989). Figure 3.1a shows the extent of available information before any EM work was conducted. The sedimentary rocks were known to exist west of the volcanic cover from well and outcrop information. East of the volcanics, well information indicated no sediments at depth. It was suspected that the hydrocarbon bearing formation continued beneath the volcanic rocks, however, seismics could only trace the sediments to the edge of the volcanics. To determine whether the sedimentary sequence continued beneath the volcanics, an MT survey over the area was conducted. Figure 3.2a is a sample data set from over the sediments to the west, illustrating the conductive sediments near the surface and the resistive basement at depth. Figure 3.2b, data from a site located over

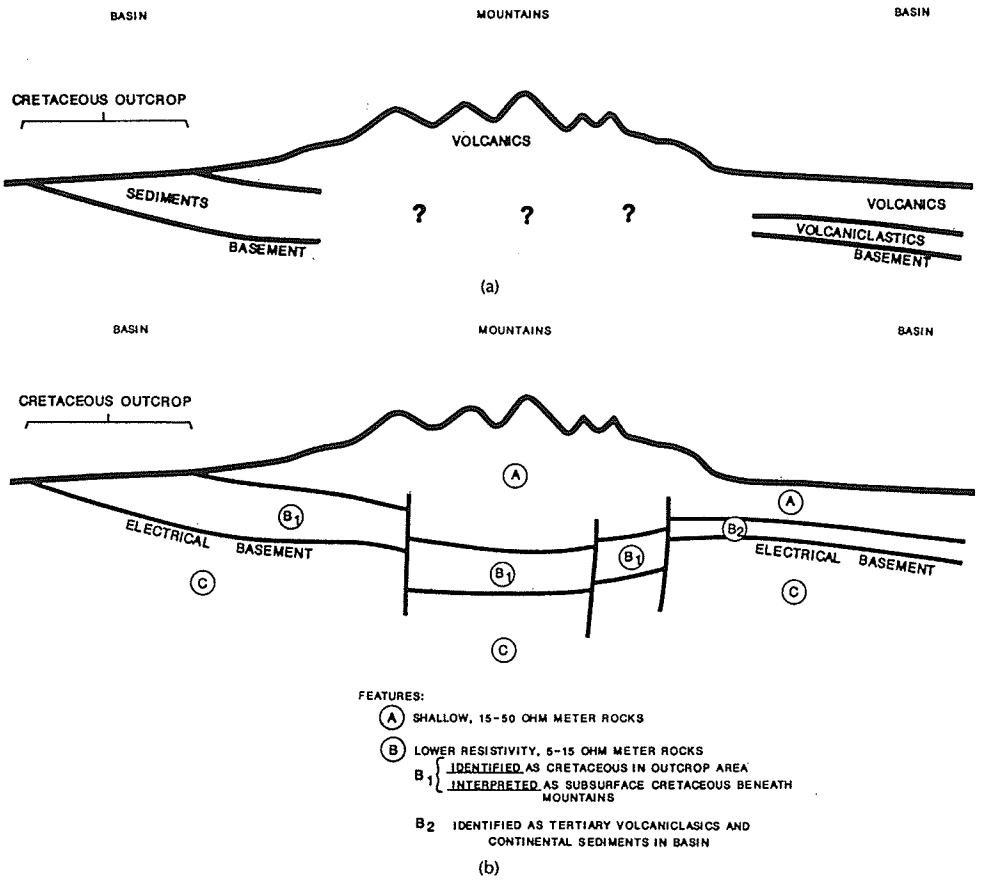

Figure 3.1 Evaluation of a hydrocarbon prospect involving extensive volcanic cover (from Orange, 1989). (a) Presurvey cross section. (b) Cross section after MT survey and interpretation.

the volcanics, shows the high resistivity volcanics near the surface. This figure also shows a layer of low resistivity rock between the surface volcanics and the resistive basement. This indicates that the sediments most likely do exist below the volcanic cover, an interpretation later confirmed by well information. An interpretation of the area after the MT survey is shown in the cross section in figure 3.1b.

The second example of structural mapping employs a central-loop time domain CSEM method for sounding of the Emigrant Trail Thrust fault system in Wyoming (Nekut, 1987). Figure 3.3 is a generalized geological cross-section of the Emigrant Trail Thrust area showing a resistive wedge of Precambrian granite that has been thrust over a

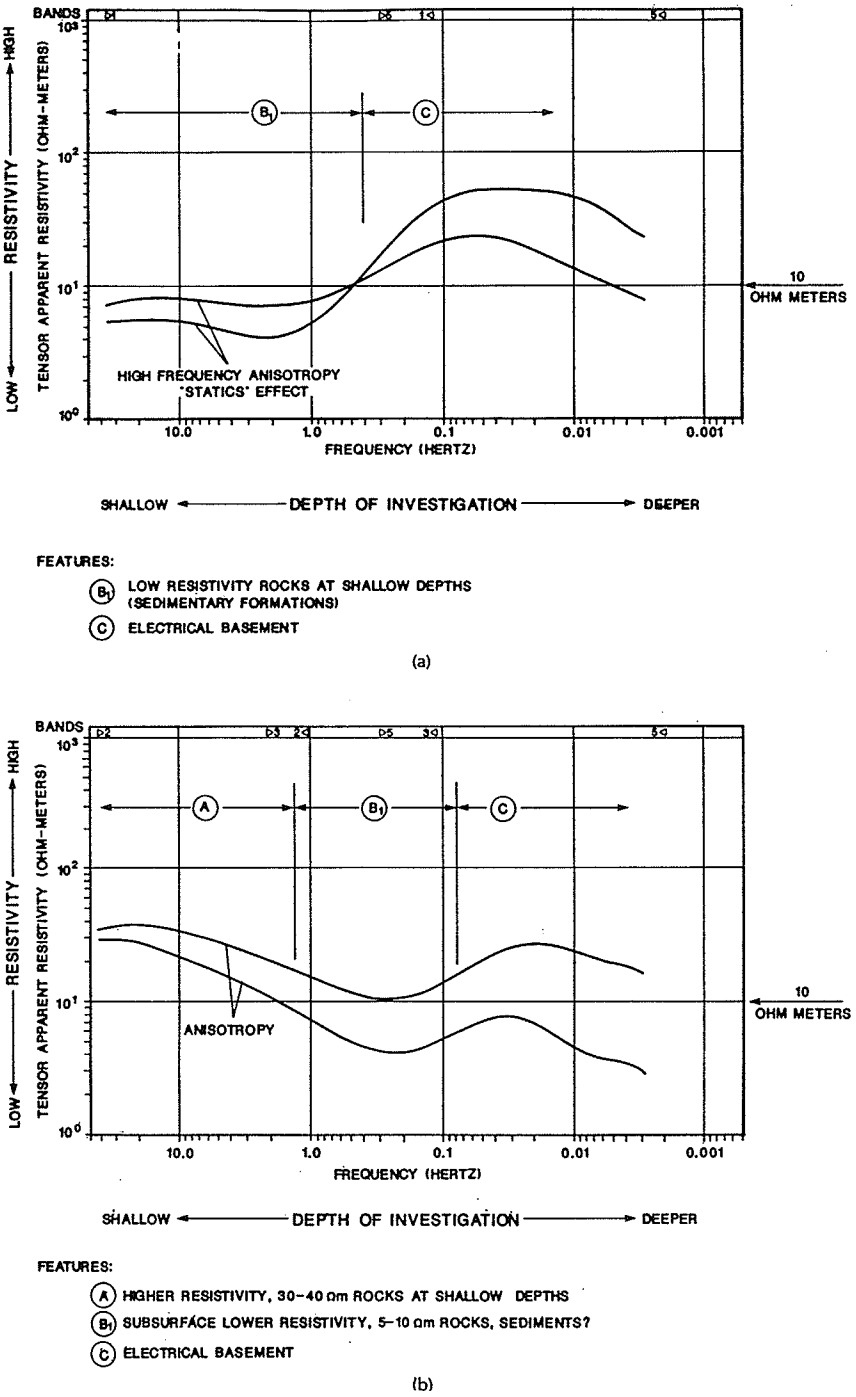

Figure 3.2 Representative MT data from the survey investigating the volcanic-covered area in figure 3.1 (from Orange, 1989). (a) Data from a "calibration" site over the sedimentary rocks. (b) Data over the volcanics showing high resistivity volcanics near the surface and more conductive sediments at depth.

sedimentary basin that contains conductive Mesozoic rocks overlying resistive Palaeozoic rocks. A cover of conductive Tertiary rocks overlays the entire area. The cross-section in figure 3.3 shows the location of the 4 central-loop soundings over the area. The data from these soundings were inverted using layered 1D models and are presented as integrated conductivity as a function of depth with the integrated conductivity of the electric well logs shown for comparison. Figure 3.4a shows a three layer inversion of the data from the two soundings over the sedimentary basin. Figure 3.4b shows a four layer inversion for the two soundings over the thrust site. The inversions of the data from the two different sites distinctly show that a resistive wedge of granite is present at the thrust site and that it thickens downdip.

The third example is structural mapping at the Tomera Ranch Oil Field, Nevada (Ostrander, 1990), using controlled-source audio-frequency magnetotellurics (CSAMT). The CSAMT method is a high-resolution, vertical-sounding resistivity technique that uses an artificial grounded dipole as its signal source. This method has been used extensively in the Basin and Range Province for detailed structural mapping of potential structural oil and gas targets previously defined by reconnaissance gravity surveys (Ostrander, 1990). The primary applications of CSAMT are the mapping of high angle faults in both the mountain ranges and basins, and the delineation of conductive Palaeozoic units at depth. The locations of the CSAMT survey line and two wells (one producing and one dry) are shown in figure 3.5. The data from the Tomera Ranch Oil Field is shown in figures 3.6a (resistivity data) and 3.6b (phase data). A major high angle discontinuity, interpreted as a fault, is well-defined in the data between stations 300E and 500E. This high angle structure is observed in the resistivity data as an abrupt decrease in resistivity in the deeper data (2 Hz and below) to the west. The phase profile graphically displays the base of the conductive valley fill. The positive phase values are indicative of high

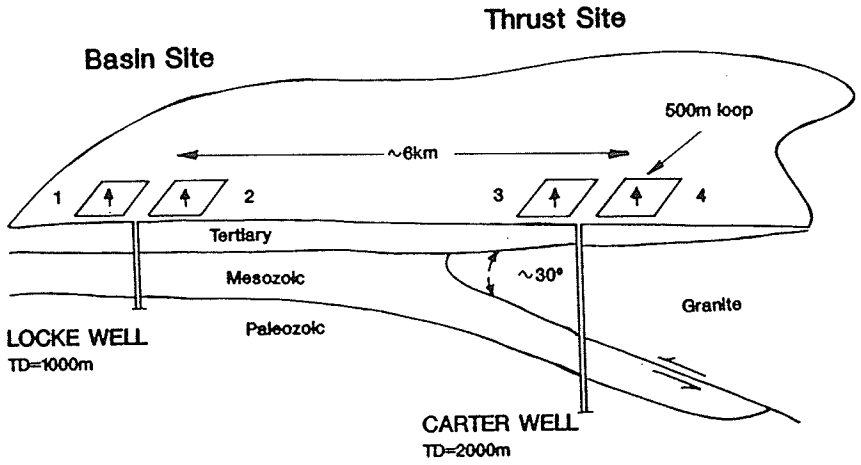

Figure 3.3 Generalized geologic cross section across the Emigrant Trail thrust, Wyoming, showing the loop and well locations (from Nekut, 1987).

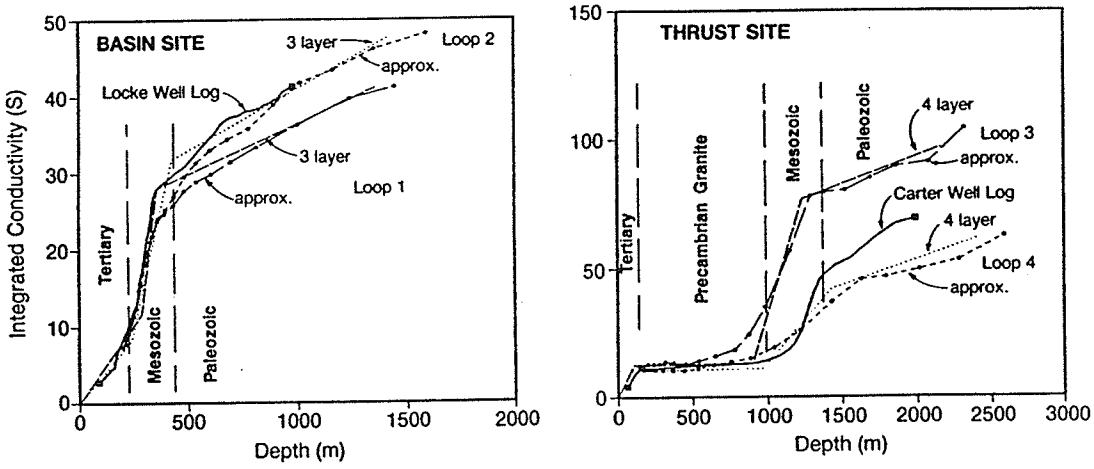

Figure 3.4 Integrated well log and conductance inversions at the basin site (a), and the thrust site (b) (from Nekut, 1987).

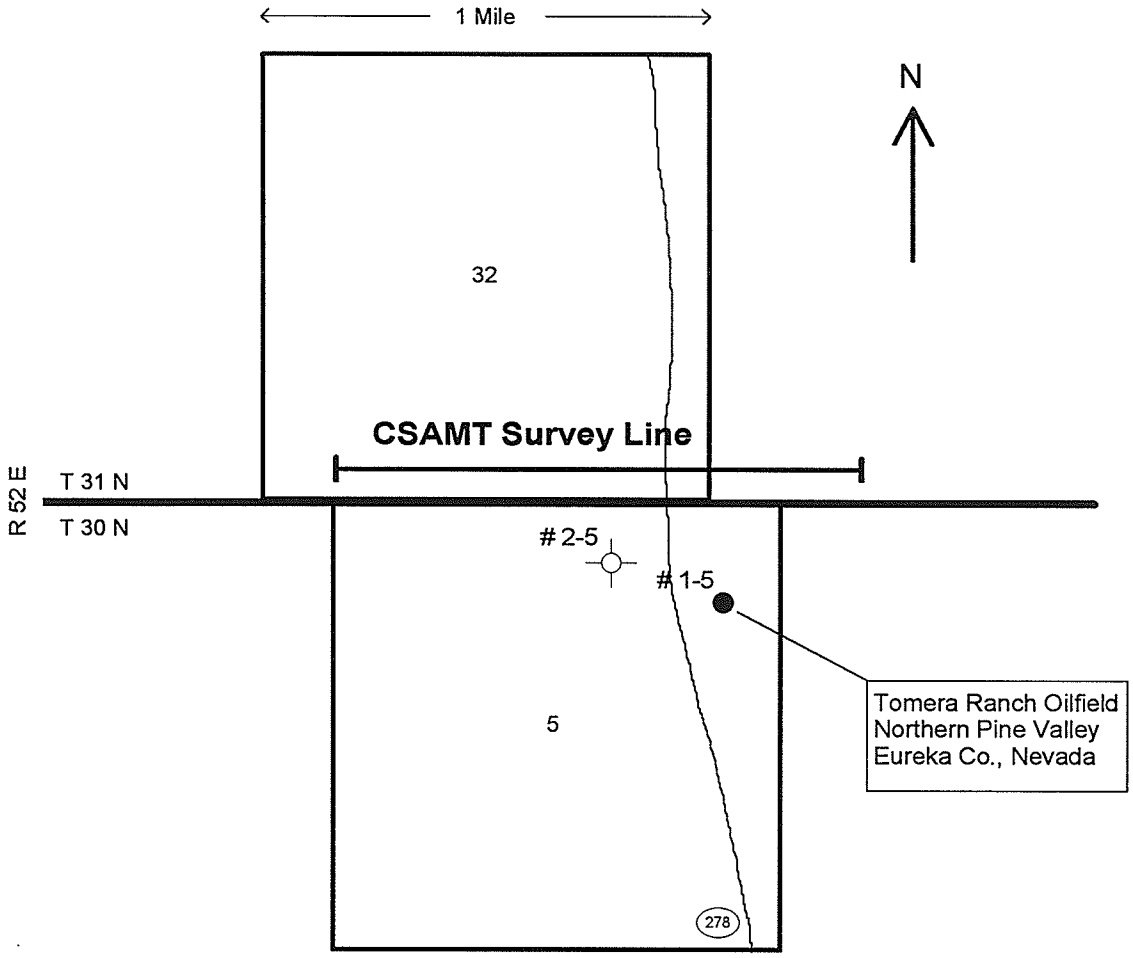

Figure 3.5 Location of the Tomera Ranch Oil Field showing the CSAMT survey line, one producing well and one dry well (from Ostrander, 1990).

conductivity valley fill and the negative values define the high resistivity volcanics or Palaeozoic bedrock beneath the conductive fill (Ostrander, 1990). An interpretation of the data from figure 3.6 is shown in figure 3.7.

3.3 Mapping Stratigraphy

Stratigraphic mapping using EM methods means the determination of horizontal variations in the electrical conductivity of a known or partially known structure (Nekut & Spies, 1989). The stratigraphic mapping example discussed here will involve geological

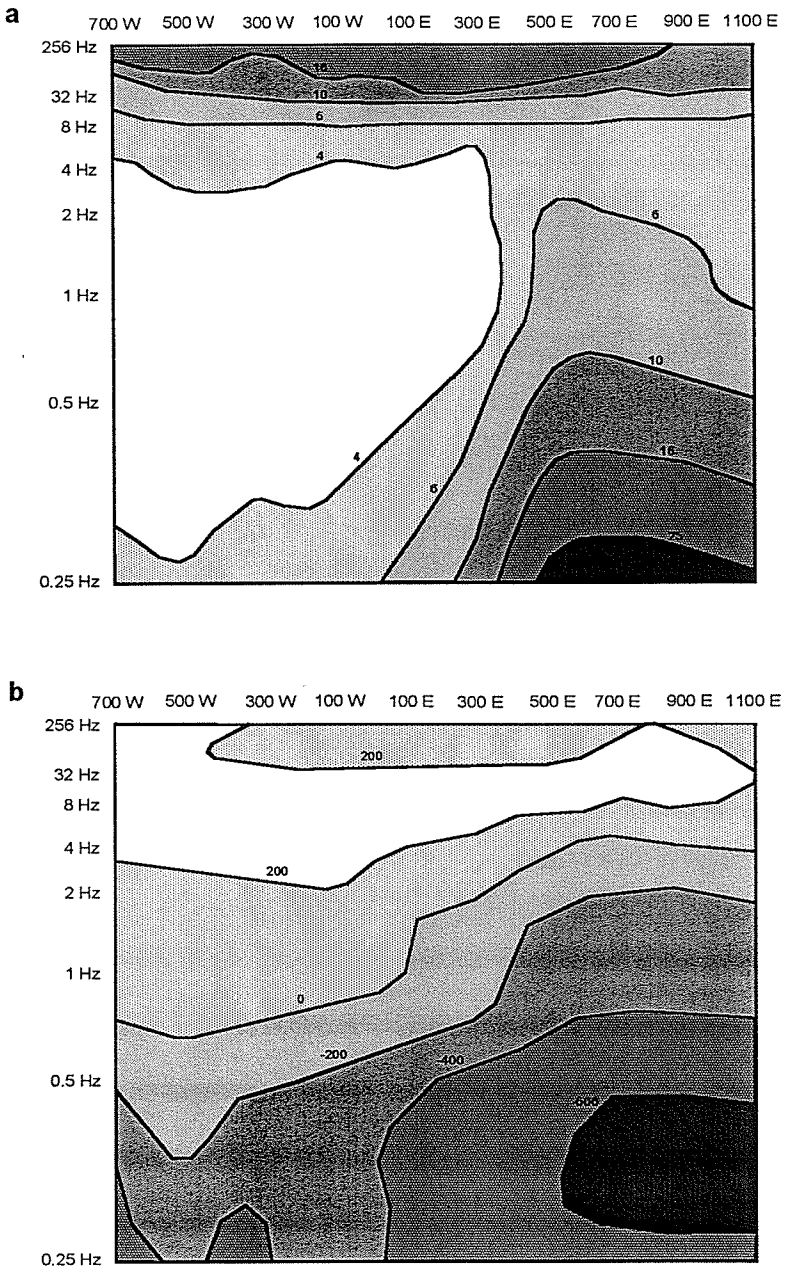

Figure 3.6 Resistivity (a) and phase (b) data from the Tomera Ranch Oil Field (from Ostrander, 1990). The high angle discontinuity between stations 300E and 500E is interpreted to be a fault.

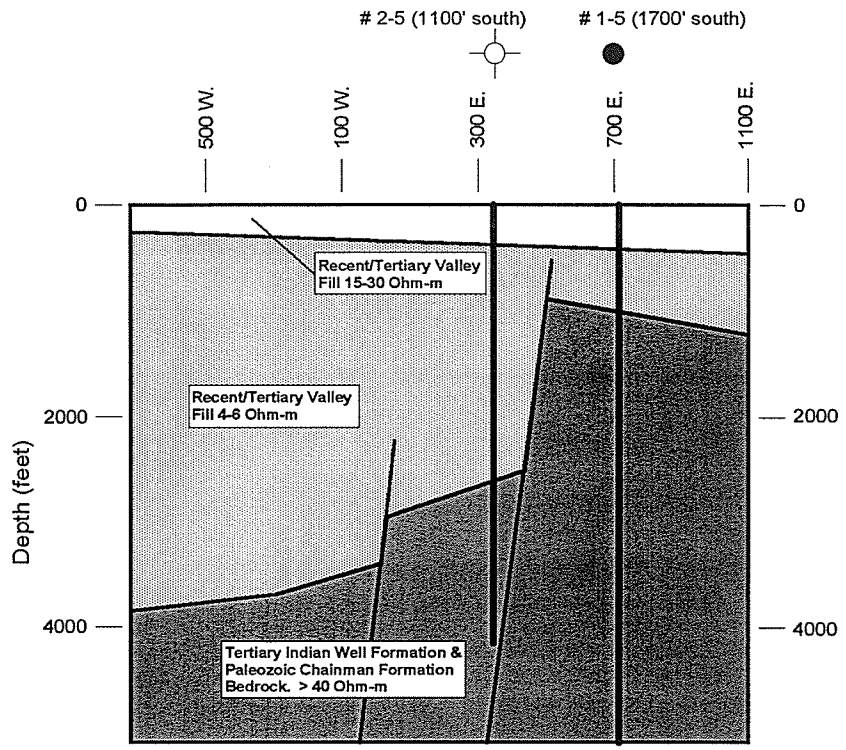

Figure 3.7 Geologic interpretation of geophysical data from Tomera Ranch Oil Field (from Ostrander, 1990).

structures with essentially horizontal layers where the conductivity in each layer varies slowly. Stratigraphic mapping applications of CSEM are usually limited to depths of less than 1000 m and to problems that are difficult or expensive to solve by seismic methods (Nekut & Spies, 1989). Although there are many examples of stratigraphic mapping using EM methods, one example will suffice to illustrate the concept. In the former Soviet Union a method known as ZSBZ (Zondirovanie Stanovleniem polia v Blizhned Zone), or transient sounding in the near zone, is used to map the variations in conductivity of oil-bearing horizons (Spies, 1983). Near-zone sounding means that the transmitter-receiver separation is less than the depth of exploration. This method

has found great success in hydrocarbon exploration in the Siberian platform, the Soviet Union's largest sedimentary basin. ZSBZ is used to determine the longitudinal conductance, S (the conductivity-thickness product), of the productive horizon in a multilayered basin. The productive horizons in the Siberian platform generally contain saline water with resistivities of about 0.1 Ω.m and formation resistivities an order of magnitude larger (Spies, 1983). In the zones that contain hydrocarbons, the highly conductive water is displaced, thus depressing the conductance. Figure 3.8c is a geologic cross-section of a particular oil field examined in the Siberian platform. The productive horizon is a lithologic trap of argillaceous sands 42 m thick with porosity between 7% and 18%. The sounding data over this area are shown in figure 3.8b, and the conductance S in figure 3.8a. There is a marked change in the appearance of the sounding curves from the oil bearing to the water bearing parts of the profile. Note also the dramatic increase in the conductance over the south part of the profile where the oil gives way to water. ZSBZ sounding has been used extensively in Russia as a valuable tool for detection of layers with good reservoir properties (Spies, 1983).

3.4 Hydrocarbon Induced Alteration

Many sedimentary basins are known to have geochemically, geobotanically, and geologically anomalous zones (Nekut & Spies, 1989; Spies, 1983; Sternberg & Oehler, 1990). The cause of the anomalous zones is that some hydrocarbon reservoirs leak and the upward migration of hydrocarbons and hydrogen sulphide from the reservoir produce a chemically reducing environment close to the surface where an otherwise oxidizing environment would be found. The reducing environment results in the leaching of iron and manganese ions to produce a zone of disseminated pyrite mineralization over or around the leaking reservoir (figure 3.9). Pyrite is polarizable and therefore detectable

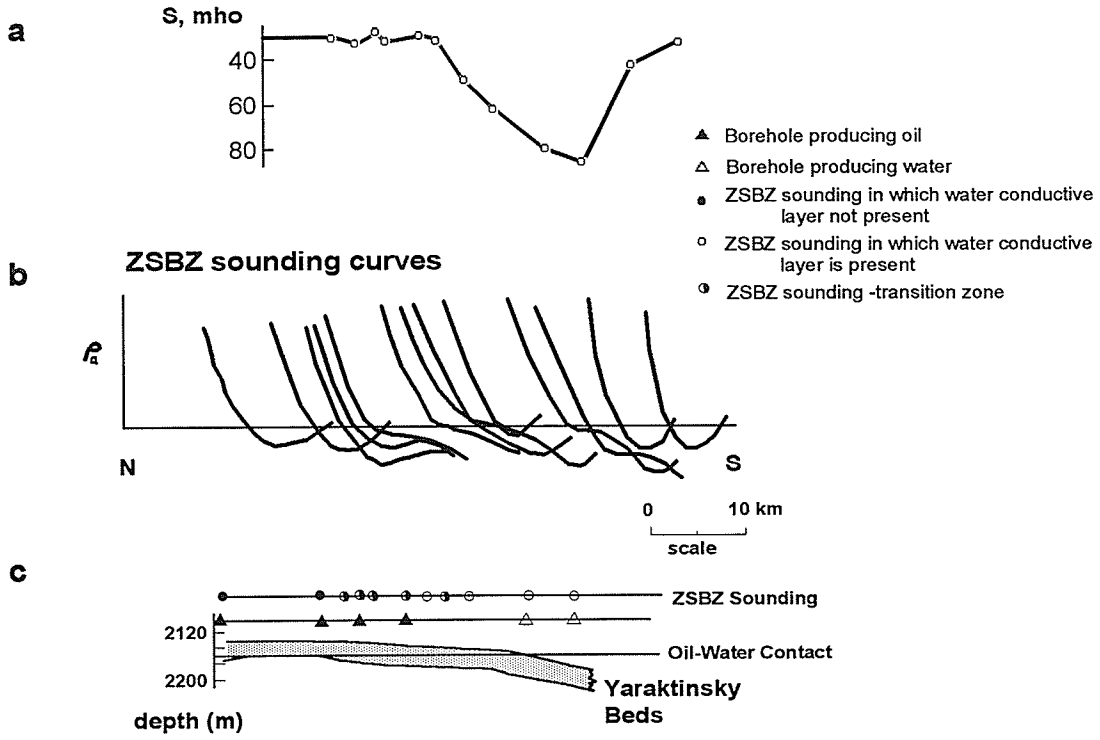

Figure 3.8 ZSBZ sounding curves and drilling results on a profile over the Yaraktinsky Oil Field in the southeastern Siberian platform (from Spies, 1983). (a) Profile of total longitudinal conductance. (b) ZSBZ sounding curves. (c) Geologic cross-secion.

with an induced-polarization (IP) survey (Sternberg & Oehler, 1990). Besides an IP anomaly produced by the formation of a pyrite zone, the hydrocarbons can increase the concentration of bicarbonate ions which react with the calcium to produce a carbonate cement; this reduces the porosity of the rocks over the reservoir. The reduction in porosity decreases the water content of the rocks and therefore causes an increase in the resistivity which may be detected using an EM technique (Nekut & Spies, 1989; Oehler & Sternberg, 1984).

Time domain IP data from a survey in China is shown in figure 3.10. The survey used a Schlumberger array with a separation of 1000 m between the source electrodes (Nekut & Spies, 1989). In this case, there appears to be no resistivity anomaly coincident

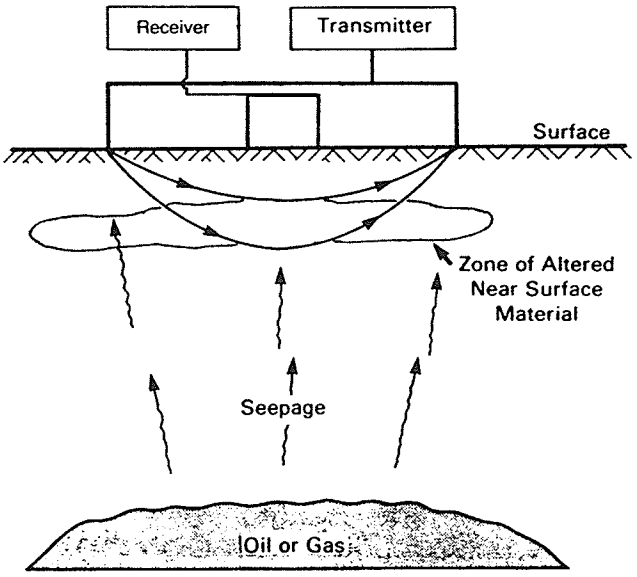

Figure 3.9 Illustration of hydrocarbon seepage and the IP array used to detect zones of altered near-surface material caused by the seepage. (from Sternberg & Oehler, 1990).

with the oil field. However, the IP anomaly is very large over the oil-bearing units and decreases with distance from the area.

Another example is from the Ashland Gas Field in Oklahoma (Sternberg & Oehler, 1990). Figure 3.11 shows the apparent resistivity results for several array lengths. The solid triangles represent high resistivity anomalies directly over the gas field. The anomaly shows up best using an array length of 190 m in this survey.

This method of detection of hydrocarbon alteration shows promise in the oil industry, but it does not always work. The method depends upon the absence of an impermeable seal over the reservoir and the presence of porous, iron-rich, near surface host rocks for the pyrite to form (Nekut & Spies, 1989; Oehler & Sternberg, 1984). It is also important to note that when these conditions exist, the location of the pyrite "plume" will depend on the migration route of the hydrocarbons. The hydrocarbons may leak

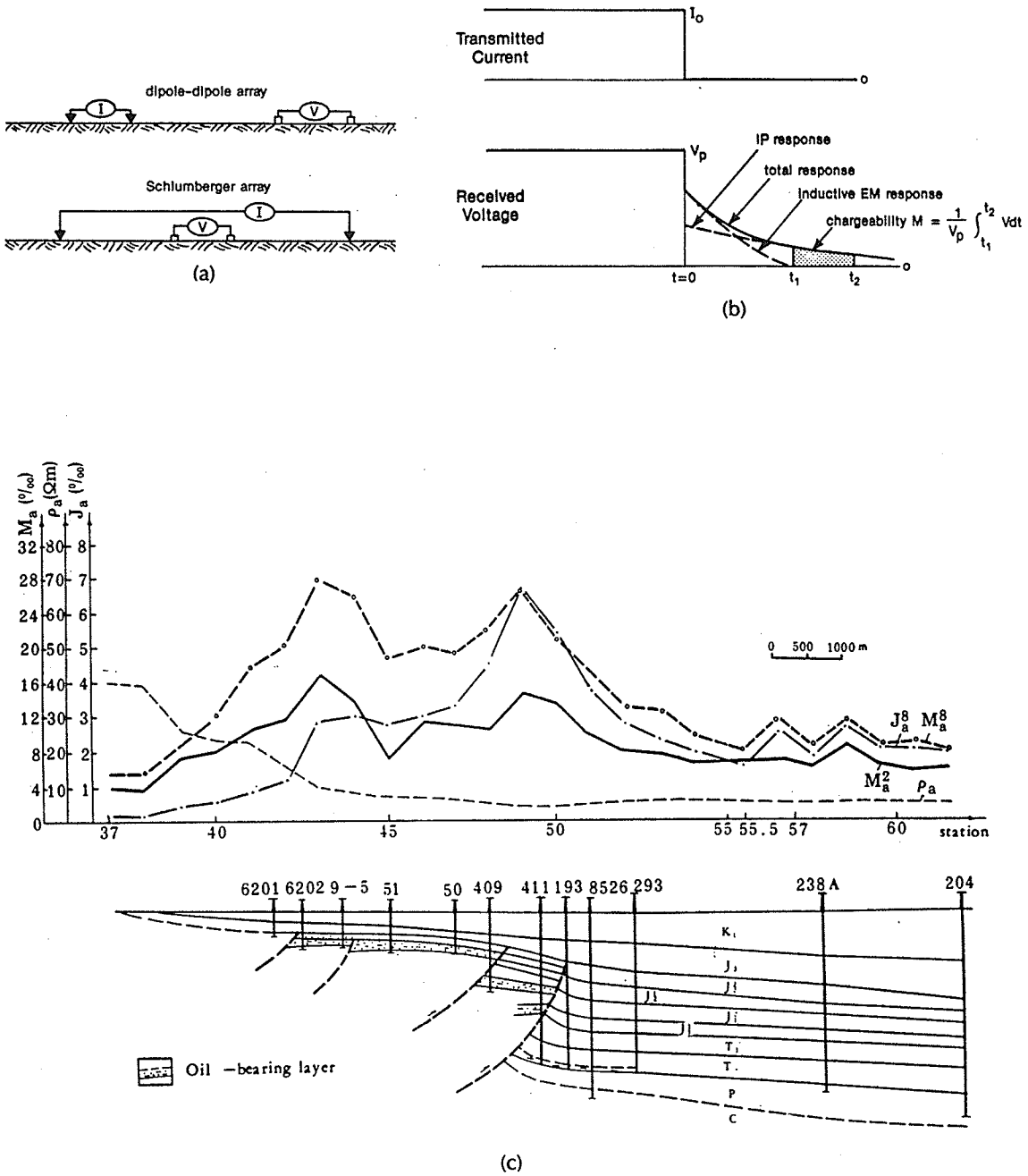

Figure 3.10 IP survey results over an oil field in north-west China (from Nekut & Spies, 1989). There is a strong IP anomaly, but very little apparent resistivity anomaly over this field. ρ_a = apparent resistivity, M_a = apparent chargeability, and J_a = apparent metal factor.

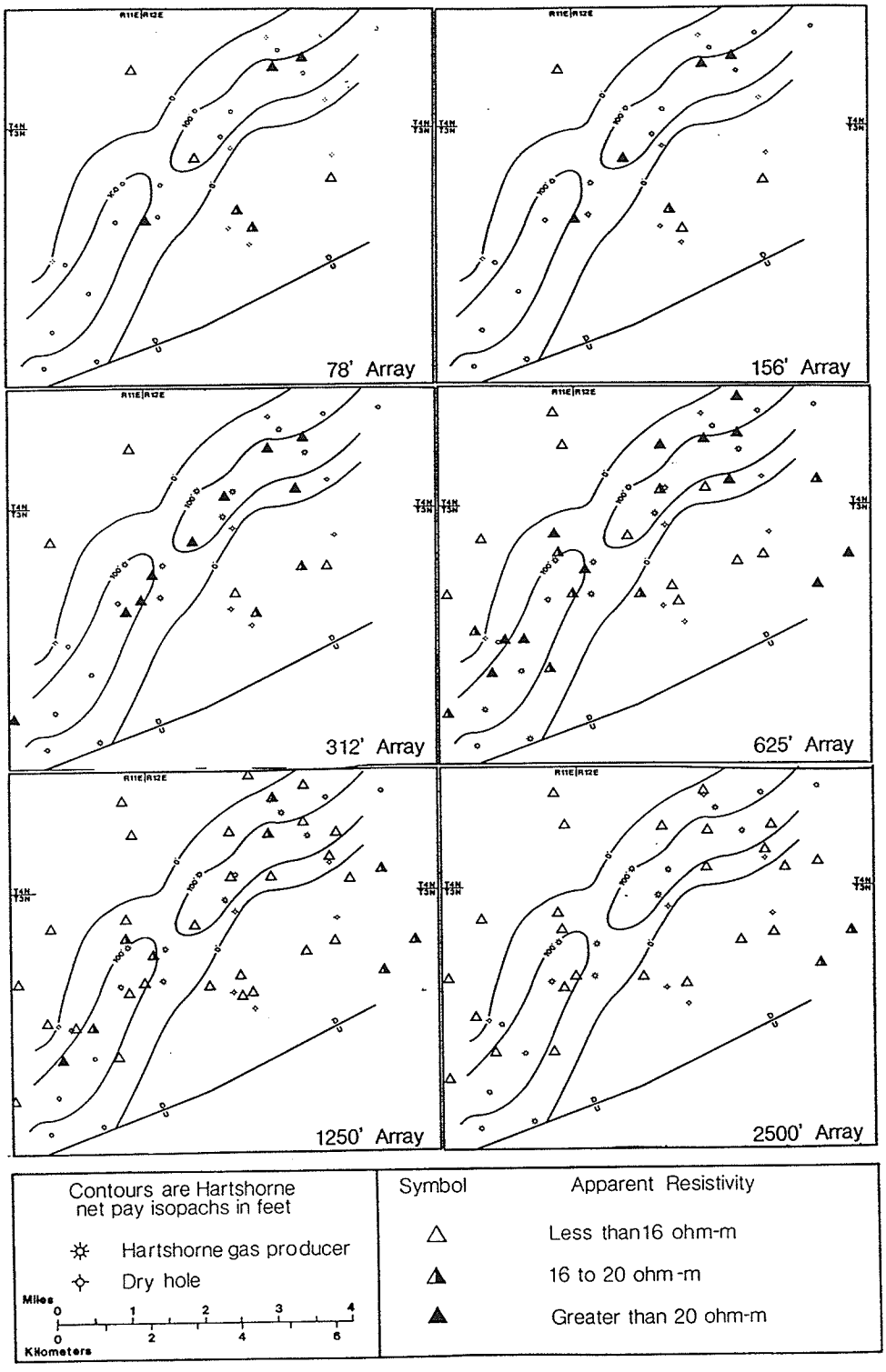

Figure 3.11 Apparent resistivity anomalies at Ashland Gas Field, Oklahoma showing a distinct anomaly over the gas field (from Sternberg & Oehler, 1990).

vertically upwards to form an anomalous zone directly above the reservoir, but the leakage may also take a non-vertical path through jointing, fracturing or faulting of the rocks above. In such a case, the zone of pyrite will be horizontally offset from the reservoir and may be broader or narrower than the reservoir. There have also been surveys that have measured "false" IP anomalies over some areas; these anomalies being unrelated to any hydrocarbon reservoir at depth (Oehler & Sternberg, 1984). Although there is not necessarily a direct correlation between the presence of an IP and/or resistivity anomaly and the production of oil and gas, this method can be an effective method in exploration in some areas, especially when combined with other geophysical methods.

3.5 Combined Geophysical Analysis

The interpretation of subsurface geology almost invariably involves the integration of several types of geophysical data. This is not a different technique from the methods discussed above, but includes the use of EM data to enhance the interpretation of other geophysical data sets such as seismics, gravity and magnetics. The electromagnetic data sets (*e.g.* MT, CSEM, or IP) are usually interpreted within the framework of these other data sets. The final interpretation is then one that best satisfies all the geophysical and geological data.

An example of integrated geophysical interpretation comes from the Eastern Snake River Plain, Idaho (Young & Lucas, 1988). The Eastern Snake River Plain in south-eastern Idaho is covered by volcanics (figure 3.12). Palaeozoic sedimentary rocks of the Western Overthrust Belt appear to plunge under these volcanic rocks. Since some of the sedimentary units contain hydrocarbons, establishing where these rocks exist beneath the volcanics is of interest in oil exploration. The results provided by earlier surveys employing only one geophysical method were inconclusive (Young & Lucas, 1988), suggesting

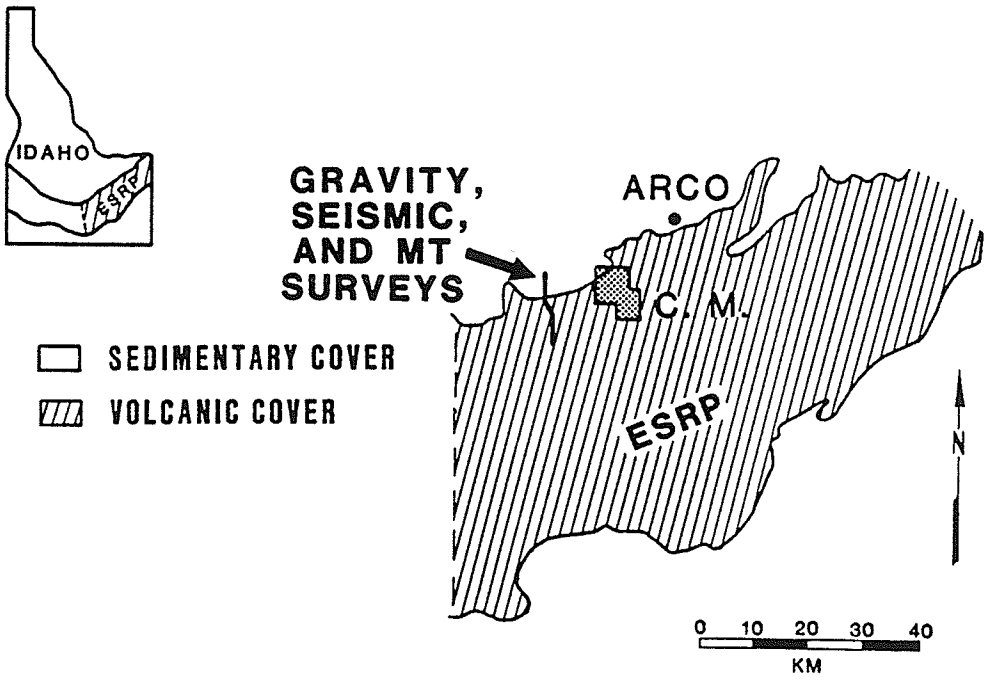

Figure 3.12 Location of the gravity, MT, and seismic surveys across the geologic boundary between the volcanic-cover and sediment-cover in the Eastern Snake River plain (from Young & Lucas, 1988). The town of Arco and Craters of the Moon National Monument lie to the northeast.

that several methods run together along the same line might be needed. Therefore, co-incident gravity, MT and seismic reflection-refraction surveys were conducted along a line traversing the boundary between the volcanic-covered Eastern Snake River Plain, Idaho, and the sediment-covered Western Overthrust Belt (figure 3.12). By integrated geophysical interpretation, a generalized geologic model for the Eastern Snake River Plain boundary is inferred (figure 3.13). This model shows that metasediments extend laterally at least 16 km beneath the volcanic cover. The volcanic-covered and sediment-covered terrains are linked by a major normal fault. Thus, integrated analysis using simple modelling and inversion methods can answer fundamental exploration questions where seismic reflection profiling alone is insufficient.

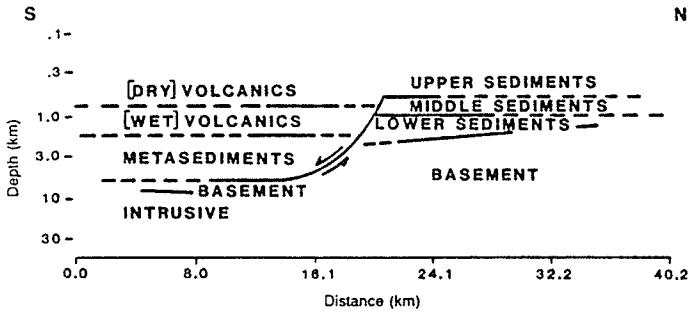

Figure 3.13 A generalized geologic model for the Eastern Snake River plain boundary showing layered models away from the boundary zone and indicating the sense of dip along the boundary zone fault (from Young & Lucas, 1988). The interfaces are solid where controlled by seismic first arrivals.

Chapter 4

EM Theory and Problem Formulation

4.1 Introduction

Most discussions of electromagnetic fields begin with Maxwell's equations which are based on the experimental evidence of researchers such as Faraday and Ampere. Notwithstanding the fact that these equations are empirical (Ward & Hohmann, 1987; Wangsness, 1986), they do describe most macroscopic electromagnetic phenomena. Maxwell's equations may be written in terms of the electric and magnetic field vectors, $\mathbf{E}$ and $\mathbf{B}$, as:

$$\nabla \cdot [\epsilon(r)\mathbf{E}] = \rho_{ch} \tag{4.1}$$

$$\nabla \cdot \mathbf{B} = 0 \tag{4.2}$$

$$\nabla \times \mathbf{E} = -\frac{\partial \mathbf{B}}{\partial t} \tag{4.3}$$

$$\nabla \times \mathbf{B} = \mu\sigma(r)\mathbf{E} + \mu\mathbf{J}_s + \mu\epsilon(r)\frac{\partial \mathbf{E}}{\partial t} \tag{4.4}$$

where $\mathbf{E}$ [Vm^{-2}] is the electric field intensity, $\mathbf{B}$ [T] is the magnetic induction, ρ_{ch} [Cm^{-3}] is the volume electric charge density and $\mathbf{J}_S$ [Am^{-2}] is the current density applied at the source. In a controlled-source experiment, $\mathbf{J}_S$ is controlled by the experimenter. Maxwell's equations in this form are only valid in media which are linear, isotropic, and homogeneous (l.i.h.) with respect to the electric permittivity ϵ and magnetic permeability μ, and linear and isotropic with respect to the electric conductivity σ. This means that ϵ and μ are scalar constants, and may vary with position only. Since this thesis is

concerned with electromagnetic modelling at the seafloor, the media considered will also have non-zero conductivity ($\sigma \neq 0$) everywhere. This restriction will be discussed further in §4.2. The electromagnetic fields must also satisfy certain conditions applied at boundaries between homogeneous regions, for example, the seawater-seafloor interface (Ward & Hohmann, 1987). These boundary conditions can be obtained from Maxwell's equations (Wangsness, 1986) and are given below.

$\mathbf{B}_{n1} = \mathbf{B}_{n2}$	Normal component of $\mathbf{B}$ is continuous
$\mathbf{E}_{n2} - \mathbf{E}_{n1} = \frac{\sigma_{ch}}{\epsilon}$	Normal component of $\mathbf{E}$ is *dis*continuous
$\mathbf{E}_{t1} = \mathbf{E}_{t2}$	Tangential component of $\mathbf{E}$ is continuous
$\mu\mathbf{B}_{t1} = \mu\mathbf{B}_{t2}$	Tangential component of $\mathbf{B}$ is continuous
$\mathbf{J}_{n1} = \mathbf{J}_{n2}$	Normal component of $\mathbf{J}$ is continuous

where σ_{ch} [C.m^{-2}] is the surface charge density.

4.2 Electromagnetic Diffusion

In order to simplify the analysis of Maxwell's equations, several assumptions can be made in the case of most earth problems. The electric permittivity and magnetic permeability are assumed to be constant and equal to their free-space values:

$$\epsilon = \epsilon_0 = 8.85 \times 10^{-12}\text{Fm}^{-1}$$

$$\mu = \mu_0 = 4\pi \times 10^{-7}\text{Hm}^{-1}$$

As mentioned in §4.1, the conductivity is assumed to be non-zero everywhere because we are working in a marine environment. Therefore, we can neglect the fields propogating through air. This assumption allows the quasi-static approximation to be used. That is,

$$\sigma\mathbf{E} \gg \epsilon_0 \frac{\partial \mathbf{E}}{\partial t} \tag{4.5}$$

Equation (4.5) indicates that the electric field inside a conductor varies very slowly

with time. The term on the right side of equation (4.5) is often called the displacement current density, $\mathbf{J}_D$. The quasi-static approximation is made by setting $\mathbf{J}_D$ to zero (West & McNae, 1991).

When the above assumptions are applied, Maxwell's equations become

$$\nabla \cdot \mathbf{E} = \frac{\rho_{ch}}{\epsilon_0} \tag{4.6}$$

$$\nabla \cdot \mathbf{B} = 0 \tag{4.7}$$

$$\nabla \times \mathbf{E} = -\frac{\partial \mathbf{B}}{\partial t} \tag{4.8}$$

$$\nabla \times \mathbf{B} = \mu_0 \sigma(r)\mathbf{E} + \mu_0 \mathbf{J}_s \tag{4.9}$$

Equations (4.6) to (4.9) imply that the sources of the electric field $\mathbf{E}$ are the volume charge density and the time variations in the magnetic induction $\mathbf{B}$. Likewise, the sources of the induction $\mathbf{B}$ are the applied currents and the conduction currents which are dependant on $\mathbf{E}$. Since the sources of one field depend on the value or the time variation of the other field, equations (4.8) and (4.9) are coupled and therefore must be solved simultaneously. Taking the curl of equation 4.8 and eliminating $\mathbf{B}$ gives the vector diffusion equation

$$\nabla^2 \mathbf{E} - \mu_0 \sigma \frac{\partial \mathbf{E}}{\partial t} = -\mu_0 \frac{\partial \mathbf{J}_s}{\partial t} \tag{4.10}$$

while taking the curl of equation (4.9) and eliminating $\mathbf{E}$ gives a second diffusion equation

$$\nabla \times \frac{1}{\sigma} \nabla \times \mathbf{B} + \mu_0 \frac{\partial \mathbf{B}}{\partial t} = \mu_0 \nabla \times \left(\frac{1}{\sigma} \mathbf{J}_s(t) \right) \tag{4.11}$$

Equations (4.10) and (4.11) are only valid in conductors and must obey the general boundary conditions set out in §4.1. The solution of these vector diffusion equations is used to describe the response of the conducting earth to controlled-source excitation.

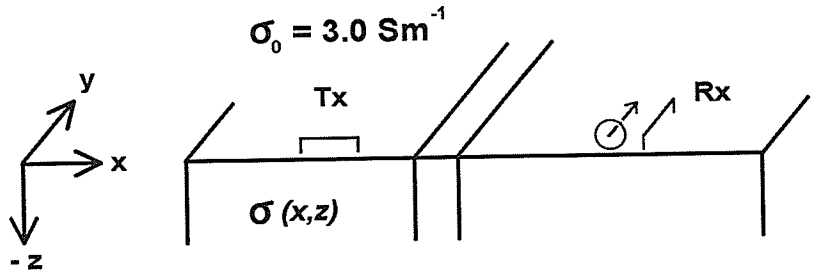

Figure 4.1 Two dimensional Earth excited by a 3D electromagnetic source (Tx). The receivers (Rx) and coordinate system are also shown. The conductivity of the seawater and seafloor are σ_0 and $\sigma(x, z)$ respectively.

4.3 2.5D Problem

The 2.5D problem involves transient electromagnetic excitation of a 2D Earth by a finite (3D) source. In this section of the thesis, I provide a summary of the 2.5D problem formulation described by Everett (1990). The 3D source used in this thesis is a horizontal electric dipole (HED) and is described in §2.4. Analytical solutions for this source on a double half-space are provided in §4.4. The 2D model considered is shown in figure 4.1. A Cartesian coordinate system is employed with z vertically upwards and the conductivity invariant in the y-direction; the source is an x-directed HED. The plane z=0 divides the upper homogeneous region $z \geq 0$ representing the sea water from a lower half-space $z \leq 0$ of variable conductivity $\sigma(x, z)$ representing the inhomogeneous Earth.

Everett (1990) approaches the 2.5D problem using a method similar to that of Stoyer & Greenfield (1976), in which the EM fields are obtained in the y-wavenumber

(q) domain, where y is the along-strike direction. The fields are then transformed back to the space domain by sine and cosine transforms. Solving for the fields in the q-domain reduces the problem of solving the 3D fields for a finite source to a series of 2D problems. Formulation of the problem in the q-domain also avoids many of the numerical problems involved in solving the EM diffusion equations such as generating a 3D FE mesh with tetrahedral elements. However, this method is only possible with a 2D earth conductivity $\sigma(x,z)$. In addition to working in the spatial wavenumber domain, Everett (1990) computes the fields in the Laplace frequency (s) domain. The advantage of working in the Laplace domain rather than directly in the time-domain is apparent when the fields $\mathbf{B}_y(t)$ and $\mathbf{E}_y(t)$ are desired at only one or more specific times: the former method avoids the potential waste of computer resources in time-stepping the fields from t=0s. The fields computed in the s-domain are then transformed back to the time-domain via an inverse Laplace transform. An arbitrary function of time $\mathrm{F}(t)$ may be transformed to the Laplace s-domain or back to the time-domain via the Laplace transform pair

$$\mathrm{F}(r,s) \equiv \int_0^\infty \exp(-st)\mathrm{F}(r,t)dt \tag{4.12}$$

$$\mathrm{F}(r,t) \equiv \frac{1}{2\pi i}\int_{\gamma-i\infty}^{\gamma+i\infty} \exp(st)\mathrm{F}(r,s)dt \tag{4.13}$$

In the Laplace domain, Faraday's Law (4.8) and Ampere's Law (4.9) become

$$\nabla \times \mathbf{E}(r,s) = -s\mathbf{B}(r,s) \tag{4.14}$$

$$\nabla \times \mathbf{B}(r,s) = \mu_0\sigma(r)\mathbf{E}(r,s) + \mu_0\mathbf{J}_s(r,s) \tag{4.15}$$

These equations are used to derive the governing vector diffusion equations. This pair of vector equations may be rewritten as a 3×3 system of partial differential equations (PDEs) where the independent variables are the components of $\mathbf{E}$ and $\mathbf{B}$.

To reduce the problem from 3D to 2.5D, equations (4.14) and (4.15) must be transformed to the q-domain using cosine and sine transforms. In the q-wavenumber domain, the operator $\nabla = (\partial x, \partial y, \partial z)$ becomes $\nabla_q = (\partial x, -iq, \partial z)$. This reduces the PDE system to a 2×2 matrix equation, with the independent variables becoming the along-strike components of the magnetic field $\bar{b}_y(q,s)$ and electric field $i\bar{e}_y(q,s)$ (Everett & Edwards, 1992). The fields $\bar{b}_y(q,s)$ and $i\bar{e}_y(q,s)$ are simply the cosine and sine transformed values of $\mathbf{B}(y,s)$ and $\mathbf{E}(y,s)$ respectively. To formulate the 2.5D problem numerically, the source term $\mathbf{J}_S$ is set to zero and represented instead by a series of boundary conditions on a small enclosing volume around the source. This is done because the field components $\bar{b}_y$ and $i\bar{e}_y$ contain a singularity at the location of the source which must be avoided in a numerical solution.

The along-strike component of Ampere's Law (without the source term) is given by

$$\mu_0 \sigma \bar{e}_y = \left(\frac{\partial \bar{b}_x}{\partial z} - \frac{\partial \bar{b}_z}{\partial x} \right) \tag{4.16}$$

and the x and z components of Faraday's Law may be written as

$$\left(s + \frac{q^2}{\mu_0 \sigma} \right) \bar{b}_x = \frac{iq}{\mu_0 \sigma} \frac{\partial \bar{b}_y}{\partial x} + \frac{\partial \bar{e}_y}{\partial z} \tag{4.17}$$

$$\left(s + \frac{q^2}{\mu_0 \sigma} \right) \bar{b}_z = \frac{iq}{\mu_0 \sigma} \frac{\partial \bar{b}_y}{\partial z} - \frac{\partial \bar{e}_y}{\partial x} \tag{4.18}$$

A single equation in $\bar{b}_y$ and $\bar{e}_y$ is attained by the elimination of $\bar{b}_x$ and $\bar{b}_z$ from (4.16) to (4.18):

$$\frac{\partial}{\partial x} \left(\frac{\sigma}{u^2} \frac{\partial \bar{e}_y}{\partial x} \right) + \frac{\partial}{\partial z} \left(\frac{\sigma}{u^2} \frac{\partial \bar{e}_y}{\partial z} \right) - \sigma \bar{e}_y - \frac{iq}{\mu_0} \frac{\partial}{\partial x} \left(\frac{1}{u^2} \frac{\partial \bar{b}_y}{\partial z} \right) + \frac{iq}{\mu_0} \frac{\partial}{\partial z} \left(\frac{1}{u^2} \frac{\partial \bar{b}_y}{\partial x} \right) = 0 \tag{4.19}$$

where $u = \sqrt{q^2 + \mu_0 \sigma s}$. Similarily, a second equation in $\bar{b}_y$ and $\bar{e}_y$ can be attained by taking the along-stike component of Faraday's Law,

$$s\bar{b}_y = \left(\frac{\partial \bar{e}_z}{\partial x} - \frac{\partial \bar{e}_x}{\partial z} \right) \tag{4.20}$$

and the x and z components of Ampere's Law,

$$\left(\frac{q^2}{s}+\mu_0\sigma\right)\bar{e}_x = \frac{iq}{s}\frac{\partial \bar{e}_y}{\partial z}+\frac{\partial \bar{b}_y}{\partial x} \tag{4.21}$$

$$\left(\frac{q^2}{s}+\mu_0\sigma\right)\bar{e}_z = \frac{iq}{s}\frac{\partial \bar{e}_y}{\partial x}-\frac{\partial \bar{b}_y}{\partial z} \tag{4.22}$$

and eliminating $\bar{e}_x$ and $\bar{e}_z$ to get

$$\frac{\partial}{\partial x}\left(\frac{s}{u^2}\frac{\partial \bar{b}_y}{\partial x}\right)+\frac{\partial}{\partial z}\left(\frac{s}{u^2}\frac{\partial \bar{b}_y}{\partial z}\right)-s\bar{b}_y+iq\frac{\partial}{\partial x}\left(\frac{1}{u^2}\frac{\partial \bar{e}_y}{\partial z}\right)-iq\frac{\partial}{\partial z}\left(\frac{1}{u^2}\frac{\partial \bar{e}_y}{\partial x}\right)=0 \tag{4.23}$$

Equations (4.19) and (4.23) may be written in matrix form as

$$\begin{pmatrix} \partial x\left(\frac{s}{u^2}\partial x\right)+\partial z(\frac{s}{u^2}\partial z)-s & q\partial x(\frac{1}{u^2}\partial z)-q\partial z(\frac{1}{u^2}\partial x) \\ q\partial x\left(\frac{1}{u^2}\partial z\right)-q\partial z\left(\frac{1}{u^2}\partial x\right) & \partial x\left(\frac{\mu_0\sigma}{u^2}\partial x\right)+\partial z\left(\frac{\mu_0\sigma}{u^2}\partial z\right)-\mu_0\sigma \end{pmatrix}\begin{pmatrix} \bar{b}_y \\ i\bar{e}_y \end{pmatrix}=0 \tag{4.24}$$

where the 2×2 partial differential operator matrix is both real and symmetric (Everett, 1990). The fact that the two off-diagonal terms are not zero indicates that the two PDEs are coupled. (Note that for $q=0$, coupling of the equations dissappears. *i.e.* the off-axis terms in equation (4.24) become zero. This situation corresponds to the simpler solution for a 2D source).

4.4 Semi-Analytical solutions for Double Half-Space

Since the field components $\bar{b}_y$ and $\bar{e}_y$ contain a singularity at the point of applied current, the boundary value problem described above must be altered in order to deal with the solution numerically. As will be described in more detail in §5.2, a small "box" is cut out of the solution domain, Ω, around the source. The field components $\bar{b}_y$ and $\bar{e}_y$ on the boundary of this cut out portion of Ω are then matched exactly to the semi-analytic solution for the source over a double half-space (DHS).

The semi-analytic equations for $\bar{b}_y$ and $\bar{e}_y$, given below, were derived by Everett (1990) for a DHS model with σ_0 and σ_1 representing the conductivities of the upper and

lower half-space respectively. For a detailed derivation, the reader is referred to Everett (1990).

Since the conductivity is invariant in the y-direction, the EM fields themselves vary smoothly in this direction. Therefore, the fields can be simplified by Fourier transforming them in this direction. Thus the solutions for a grounded electric dipole with dipole moment $\mathbf{P}$ located at the origin on the sea-seafloor interface are;

$$\overline{b}_y^{sea}(q,s) = \frac{-\mu_0 \mathrm{P}}{\pi s^2} \int_0^\infty \left(\frac{s\mu_0}{u_0+u_1} + \frac{p^2(u_0-u_1)}{\mu_0(\sigma_1 u_0 + \sigma_0 u_1)} \right) \exp(-\mu_0 z)\cos(px)dp \quad (4.25)$$

$$\overline{b}_y^{earth}(q,s) = \frac{\mu_0 \mathrm{P}}{\pi s^2} \int_0^\infty \left(\frac{s\mu_1}{u_0+u_1} + \frac{p^2(u_0-u_1)}{\mu_0(\sigma_1 u_0 + \sigma_0 u_1)} \right) \exp(\mu_1 z)\cos(px)dp \quad (4.26)$$

$$i\overline{e}_y^{sea}(q,s) = \frac{-q\mathrm{P}}{\pi\sigma_0 s^2} \int_0^\infty \left(\frac{ps}{u_0+u_1} + \frac{p\mu_0(u_0-u_1)}{\mu_0(\sigma_1 u_0 + \sigma_0 u_1)} \right) \exp(-\mu_0 z)\sin(px)dp \quad (4.27)$$

$$i\overline{e}_y^{earth}(q,s) = \frac{-q\mathrm{P}}{\pi\sigma_1 s^2} \int_0^\infty \left(\frac{ps}{u_0+u_1} - \frac{p\mu_0(u_0-u_1)}{\mu_0(\sigma_1 u_0 + \sigma_0 u_1)} \right) \exp(\mu_1 z)\sin(px)dp \quad (4.28)$$

where

$$u_i = \sqrt{p^2 + q^2 + \mu_0\sigma_i s}\ , \quad (4.29)$$

p is the x-wavenumber and σ_i represents the i^{th} layer below the seafloor. This solution is used to define the fields of a source dipole and also to test the finite element solution in the (q,s)-domain.

4.5 Response Parameters

In this section, a pair of electromagnetic response parameters defined by Edwards & Chave (1986) will be described. These parameters will be used in chapters 5 through 8 to discuss the modelling results.

A measurement of the transient magnetic field component $\mathbf{B}_y(t)$ following a step-on of source current at time t=0 s is termed the *step*-response. The step-on source dipole

has a current/unit length of the form $\lambda(t) = \lambda_0 u(t)$ where $u(t)$ is the Heaviside function

$$u(t) = \begin{cases} 0, & \text{if } t \leq 0 \\ 1, & \text{if } t > 0 \end{cases} \tag{4.30}$$

If an impulse-current source is used instead of a step-on current, the measured response is described as the *impulse*-response, $\dot{\mathbf{B}}_y\ (t)$. The impulse-response may be obtained from the step response by simply taking its time derivative. *i.e.*

$$\dot{\mathbf{B}}_y\ (t) = \frac{\partial \mathbf{B}_y}{\partial t} \tag{4.31}$$

The impulse-response is often used instead of the step-response because the former better illustrates the change in the fields.

Response Parameters

The first response parameter is the *diffusion time*, τ (Edwards & Chave, 1986), which may be defined as the time at which the impulse-response at some location attains its maximum amplitude. *i.e.*

$$\dot{\mathbf{B}}_y\ (t)|_{t=\tau} = \max \dot{\mathbf{B}}_y\ (t) \tag{4.32}$$

The diffusion time is characteristic of the electrical conductivity, and is considered the *arrival* time of the magnetic signal at a given location in the conductor. The other response parameter of interest is the maximum value of the impulse-response itself;

$$\max \dot{\mathbf{B}}_y\ (t) = \dot{\mathbf{B}}_y\ (\tau) \tag{4.33}$$

Although these response parameters have been defined here in terms of the magnetic field, equivalent parameters may be defined using the electric field.

The time domain skin depth, δ^t, is the distance at which the exponential damping factor equals $1/e$. More precisely,

$$\delta^t = \sqrt{\frac{2t}{\mu_0 \sigma}} \tag{4.34}$$

(Spies & Frischknecht, 1991). Following the transmission of an EM signal at the source, the field components at a given location in the conductor are said to have reached *late* time when the distance from the source (ρ) is much greater than one skin depth, *i.e.* $\rho \gg \delta^t$. Thus, the definition of skin depth in the time domain may be used to quantify the concept of late time. A similar expression for the skin depth is defined by Everett (1990) in the Laplace domain,

$$\delta^s = \sqrt{\frac{2}{\mu_0 \sigma s}}. \tag{4.35}$$

Chapter 5

Implementation and Testing of Finite Element Algorithm

5.1 Introduction

In this chapter, the finite element (FE) method will be introduced and used to numerically solve the EM diffusion equations presented in chapter 4. A forward modelling FE computer algorithm will also be presented. This computer program was developed by Everett (1990) to help design ridge-going experiments and assist interpretation of mid-ocean ridge (MOR) transient CSEM data sets as they become available. Everett (1990, 1989) developed this program for use on a CRAY XMP/24 supercomputer. I have modified this program to run on a Fujitsu VPX240/10 supercomputer for modelling sedimentary seafloor environments.

The algorithm discussed here provides a solution to the transient 2.5D problem. The program calculates the theoretical EM fields generated in a 2D Earth after activation by a 3D horizontal electric dipole (HED) source at the seafloor. In short, the FE approximations to the along-strike magnetic $\overline{b}_y(q,s)$ and electric $i\overline{e}_y(q,s)$ field components are obtained in the spatial wavenumber (q) and Laplace frequency (s) domains. Then the Gaver-Stehfest inverse Laplace transform is used to transform the components into the time-domain. Finally, sine and cosine transforms are used to transform the compo-

nents into the space-domain giving $\mathbf{B}_y(y,t)$ and $\mathbf{E}_y(y,t)$. This algorithm is discussed in greater detail in this chapter.

Contoured snap-shots of the fields, *e.g.* $\mathbf{B}_y(x,0,z,t)$, are instructive for examining the interaction of the EM fields with the inhomogeneous conducting Earth. However, to study the geophysical response, examination of $\mathbf{B}_y(x,y,0,t)$ and $\mathbf{E}_y(x,y,0,t)$ is required. For example, plots of $\mathbf{B}_y(x)$ or $\mathbf{B}_y(t)$ correspond to the information that would be recorded on the seafloor, and provide valuable information about the time and magnitude of response expected.

As mentioned in chapter 4, the solutions are found for only the field components in the along-strike y direction. However, although it is not a simple task, the remaining field components can be derived from these components if desired. This would require computing the spatial (x and z) derivitives of the fields given in equations 4.17, 4.18, 4.21, and 4.22.

Section 5.2 of this chapter presents the necessary FE theory and sets up the numerical solution of the EM fields. In §5.3 the convergence properties of the FE approximation are described and an extrapolation formula is presented. Sections 5.4 and 5.5 discuss the implementation of the numerical algorithm and present results for a simple double half-space model on which the FE algorithm is tested for accuracy. Section 5.6 shows the results for a layered half-space.

5.2 2.5D Finite Element Solution

Perturbed boundary value problem

Recall from §4.3 that the electromagnetic boundary value problem (BVP) contains a singularity at the point at which the source current is applied. This singularity must be avoided (to make the numerical problem well-posed) by slightly altering the numerical

representation of the BVP (Everett, 1990). In this section of the thesis, the finite element solution of a perturbed BVP based on the system of PDEs (4.24) will be discussed.

A function $u(r)$ which satisfies the linear differential equation

$$Lu(\mathbf{r}) = 0, \quad \mathbf{r} \in \Omega \tag{5.1}$$

where L is a differential operator, is said to be a *classical* solution. The finite element method, however, is based on the *weak* solution which satisfies only

$$(Lu, v)_\Omega = 0 \tag{5.2}$$

for all measurable admissible test functions $v(r)$ (*e.g.* Wait, 1986), where $(\cdot,\cdot)$ is the L_2 inner product

$$(u, v)_\Omega = \int_\Omega uv \, d\mathbf{r} \tag{5.3}$$

Since a singularity exists in the solution domain Ω at $r = 0$ for the seafloor EM problem, a new solution domain, $\Omega_h \subset \Omega$, must be established to keep the problem well-posed (Everett, 1990). This is done by cutting a hole out of the original domain Ω around the applied current source, thus avoiding the problem of the singularity. The result is a perturbed BVP given by

$$(Lu^h, v)_{\Omega_h} = 0 \tag{5.4}$$

with solution u^h. The boundary of Ω_h then is given by $\partial\Omega_h = \partial\Omega_{h_0} + \partial\Omega_{h_1}$ where $\partial\Omega_{h_0}$ is the outer boundary and $\partial\Omega_{h_1}$ is the inner boundary which is the hole in Ω_h around the source. The new solution domain and boundaries are shown in figure 5.1.

The inner boundary, $\partial\Omega_{h_1}$, is placed sufficiently close to the source so that the solution $u^h(\mathbf{r}_1), \mathbf{r}_1 \in \partial\Omega_{h_1}$ may be approximated by the analytic double half-space solutions in equations 4.25 to 4.28 (Everett, 1990). For the current problem, the outer

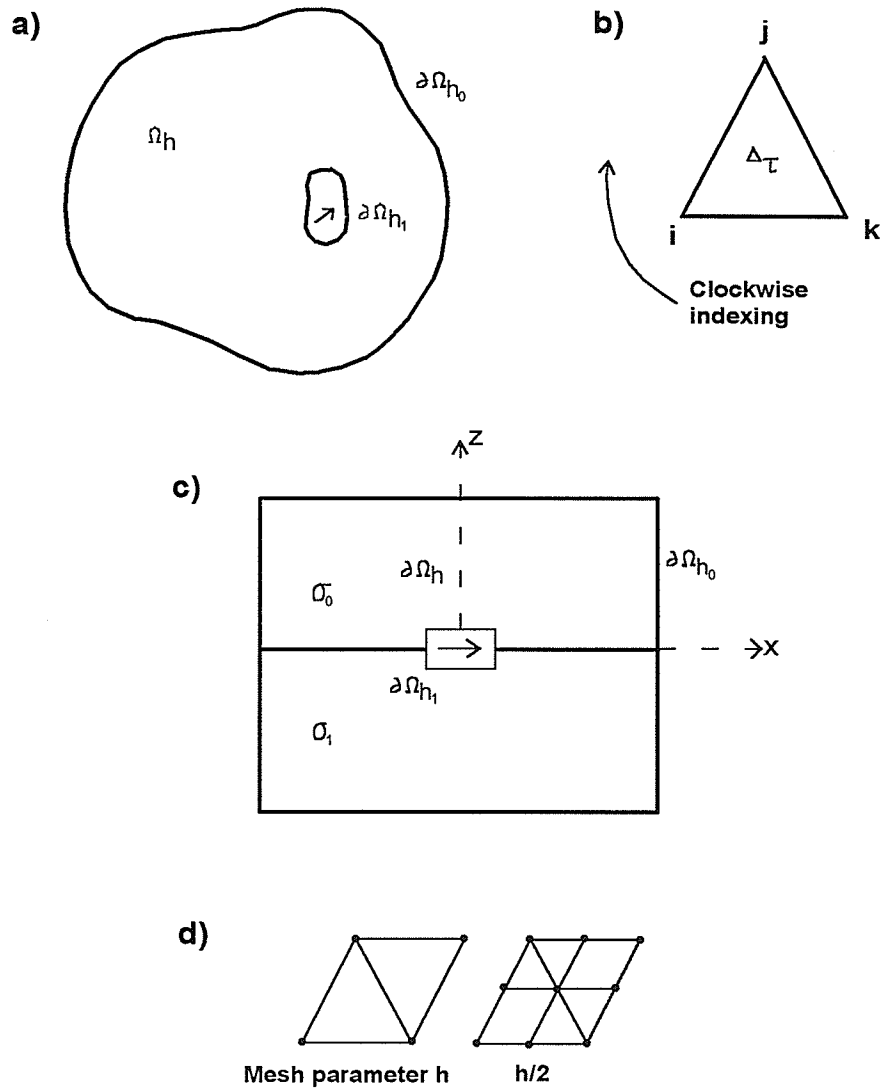

Figure 5.1 (a) Illustration of a perturbed domain Ω_h with outer and inner boundaries $\partial\Omega_{h_0}$ and $\partial\Omega_{h_1}$ (from Everett, 1990). (b) The domain Ω_h, is partitioned into a set of non-overlapping triangles or finite elements. Linear interpolation is performed over the τ^{th} triangle by a polynomial asociated with the i^{th} node. (c) The resultant 2D model. (d) The accuracy of the FE solution depends greatly on triangle size. A mesh with triangle size $h/2$ can be generated from a mesh of size h as illustrated.

boundary is placed far enough from the source such that the solution $u^h(\mathbf{r_0}) = 0, \mathbf{r_0} \in \partial\Omega_{h_0}$. This method works well, however, it necessitates a fairly large FE mesh. In electrical engineering scattering and radiation problems, absorbing boundary conditions are used at an outer boundary placed much closer to the structure of interest (Chatterjee *et al.*, 1993). The advantage with this method is a much reduced matrix size.

Finite element formulation

The first step in the finite element method is to partition the solution domain Ω_h into a mesh of N_T non-overlapping triangular elements. The vertices of these triangles are the nodes at which the solution u^h is to be approximated (Everett, 1990). A finite element approximation is based on the weak solution (5.2) by defining an approximate solution $\widetilde{u}$ as a finite sum of specified basis functions α_i. That is, a solution with the form

$$\widetilde{u}=\sum_{i=1}^{N} a_i\alpha_i(x,z) \tag{5.5}$$

The basis function α_i is associated with the i^{th} node of a total of N nodes, while a_i is an unknown coefficient. Each basis function is then represented by a set of piecewise 2D interpolating polynomials:

$$\alpha_i(x,z) =\sum_{\tau=1}^{N_T} \alpha_i^{\tau}(x,z), \quad i = 1,2,...,N. \tag{5.6}$$

where α_i^{τ} is associated with the i^{th} node and the τ^{th} triangle. The interpolating polynomials are chosen to be of first order in the formulation of Everett (1990), thus interpolation over each triangle is linear. The interpolating polynomials have the property that they are only non-zero at the node to which they are associated. That is

$$\alpha_p^{\tau}(x_q,z_q) = \delta_{pq}, \quad \forall p \in (i,j,k),\ q \in (i,j,k) \tag{5.7}$$

where δ_{pq} is the Kronecker delta function. It is apparent from (5.7) that the basis function

$\alpha_i = N_{i,T}$ where $N_{i,T} < N_T$ is the total number of triangles which have node i as a vertex.

The 2.5D BVP may be expressed in terms of the five equations (Everett, 1990)

$$\Lambda \begin{pmatrix} \overline{b}_y^h \\ i\overline{e}_y^h \end{pmatrix} = 0 \quad (x,z) \in \Omega_h,\ q \geq 0,\ s > 0 \tag{5.8}$$

$$\overline{b}_y^h(x_0, q, z_0, s) = 0 \quad (x_0, z_0) \in \partial\Omega_{h_0} \tag{5.9}$$

$$i\overline{e}_y^h(x_0, q, z_0, s) = 0 \quad (x_0, z_0) \in \partial\Omega_{h_0} \tag{5.10}$$

$$\overline{b}_y^h(x_1, q, z_1, s) = \begin{cases} \overline{b}^{sea}(x, q, z, s) & z > 0 \\ \overline{b}^{earth}(x, q, z, s) & z < 0, \end{cases} \quad (x_1, z_1) \in \partial\Omega_{h_1} \tag{5.11}$$

$$i\overline{e}_y^h(x_1, q, z_1, s) = \begin{cases} \overline{e}^{sea}(x, q, z, s) & z > 0 \\ \overline{e}^{earth}(x, q, z, s) & z < 0, \end{cases} \quad (x_1, z_1) \in \partial\Omega_{h_1} \tag{5.12}$$

where Λ in (5.8) is the 2×2 partial differential operator matrix in (4.24). The outer boundary conditions are represented by (5.9) and (5.10) and the inner boundary conditions are represented by (5.11) and (5.12).

As described earlier, the FE mesh contains N nodes in total. There are M_0 nodes on the outer boundary and M_1 nodes on the inner boundary with a total of $M = M_0 + M_1$. This leaves $N - M$ nodes in the interior of the mesh. Following the form of (5.5), the finite element approximation of the BVP can then be written as a linear combination of the basis functions α_j,

$$\overline{u}^h \equiv \begin{pmatrix} \overline{b}_y^h \\ i\overline{e}_y^h \end{pmatrix} = \sum_{j+1}^{N-M} \begin{pmatrix} a_{1j} \\ a_{2j} \end{pmatrix} \alpha_j(x,z) + \sum_{k=N-M_1+1}^{N} \begin{pmatrix} b_{1j} \\ b_{2j} \end{pmatrix} \alpha_k(x,z) \tag{5.13}$$

where the first term on the right side is the solution on each node on the interior of the mesh and the second term is the solution on each node on the inner boundary which is matched exactly with the double half-space analytical solution (Everett, 1990).

The finite element solution u^h must satisfy the set of equations

$$\left(\Delta\overline{u}^h, \begin{pmatrix} \alpha_l \\ \alpha_l \end{pmatrix}\right)_{\Omega_h} = 0, \quad l = 1, 2, ..., N - M \tag{5.14}$$

which can be re-written in the matrix form:

$$\mathbf{\Gamma a} = \mathbf{g} \tag{5.15}$$

where the solution $\mathbf{a}$ is given by the 2-vector

$$\begin{pmatrix} a_{1j} \\ a_{2j} \end{pmatrix} = \begin{pmatrix} \overline{b}_y^h(x_j, z_j) \\ i\overline{e}_y^h(x_j, z_j) \end{pmatrix} \quad j = 1, 2, ..., N - M \quad , \tag{5.16}$$

the RHS vector $\mathbf{g}$ is the 2-vector

$$g_l = \begin{pmatrix} g_{1j} \\ g_{2j} \end{pmatrix} = - \sum_{k=N-M_1+1}^{N} \Gamma_{kl} \begin{pmatrix} \overline{b}_y^h(x_k, z_k) \\ i\overline{e}_y^h(x_k, zk) \end{pmatrix}, \tag{5.17}$$

and the finite element matrix $\mathbf{\Gamma}$ is comprised of elements Γ_{jl} that are in themselves defined by the 2×2 matrix

$$\Gamma_{jl} = \begin{pmatrix} \beta_{jl} - s(\alpha_j, \alpha_l)_{\Omega_h} & q\gamma_{jl} \\ q\gamma_{jl} & \beta'_{jl} - \mu_0\sigma(\alpha_j, \alpha_l)_{\Omega_h} \end{pmatrix} \tag{5.18}$$

where the elements of Γ_{jl} are expressed in terms of inner products over derivatives of the basis functions. That is,

$$\beta_{jl} = -\left(\frac{s}{u^2}\frac{\partial\alpha_j}{\partial x}\frac{\partial\alpha_l}{\partial x}\right)_{\Omega_h} - \left(\frac{s}{u^2}\frac{\partial\alpha_j}{\partial z}\frac{\partial\alpha_l}{\partial z}\right)_{\Omega_h} \tag{5.19}$$

$$\beta'_{jl} = -\left(\frac{\mu_0\sigma}{u^2}\frac{\partial\alpha_j}{\partial x}\frac{\partial\alpha_l}{\partial x}\right)_{\Omega_h} - \left(\frac{\mu_0\sigma}{u^2}\frac{\partial\alpha_j}{\partial z}\frac{\partial\alpha_l}{\partial z}\right)_{\Omega_h} \tag{5.20}$$

$$\gamma_{jl} = -\left(\frac{1}{u^2}\frac{\partial\alpha_j}{\partial x}\frac{\partial\alpha_l}{\partial z}\right)_{\Omega_h} - \left(\frac{1}{u^2}\frac{\partial\alpha_j}{\partial z}\frac{\partial\alpha_l}{\partial x}\right)_{\Omega_h} \tag{5.21}$$

Solving this system of equations gives the finite element approximation of $\overline{b}_y(q, s)$ and $i\overline{e}_y(q, s)$ on the interior nodes of the mesh. The transient solutions $\mathbf{B}_y(y, t)$ and $\mathbf{E}_y(y, t)$ are then found via an inverse Laplace transform and an inverse sine or cosine transform which will be discussed in §5.4.

5.3 Convergence of FE solution

There are two distinct types of errors involved when solving a perturbed BVP using a numerical method such as finite elements (Mitchell & Wait, 1977). The first type, $||u- \tilde{u}||$, is the *approximation error* which is due to the FE approximation. The second, $||u-u^h||$, is the *perturbation error*, which is due to the numerical implementation of the solution and include, for the current problem, interpolated boundary conditions and boundary approximation. If the perturbation errors are of smaller order in h than the approximation error, the FE solution is said to be *optimal* (Mitchell & Wait, 1977). The parameter h is a measure of triangle size and is illustrated in figure 5.1. A mesh may be made finer by sub-division of each existing triangle into four triangles by insertion of an extra node at the mid point of each element. The new mesh has triangles of size $h/2$ (Everett, 1990). As discussed by Everett (1990), there have been few if any theoretical bounds placed on the perturbation errors for solutions of BVPs with one or more singularities (*e.g.* CSEM). However, based on studying related problems, Everett (1990) found that the perturbation error for the current problem is at best

$$\left\|\mathbf{B}_y - \mathbf{B}_y^h\right\| = O(h^{3/2}) \tag{5.22}$$

and that with linear interpolating polynomials and triangular partitioning of Ω_h, the approximation error is at best

$$\left\|\mathbf{B}_y - \tilde{\mathbf{B}}_y^h\right\| = O(h) \tag{5.23}$$

where $\mathbf{B}_y$ is the exact solution on Ω, $\mathbf{B}_y^h$ is the exact solution on Ω_h, and $\tilde{\mathbf{B}}_y^h$ is the FE approximation on Ω_h.

To evaluate the convergence of the FE approximation to the 2.5D problem, Everett (1990) compared the output from the finite element program with the analytic solution in (4.25) to (4.28). Two meshes were used; a coarse mesh with N=736 nodes and triangles

of size h, and a finer mesh with $4N \approx 2880$ nodes and triangle size $h/2$. The finer mesh was generated from the coarse one by division of each triangle into four as discussed above. Everett found that by using a mesh of size $h/2$, the percent relative error for both components is decreased by a factor of two (from $\sim$16% to $\sim$8%) everywhere except near the source. This indicates that the convergence rate of the solution is $O(h)$ and the implementation of the FE approximation is optimal.

Everett (1990) describes an extrapolation technique which permits the use of relatively coarse meshes to realize very low (1-3%) relative errors. If the convergence rate of the FE solution is exactly $O(h)$, then the solution for the fields on a mesh of size $h/2$ should lie half way between the solution on mesh of size h and the analytical solution, *i.e.*

$$\bar{b}_y = 2\bar{b}_y^{h/2} - \bar{b}_y^{h} \tag{5.24}$$

where $\bar{b}_y^{h}$ is the numerical solution on mesh of size h, and $\bar{b}_y^{h/2}$ is the numerical solution on the mesh of size $h/2$. Everett (1990) found that the above relation was always satisfied to less than 3% relative accuracy. These results suggest that (5.24) can be used to attain highly accurate solutions even when the solutions $\bar{b}_y^{h}$ and $\bar{b}_y^{h/2}$ are relatively poor approximations to the analytic solution. However, the $O(h)$ convergence has only been demonstrated for a double half-space. Testing of the convergence properties on a layered half-space would be useful in determining the generality of this extrapolation formula.

5.4 Implementation of the Finite Element Method

This section will be devoted to describing, in detail, the steps in computing the EM fields via the FE method. Figure 5.2 shows a flowchart of the main processes involved in the FE algorithm. The first step is to develop a model and create a finite element

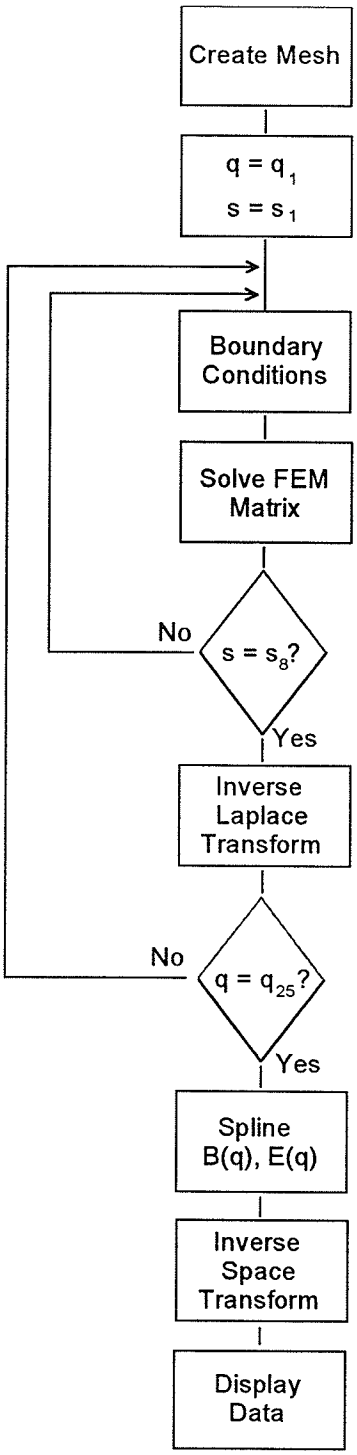

Figure 5.2 Flowchart detailing the steps involved in the numerical implementation of the FE method for solving the EM BVP described in §5.2.

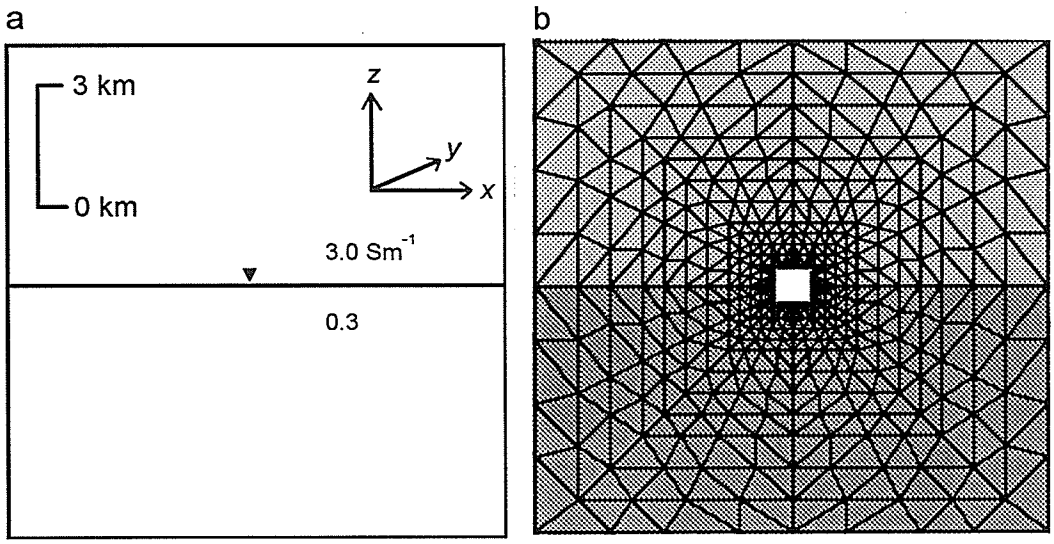

Figure 5.3 Double half-space model (a) and its finite element mesh (b). The FE mesh shown is only a small portion of the actual mesh used in calculating the fields (which contains approximately 1200 nodes). The source is located in the central cut-out portion of the mesh.

mesh of that model. The model I will use in §5.4 and §5.5 is a simple double half-space (DHS). This model will be used to illustrate the steps in the numerical solution of the EM fields and to test the solution for accuracy against an analytical solution.

The model

The 2D model considered is shown in figure 5.3a. As discussed in §4.3, a Cartesian coordinate system is employed with z vertically upwards and the conductivity invariant in the y-direction; the source is x-directed. The plane $z = 0$ divides the upper homogeneous region $z > 0$ representing the sea water from a lower half-space $z < 0$ of variable conductivity $\sigma(x, z)$ representing the inhomogeneous earth.

The model must be first partitioned into a mesh of non-overlapping triangular elements with the unknown field values located at the vertices of these triangles (figure 5.3b). The aim while meshing is to minimize the errors associated with the finite element

solution. However, the amount of computer cpu time has been found to increase as $N^{3/2}$ (Everett & Edwards, 1989) and should be kept in mind. It is therefore important to completely and accurately define the mesh structure without using too many superfluous nodes.

Mesh parameters

Everett (1990) developed a set of mesh parameters used to specify the mesh structure. The set includes the geometric spacing of the nodes g, the number of nodes N, and the distance d_0 of the inner boundary $\partial\Omega_0$ of the mesh and the distance d_1 of the outer boundary $\partial\Omega_1$ of the mesh from the source (the point of singularity). The geometric spacing g (figure 5.4) measures the rate of increase of the distance between nodes as the distance from the source increases. The optimum distance of the inner boundary from the point of singularity is dependant on g. The inner boundary condition forces the field values of the nodes on the inner boundary to be that of the semi-analytical solution. For this reason, the inner boundary must be a sufficient distance from the singularity to ensure accurate representation of the source, but close enough to maintain the accuracy of the FE mesh.

Due to the fact that the EM fields decay exponentially with distance from the source, the nodes should be spaced approximately logarithmically with distance from the source. Everett (1990) found that the best results were obtained when the input parameters were set to $g \simeq 1.5$, and $d_1=0.1\delta_1^s$ where δ_1^s is the Laplace skin depth in the seafloor (translating to about $d_1=100$ m for $\sigma_1=0.3$ Sm^{-1}). The distance to the outer boundary $\partial\Omega_{h0}$ must be sufficiently large that the fields have effectively decayed to zero ($d_0=75$ km is sufficient); this is the outer boundary condition.

I have found that it is also important to increase node density at model locations corresponding to sites where actual measurements might be made (*i.e.* on the seafloor

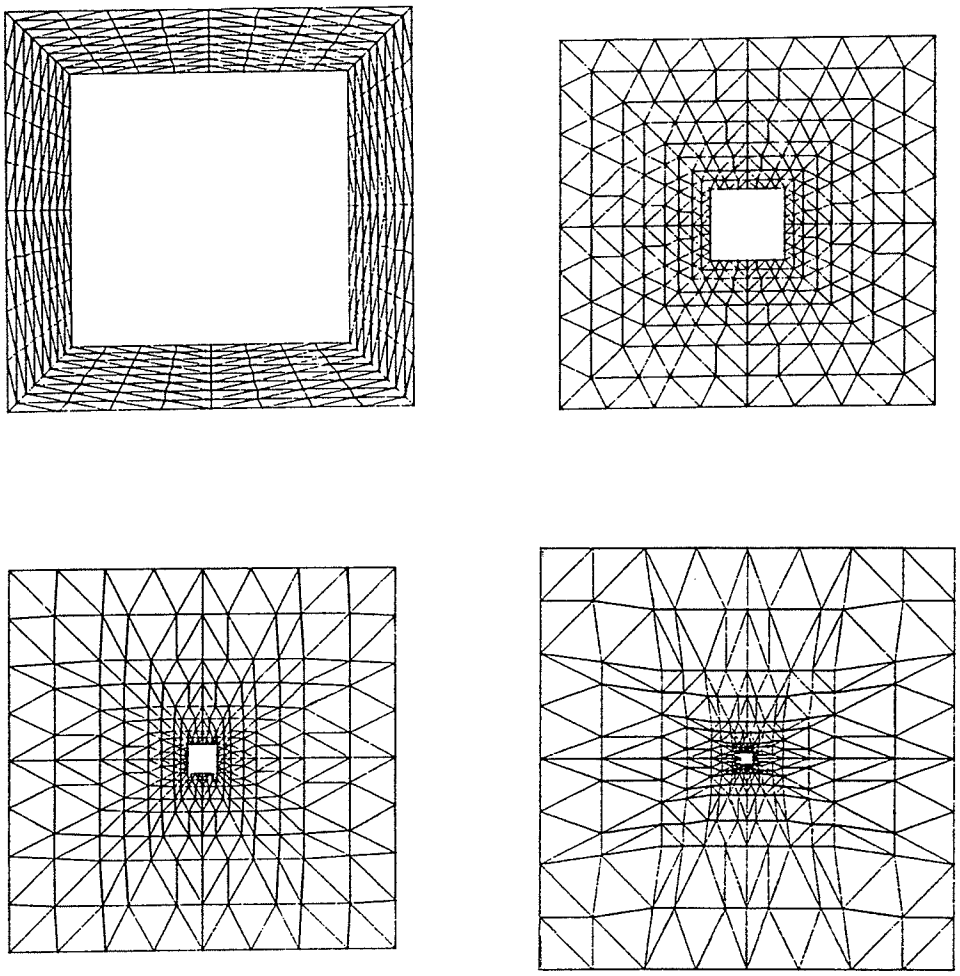

Figure 5.4 Some sample finite element meshes constructed with values of the geometric spacing, g, ranging from 1.1 at top left to 2.4 at bottom right (from Everett, 1990). The factor g is a measure of the increasing distance between nodes with increasing distance from the source.

over the structure being modelled). This procedure has the two-fold advantage of creating more output points for plotting geophysical data and reducing the data error in these areas of interest.

The model space is subdivided into polygonal areas, each of uniform conductivity, and conforming to the constraints above. The vertices of these polygons are then fed into the mesh generator TRIMESH written by Travis (1987) and modified by Everett (1990). This program automatically partitions the model into triangular elements and orders the nodes to minimize the bandwidth of the FE matrix.

Matrix equation

As described in §5.2, a matrix equation for the unknown field values $\overline{b}_y$ and $i\overline{e}_y$ is constructed with the matrix entries on the left-hand side dependent only on the mesh structure and the governing field equations. This matrix is sparse and banded (*e.g.* Zienkiewicz & Taylor, 1989). The RHS vector contains the boundary conditions. As stated before, the solution at the nodes on a cut out portion around the source is matched exactly to the analytic solution for the source given by equations 4.25 to 4.28. Also, it is presumed that the fields will effectively decay to zero at a large enough distance from the source. The solution of this matrix is found using the LU decomposition and Gaussian elimination routines from the NAG library (1993).

Inverse Laplace Transform

The algorithm employs the Gaver-Stehfest (GS) method to invert from the Laplace domain $\overline{b}_y(q,s)$ and $i\overline{e}_y(q,s)$ to the time-domain $\overline{b}_y(q,t)$ and $i\overline{e}_y(q,t)$ (Everett & Edwards, 1992; Everett, 1990). The GS algorithm provides accurate results for smooth, non-oscillatory functions of time by combining a small number of weighted Laplace domain solutions for real s. It is particularly useful for electromagnetic induction studies (Edwards & Cheesman, 1987). The GS formula for inverting an arbitrary function $f(s)$

is

$$f(t) \simeq \frac{\ln 2}{t} \sum_{n=1}^{\mathrm{N_c}} c_n f(s_n) \tag{5.25}$$

where the Laplace frequencies are

$$s_n \equiv \frac{n \ln 2}{t}, \quad n = 1, 2, ..., \mathrm{N_c} \tag{5.26}$$

and the GS coefficients are

$$c_n = (-1)^{n+\frac{\mathrm{N_c}}{2}} \sum_{k=\frac{n+1}{2}}^{\min[n, \frac{\mathrm{N_c}}{2}]} \frac{k^{\frac{\mathrm{N_c}}{2}} (2k)!}{(\frac{\mathrm{N_c}}{2} - k)!\, k!\, (k-1)!\, (n-k)!\, (2k-n)!} \tag{5.27}$$

(Everett & Edwards, 1989). The choice of $\mathrm{N_c}$ depends on machine precision and $\mathrm{N_c}$=8 has been found to be appropriate for use on a CRAY XMP/24 (Everett & Edwards, 1992) and on a FUJITSU VPX240/10 (Boyce & Ferguson, 1994, 1995). This means that the solution for the fields over the FE mesh needs to be calculated for 8 values of s.

As mentioned in §4.3, the main reason for solving equation (4.24) in the Laplace frequency domain rather than working directly in the time domain is to save cpu time. In cases such as the current problem, where a solution is desired at only a few selected times, the s-domain method aviods the potential waste of computer resources in time-stepping the solutions from t=0 s. If a "continuous" set of solutions were desired, working directly in the time-domain may be more advantageous by not carrying the Laplace to time-domain transformation.

Inverse space-transform

The cosine and sine transforms

$$B_y(x, y, z, t) = \frac{1}{\pi} \int_0^{\infty} \overline{b}^h(x, q, z, t)\, \cos(qy)\, dq \tag{5.28}$$

$$E_y(x, y, z, t) = \frac{1}{\pi} \int_0^{\infty} i\overline{e}^h(x, q, z, t)\, \sin(qy)\, dq \tag{5.29}$$

are used to retrieve the EM fields in the space-domain. These transforms are relatively time consuming because of the approximately exponential decay of the EM fields in space. The kernels of the transforms are the field values $\overline{b}^h(x,q,z,t)$ and $i\overline{e}^h(x,q,z,t)$ computed by the FE and GS methods. The magnetic and electric fields are calculated for a range of q values, and then a bi-cubic spline interpolater is employed (in the log-domain) to compute more finely spaced values. Calculation of the fields for 25 values of q spaced logarithmically over 5 decades (10^{-6} to 10^{-1} m^{-1}) works well for a seafloor environment with conductivity values between 10^{-3} and 10^{-1} $S.m^{-1}$ (Boyce & Ferguson, 1995). The implementation of the bi-cubic spline uses a routine from the NAG (1993) mathematics software library. These inverse Fourier transforms (also those in equations 4.25 to 4.28), are evaluated using the algorithm of Chave (1983). This algorithm integrates the product of the kernel and the trigonometric function between zero crossings of the latter and sums the resulting series of partial integrations using a continued fraction expansion. The algorithm convergence has been found to be sensitive to small erratic field values at large values of q. A poor choice of the set of wavenumber values can therefore lead to excessive computer cpu usage.

5.5 Illustration and Testing of the Finite Element Algorithm

When using a computer program involving many data transformations and a large matrix inversion such as the program used in this research, it is important to carefully test the program results. The computed EM field values for the DHS model in figure 5.3 are compared to the semi-analytical solution in the q-s domain, the q-t domain and the y-t domain. It is important to note at this point that the field values are not zero everywhere outside the last contour line shown in the following figures. This set of contours was chosen only to aid the illustration of the form of the fields in the q-s

domain. A similar result applies for all contour plots throughout the thesis.

q-s domain solutions

The first step in the FE program is to calculate the magnetic and electric fields in the q-s domain. For a single value of the wavenumber q, the magnetic and electric fields must be calculated for 8 values of s. Figure 5.5 shows contours of the magnetic field for s_n (n=1,4,8; s_1=1.4 s^{-1}, s_4=2.8 s^{-1}, and s_8=5.5 s^{-1}) for t=1.0 s and q=$10^{-3}m^{-1}$. These plots demonstrate that the field becomes smaller as the value of s increases (analogous to earlier time). The small irregularities on the outermost contours reflect the limit of numerical accuracy of the solution and its interpolation and contouring. Note also that the fields at this point are 10^{-3} of those near the source. After the EM fields have been calculated for 8 values of s, the fields can be trasformed to the time-domain.

To assess the level of error in the fields at this point in the program, the fields may be compared to the semi-analytical (SA) solution found using equations (5.1) through (5.4). The comparison is only made along the seafloor (z=0 m) as this is where geophysical measurements would be collected in a real marine EM survey. Figure 5.6 compares the FE solution to the SA solution for two values of the wavenumber (q_3=10^{-5} and q_{15}=2.5×10^{-3} m^{-1}; where q_3 and q_{15} are the 3^{rd} and 15^{th} wavenumbers respectively). The results in figure 5.6 are representative of the small and mid-range q values used in the program. The small value of s_4 (0.01 s^{-1}) corresponds to very late time ($t \approx$ 275 s), and the large value of s_4 (100 s^{-1}) corresponds to early time ($t \approx$ 0.03 s). In figure 5.6 the solid line shows the SA solution, the crosses show the FE solution on a mesh of size h, and the plusses show the FE solution on a mesh of size $h/2$. For nodes close to the source (<1000 m), the FE solution is inaccurate at small values of s (late times). However, doubling the node density over the entire mesh provides a much improved solution ($h/2$) for the mid-range q values (figure 5.6b). This is expected from

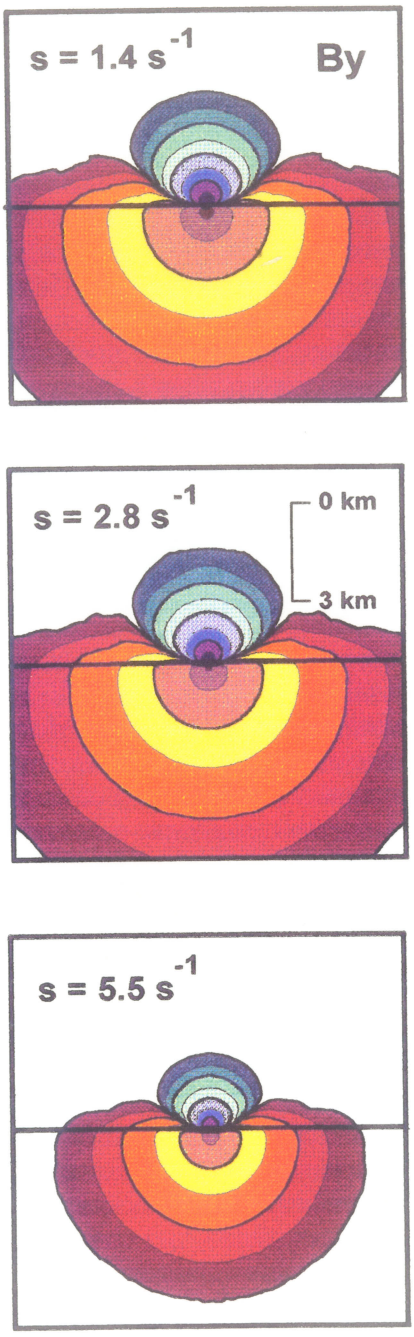

Figure 5.5 Contours (two per decade) of the magnetic field showing change with s for q=10^{-3} m^{-1}. The model used is shown in figure 5.3.

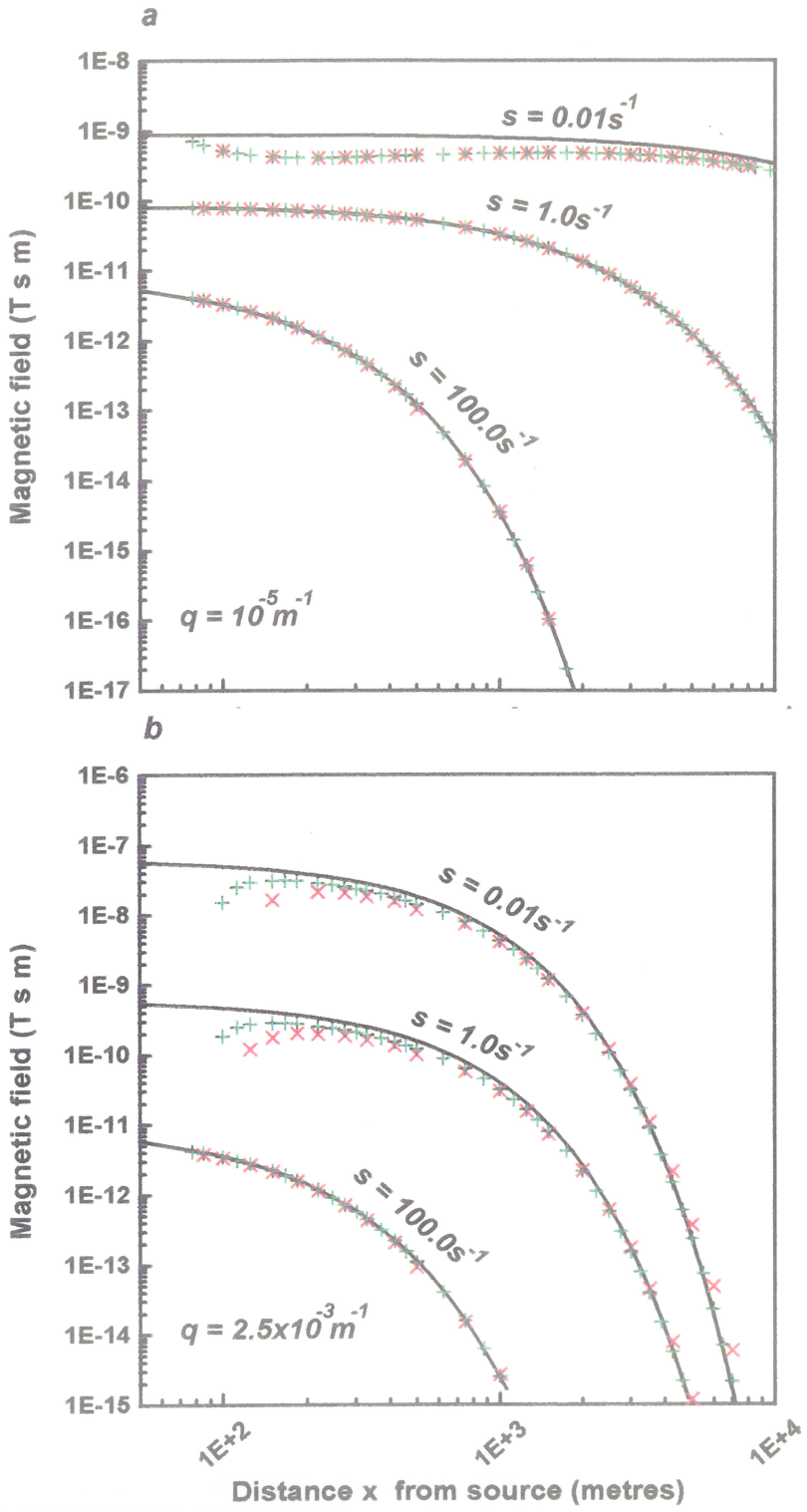

Figure 5.6 Comparison of the semi-analytical (solid line) and finite element solutions of mesh size h (crosses) and $h/2$ (plusses) for three values of the Laplace variable s for (a) q=10^{-5} m^{-1}, and (b) q=2.5×10^{-3} m^{-1}. The solution over the $h/2$ mesh is much more accurate than the solution for the mesh of size h only at very small values of s (equivalent to late time).

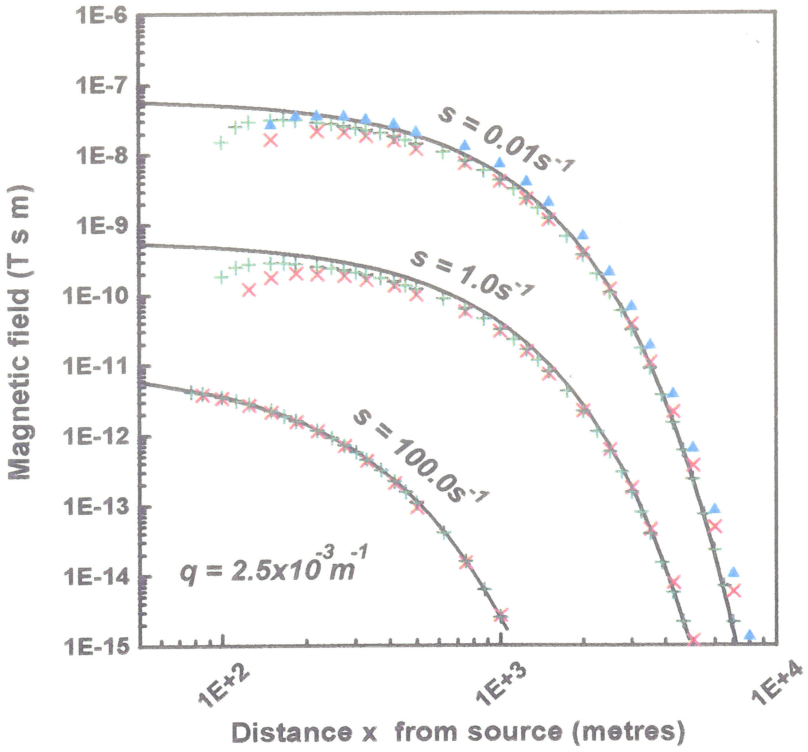

Figure 5.7 Comparison of the information in figure 5.6b with the FE solution (triangles) of a mesh with triangular elements of size $h/2$ within 1000 m of the source and size h further from the source. The local doubling of nodal density does not provide an increased solution accuracy.

the convergence properties discussed in §5.3.

Due to the large field gradients, the FE approximation is poorest near the source. Intuitively, reducing triangle size to $h/2$ near the source only should produce a similar result to reducing triangle size over the entire mesh. The advantage to refining the mesh only near the source is to reduce the total number of nodes N on the mesh and therefore the required computer cpu time for the solution. To test this hypothesis, the nodal density on a mesh of size h was doubled only within 1000 m of the source. The solution on this mesh (triangles) is shown in figure 5.7, plotted against the data from

figure 5.6. Figure 5.7 clearly shows that the mesh size must be globally refined to attain the desired increase in accuracy.

At distances 1000 m$\leq x \leq$7000 m, the FE solutions in figure 5.6 show fairly good agreement with the SA solution even for a mesh of size h. Since the target depth in hydrocarbon exploration is often greater than 500 m, EM receivers would rarely be placed closer than 1 km to the source. Therefore, although an accurate solution close to the source is desired, it is not necessary for the modelling in this thesis.

q-t domain solutions

The fields must be calculated for 25 values of the wavenumber q before they can be transformed to the space-domain. I have found that choosing wavenumbers in the range 2.5×10^{-6} m$^{-1} \leq q \leq 1.6\times10^{-1}$ m^{-1} works well for both the double half-space model examined in this chaper and the more complex models in subsequent chapters. Figure 5.8 shows contours (two per decade) of the magnetic field in the time-domain for three mid-range values of wavenumber q. These plots show that the fields in the q-t domain decrease in magnitude with increasing q.

The fields may also be tested against a semi-analytical solution in the q-t domain. As in the q-s domain, the comparison is made only at points at the seafloor. Figure 5.9 shows the FE solution on meshes of size h (plusses, blue) and $h/2$ (circles, red), the extrapolated solution (solid triangles, green), and the SA solution (open triangles, black) for two seafloor receiver positions. The FE solution is least accurate at wavelengths $(1/q)$ comparable to the distance (x) the receiver is located from the source. These errors are as high as 35%. The extrapolated solution in figure 5.9 shows that the extrapolation formula in §5.3 can be used successfully to obtain a close fit to the analytical solution even when the individual numerical solutions approximate it very poorly. Note, however, that the h solution is poor only close to the source. At sufficient distance from the source

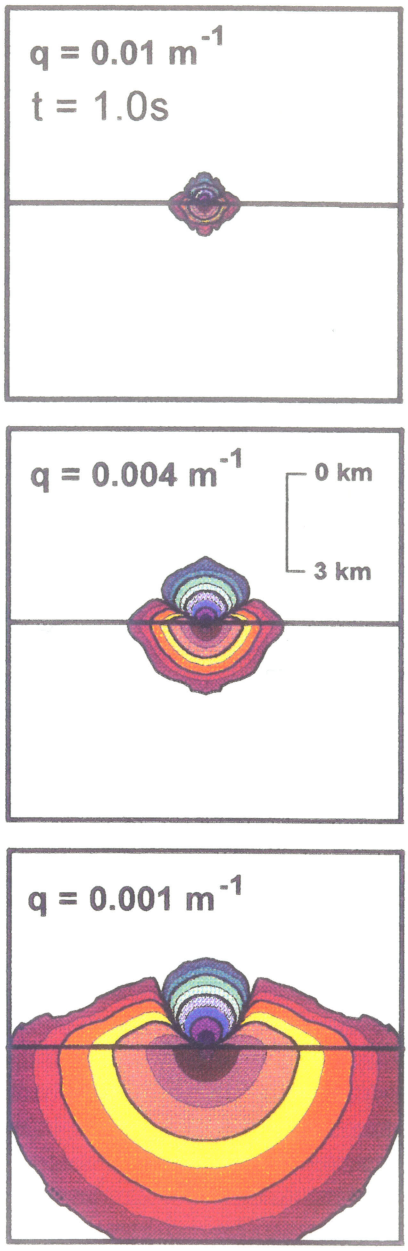

Figure 5.8 Contours (two per decade) of the magnetic field for the DHS in the q-t domain for three mid-range values of q at t=1.0 s. Notice that the field values decrease with increasing q.

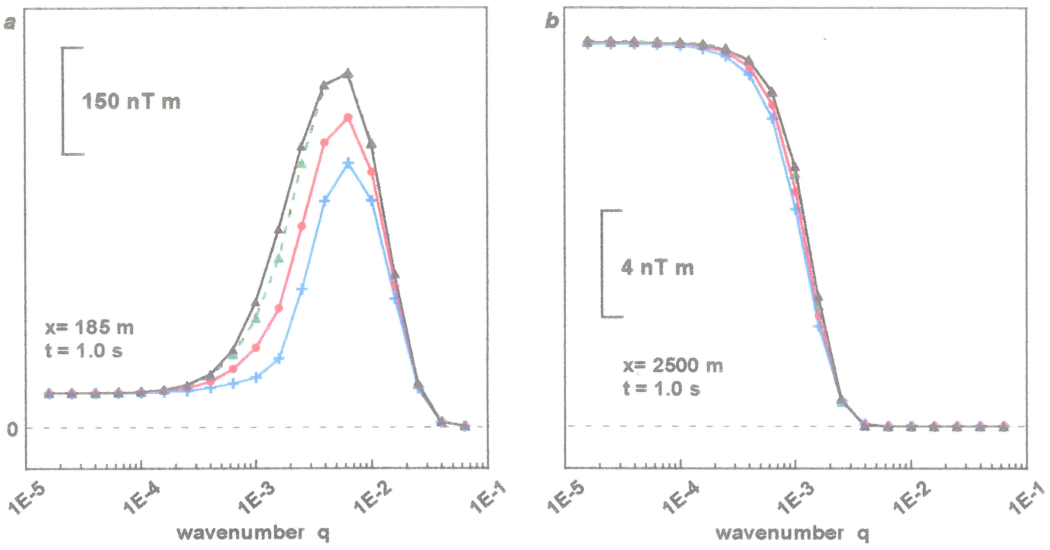

Figure 5.9 Comparison of the SA solution (open triangles) with the FE solution on mesh size h (plusses), $h/2$ (solid circles) and the extrapolated solution (solid triangles) for two receiver locations on the seafloor. The magnetic field is shown at (a) x=185 m, and (b) x=2500 m. The extrapolated solution provides an excellent fit to the analytical solution even though the individual FE solutions are relatively poorer.

($>1\delta$) the h solution provides a reasonably accurate approximation.

y-t domain solution

As indicated in figure 5.2, before transforming the calculated EM fields to the space-domain, a cubic spline is fit to the 25 values of $\bar{b}_y(q,t)$ and $i\bar{e}_y(q,t)$ to obtain 200 values that are more finely spaced. These 200 field values are then used as the kernels in the spacial transforms (equations 5.28 and 5.29). Figure 5.10 demonstrates the fit of the spline to the magnetic field at two seafloor locations.

Figure 5.11 shows contours of the magnetic field after transformation to the space-domain. Note how the fields diffuse faster in the less conductive seafloor and "leak" energy upwards across the sea-seafloor interface. It is this signal that would be measured in a seafloor survey. At late time ($t>1.0$ s), the signal in the more conductive seawater

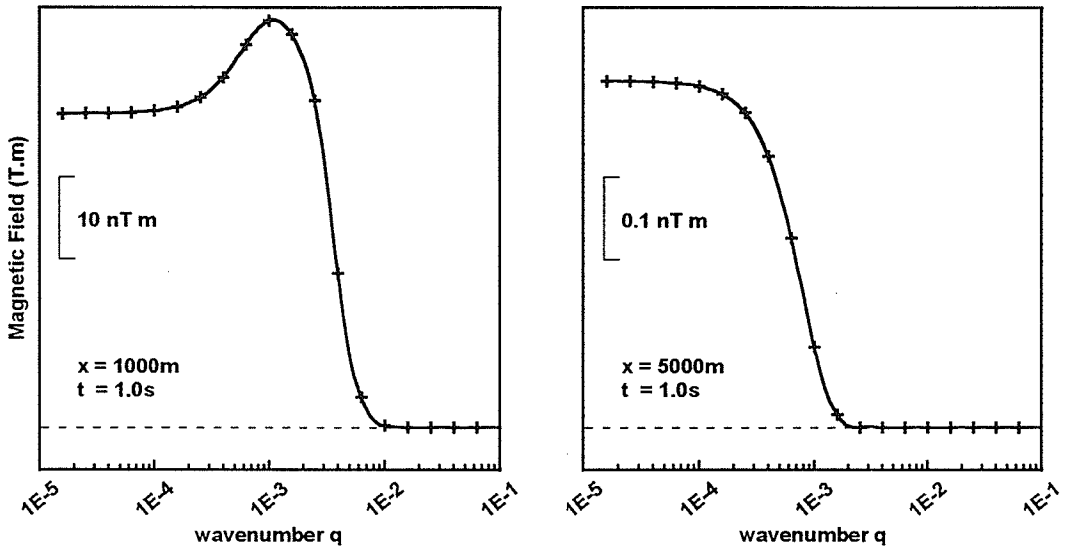

Figure 5.10 Plot showing the fit of the spline interpolated values (solid) used to compute more finely spaced values of $\bar{b}_y(q)$ for use in the spatial transforms.

begins to dominate. That is, by the time the fields in the seawater have diffused out to a specific point at the interface, the fields in the seafloor have already mostly dissipated. The plots in figure 5.11 show $\mathbf{B}_y$ in the (x, z) plane (*i.e.* y=0 m). The along-strike component of the electric field is zero in this plane and therefore can not be shown.

An examination of the accuracy of the FE solution, on a mesh of size h, is presented in figure 5.12. The figure shows both the step (5.12a) and impulse (5.12b) response for the FE solution (solid) and the SA solution (dashed) for six receiver locations on the seafloor. Figure 5.12b shows that the FE approximation provides an accurate representation at the time τ of the maximum impulse response. This is the time used to characterize the "arrival" of signals at a seafloor location.

Calculating the impulse response

As detailed in §4.5, the impulse-response $\dot{\mathbf{B}}_y\ (t)$ is often the response parameter

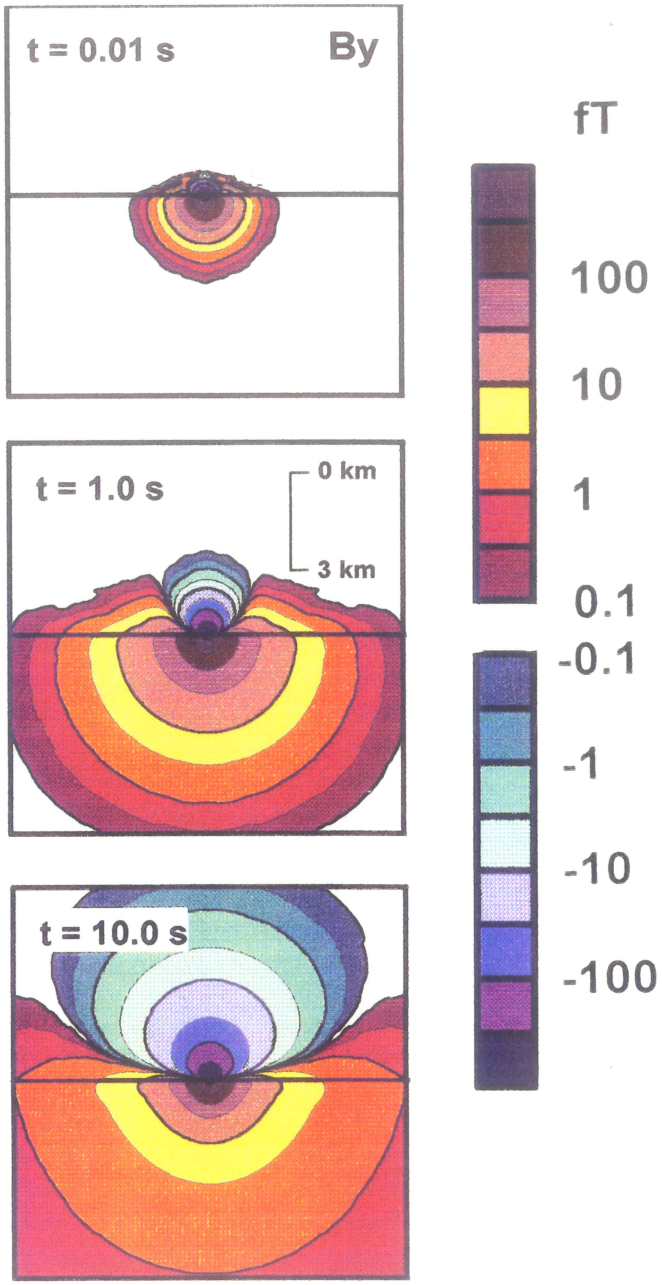

Figure 5.11 Contours (two per decade) of the magnetic field in the (y, t) domain for 3 values of t.

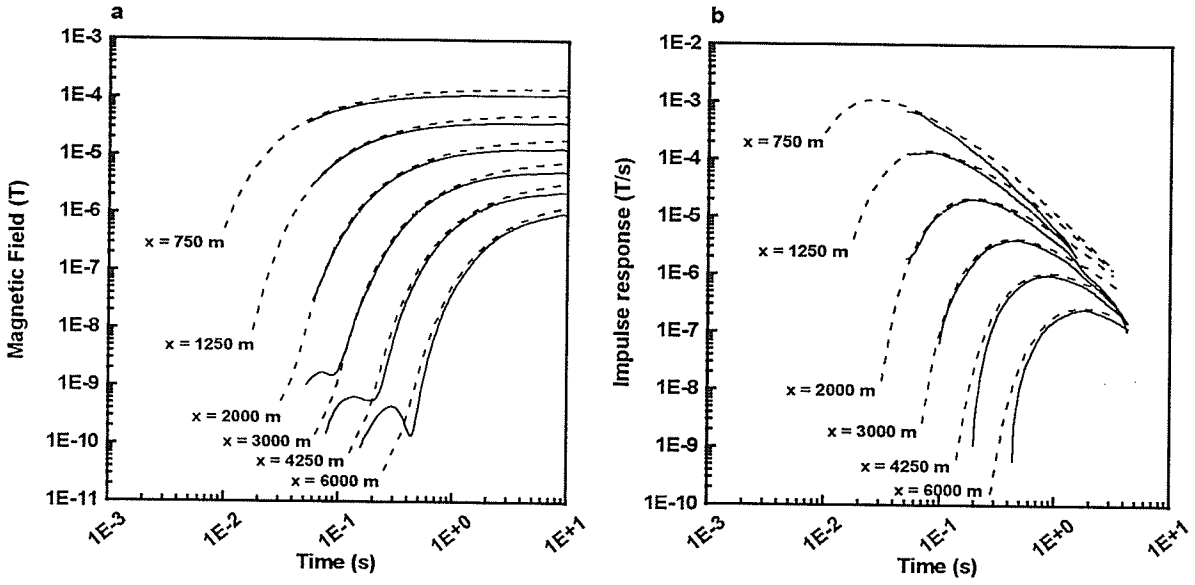

Figure 5.12 Comparison of the SA (dashed line) and FE solution (solid line) in the (y,t) domain for the DHS in figure 5.3a. The (a) magnetic field step response, and (b) magnetic field impulse response are plotted for several seafloor locations. The FE solution shows excellent agreement for values of $\dot{\mathbf{B}}_{max}$ in b.

that is required for modelling (*i.e.* often the results of a geophysical survey). The impulse-response may be obtained from the time derivative of $\mathbf{B}_y(t)$ and describes the time variations in the magnetic induction. To determine the impulse-response from the step-response in this thesis, I use a spline interpolation routine to first compute more finely spaced values of $\mathbf{B}_y$. The splining is done in the log time-domain. This process of interpolation provides more points on the step-response curve from which the time derivative can be numerically computed. Figure 5.13 demonstrates the fit of the spline interpolated data to the discrete points on the step-response curve.

5.6 Modelling on Different Computer Platforms

Although all of the modelling shown in this thesis was performed on a Fujitsu VPX240/10 vector computer in Calgary, Alberta, the FE program was initially tested

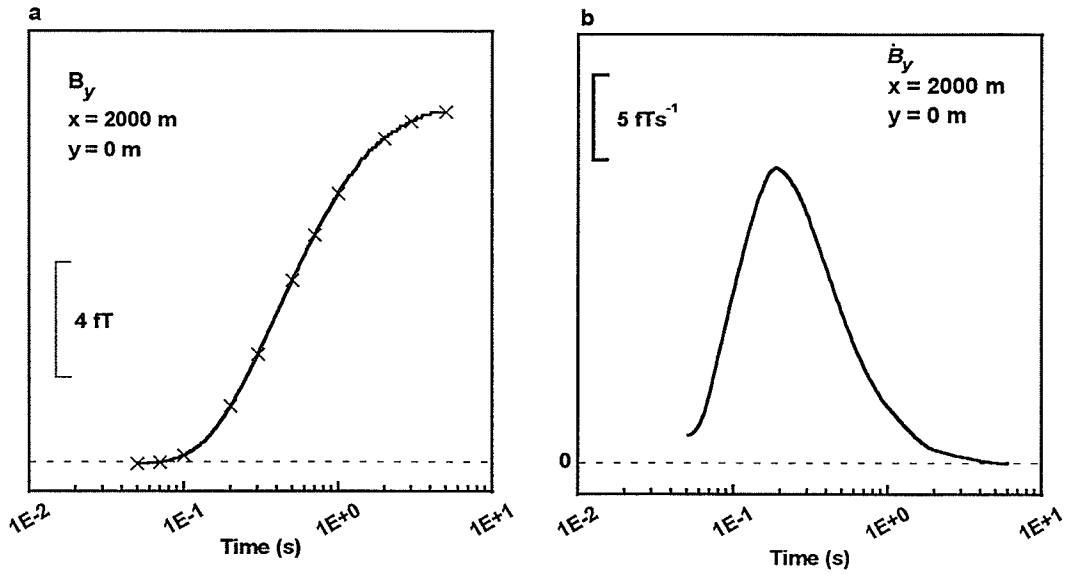

Figure 5.13 (a) Fit of spline (solid line) to the step response data. The spline interpolated data provides more points to use in the numerical time derivative. (b) The time derivative $\dot{B}_y(t)$ of the step response in (a).

on a Sparc IPX workstation. The reason for this is simple: workstations are common, inexpensive, and underutilized. If a workstation was capable of running such a program, the cost of modelling would decrease.

The Sparc IPX solves the EM fields for a single (q,s) (figure 5.5) in approximately 350 s, with a full space-time domain solution requiring approximately 20 cpu hours (Boyce & Ferguson, 1995). Calculating the fields for a single (q,s) value on the Fujitsu VPX requires only 8 s of cpu time. A full space-time solution takes $4\frac{1}{2}$-5 minutes with a vectorization rate of 45 percent.

When run on a Sparc workstation, the algorithm provided reasonably accurate solutions for simple double half-space models. Results become very inaccurate for more complex models containing thin layers or small blocks. The values calculated for the source fields and the inverse transforms are identical on both platforms, therefore, the problem is believed to arise in the accuracy available for the FE solution on the

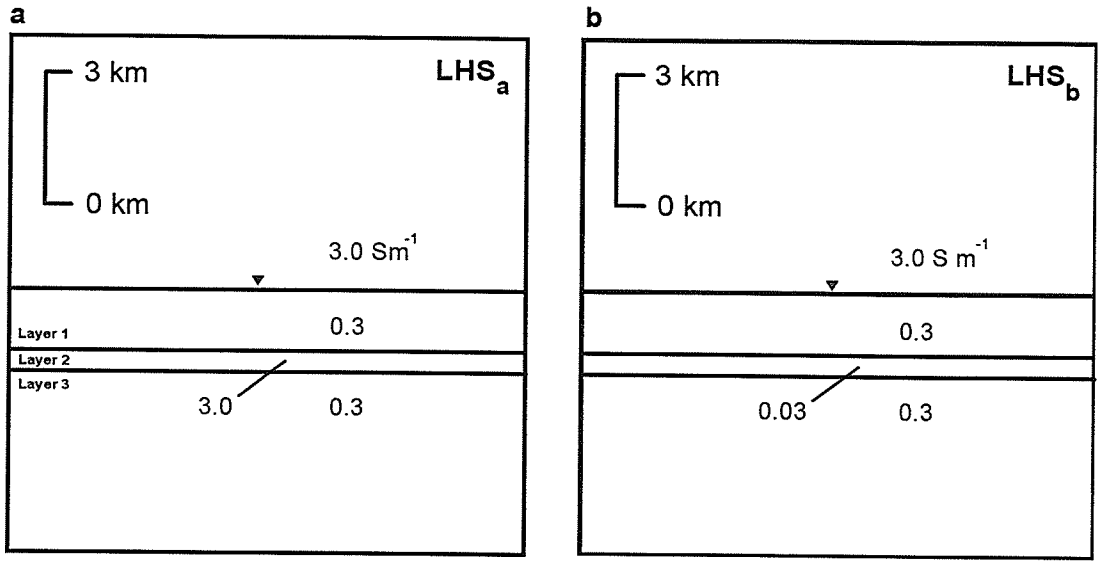

Figure 5.14 Layered half-space model with 3 seafloor layers. The (a) "conductive" and (b) "resistive" models discussed in §5.6 are identical except for the conductivity of layer 2 in the seafloor.

Sparc workstation (*i.e.* 32 bit precision). For this reason, any computations involving geologically reasonable models must be performed on a large computer such as the Fujitsu VPX240/10 with 64 bit precision.

5.7 Layered Half-Space Results

In this section, I examine the response of two similar layered half-space (LHS) models and compare the results to a semi-analytical solution. Although a layered half-space model is still only 1D (*i.e.* the conductivity is only a function of z), it provides a more complex model on which the FE program may be tested. Furthermore, studying the response of a complex 1D model is a logical step to make before trying to understand the response of a simple 2D model.

The two LHS models examined (figure 5.14) are identical geometrically, but have a different conductivity structure. Both models have three seafloor layers with conduc-

tivities σ_1=0.3 Sm^{-1} and σ_3=0.3 Sm^{-1} for layer 1 and layer 3. The conductivity of layer 2 is σ_2=3.0 Sm^{-1} in LHS_a and σ_2=0.03 Sm^{-1} in LHS_b. *i.e.* LHS_a contains a conductive layer 2 and LHS_b contains a resistive layer 2. Layer 2 is 500 m thick with the top of the layer located at 1.5 km depth.

Figures 5.15 and 5.16 show contours of the along-strike EM fields, $\mathbf{B}_y$ and $\mathbf{E}_y$, for LHS_a and LHS_b in three spatial dimensions and time. Figures 5.15a and 5.16a demonstrate that the presence of a conductive layer slows the diffusion of the magnetic field considerably, whereas the presence of a resistive layer enhances the rate of diffusion. Note that the magnetic field has largest magnitude at y=0 m, in-line with the source, and decays with distance y along-strike. The contour patterns for the electric field in figures 5.15b and 5.16b are of considerable interest. Figure 5.15b shows the electric field strength decreasing with depth from the source. At a depth of approximately 1000 m (in the relatively resistive layer 1), the field changes sign and begins to increase, reaching maximum strength again just inside the conductive layer 2. This "local" maximum in the electric field strength is due to electric currents induced in the conductor by the changing magnetic field. These currents are in the opposite direction to those in the HED source. Figure 5.16b shows a similar result, except that the "local" maximum in the electric field is found below the resistive layer 2 (in the conductive layer 3).

The magnetic impulse response for the DHS model and the two LHS models is shown in figure 5.17. These figures show that at locations close to the source, the diffusion time τ is approximately the same for all three models. However, there is a distinct difference in the values of τ for the three models at locations where the source-receiver separation is greater than the depth to the layer of anomalous conductivity in the LHS models. In particular, the signal in LHS_b (the resistive layer model) arrives much earlier than the signal from the other two models. The earlier arrival time indicates that

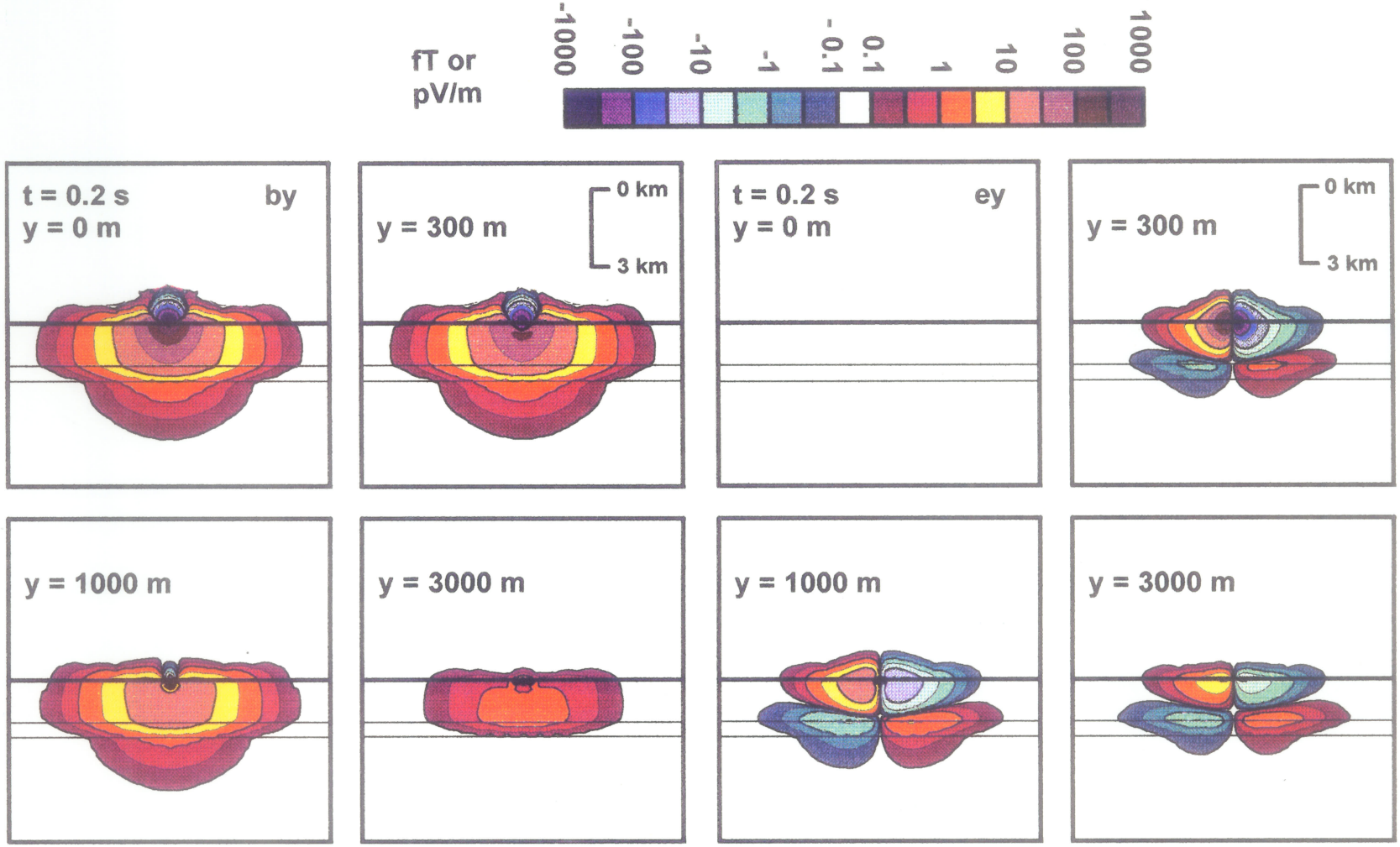

Figure 5.15 Contours of the step response for the (a) magnetic field and (b) electric field showing diffusion into a layered half-space containing a conductive layer 500 m thick at depth. The fields are shown at four distances, y, in the along-strike direction. The conductive layer slows the rate of diffusion of the magnetic field.

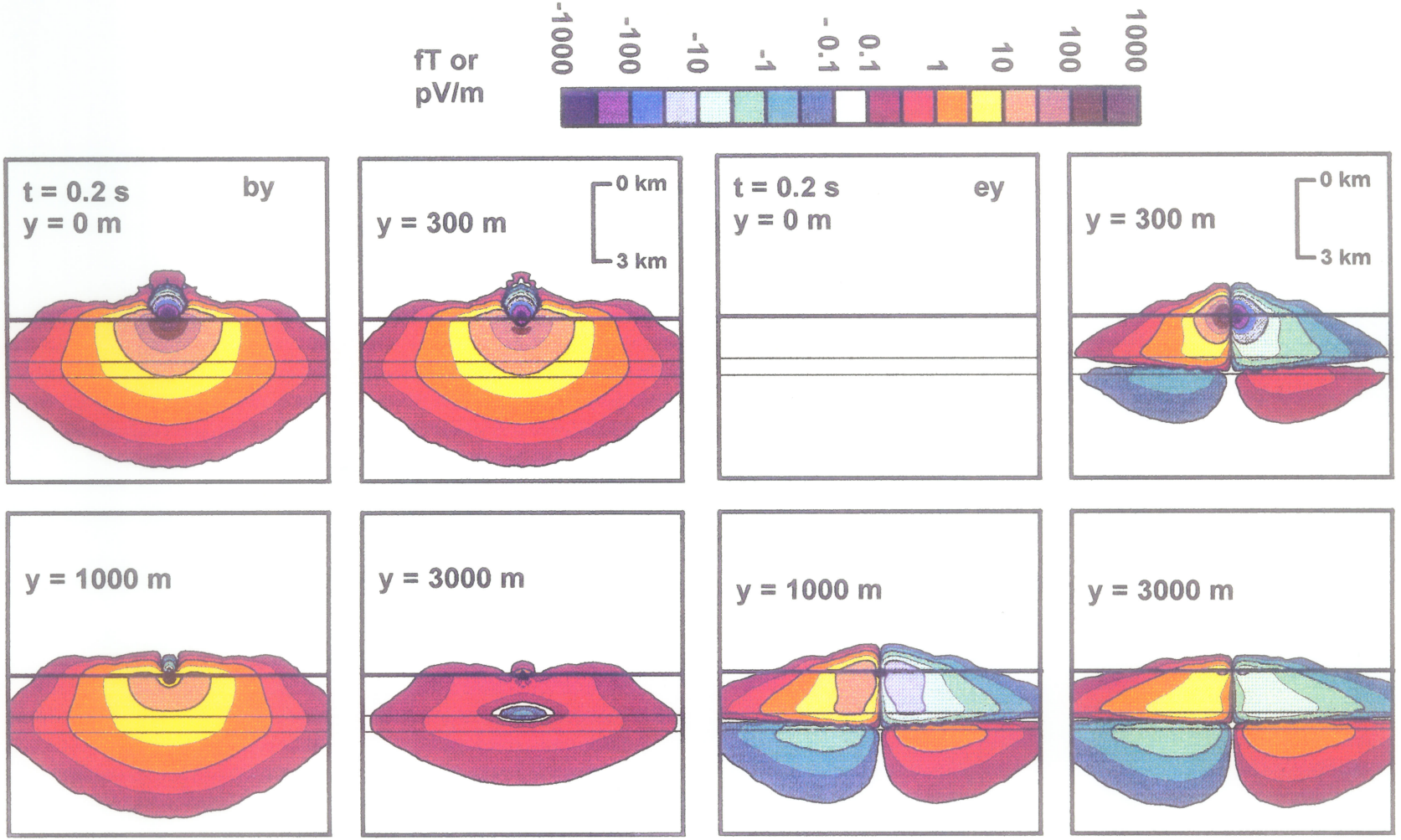

Figure 5.16 Contours of the step response for the (a) magnetic field and (b) electric field showing diffusion into a layered half-space containing a resistive layer 500 m thick at depth. The fields are shown at four distances, y, in the along-strike direction. The magnetic field diffuses faster through the resistive layer.

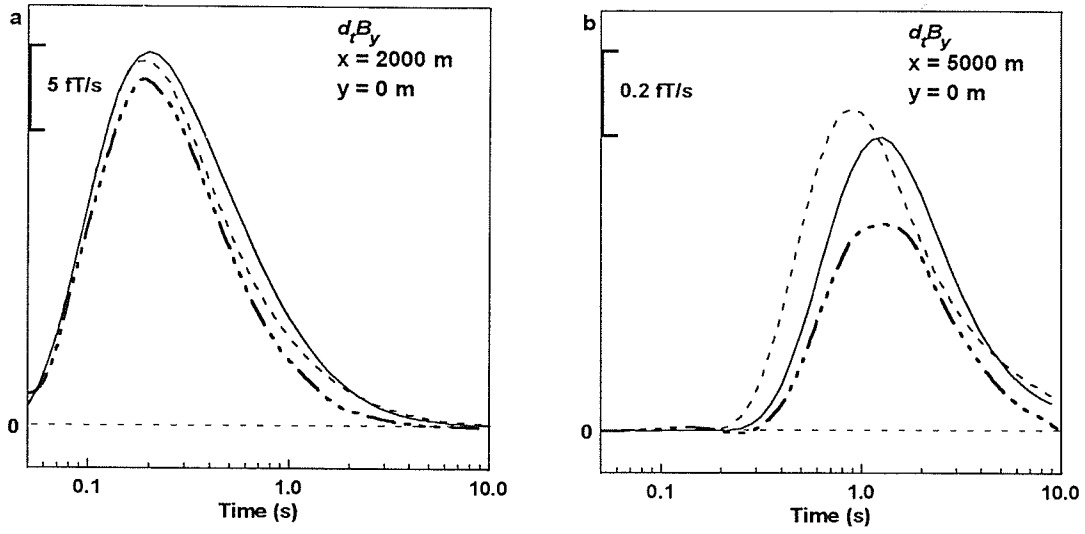

Figure 5.17 Impulse response curves at two seafloor locations comparing the response of the double half-space model from figure 5.3a and the layered half-space models from figure 5.14. At relatively large source-receiver separations, the signal from the "resistive" LHS_b model (dashed line) arrives much earlier than the signal from either the "conductive" LHS_a model (solid line) or the double half-space (dot-dash line).

the fields have a more resistive path to follow in LHS_b than in LHS_a or the DHS.

5.8 Data Display

Before presenting the modelling results for the 2D models, a description of the supplementary programs used in displaying the output from the FE program will be given. This "post-processing" was done entirely in a PC environment and included the use of both WINDOWS applications and many small FORTRAN programs I wrote.

The FE program outputs $\mathbf{B}_y(x, y, z, t)$ and $\mathbf{E}_y(x, y, z, t)$ at each node on the mesh. These datasets were input into SURFER for WINDOWS (Golden Software, 1993) to be gridded and contoured. The Kriging method of gridding in SURFER was used with a search radius of 1500 m. Grid lines were spaced approximately 200 m apart. This gridding method is slow, as the data output from the FE program is not random, or

evenly spaced, but has a spacing that grows logarithmically away from the origin. The gridded field values were then contoured and plotted (*e.g.* figure 5.5).

A program was written to extract the information used in the geophysical plots (*e.g.* figure 5.13) from the numerous datasets generated by the FE program. After extracting the data of interest, a cubic-spline interpolation was used to generate a more continuous set of field values (*e.g.* figure 5.12a) to be used in computing the time derivitive (*e.g.* figure 5.12b). These graphs and all other graphs like it in this thesis were displayed using GRAPHER for WINDOWS (Golden Software, 1993).

Chapter 6

Modelling of a Simple Seafloor Structure

6.1 Introduction

As a first stage in modelling, I examine the time-domain EM response of a simple seafloor structure. It is necessary to understand the response of simple structures in order to interpret the results from more complex, geologically-reasonable structures. In this chapter, a two-layered earth that has undergone faulting will be modelled. A set of three fault models including differences in both the depth to the fault and fault displacement will be used to determine the sensitivity of the CSEM response to changes in seafloor structure. Further rationale for studying the response of a simple faulted Earth comes from the fact that faults often provide a trapping mechanism for hydrocarbon accumulation (see chapter 2).

It is *not* the primary objective of the modelling in this chapter to determine if CSEM methods can detect the existence and dimensions of a fault structure, since seismic methods usually are capable of doing this with higher resolution. Instead, the focus of the modelling is to determine whether CSEM methods are capable of detecting a difference in conductivity across the fault when *a priori* information about the structure is available. To determine the relative sensitivity of CSEM responses to fault depth or displacement

would indicate the utility of the method for use in the exploration for hydrocarbons in this type of environment.

For simplicity, the fault in all three models is vertical. Although this is not a true representation of most hydrocarbon trapping faults (North, 1985), it is a reasonable first order approximation. The horizontal distance from the source to the fault will also remain constant from one model to the next. Although this thesis does not study the effects of changing the distances of the EM source from the structure of interest, the fact that most seafloor EM surveys deploy the source at more than one location should be kept in mind when studying the EM responses.

6.2 Faulted Models

The three models studied in this chapter are shown in figure 6.1. All three models have a two layer seafloor with conductivity σ_1= 0.1 Sm^{-1} and σ_2= 0.01 Sm^{-1} for the upper and lower layers respectively. The conductivity of the seawater is σ_0=3.0 Sm^{-1}. Assuming that the North direction is into the page, the HED source is located 2500 m west of the fault. Model F_1 has a fault displacement of 1500 m and a depth to the fault of 1000 m. In model F_2, the depth to the fault is only 500 m, and the displacement is 2000 m. Model F_3 has the same depth to fault as F_2, but only 1000 m displacement. These three models represent both a change in the depth to the fault (F_1/F_2), and a change in the fault displacement (F_2/F_3). Although the fault offsets described above are very large, these models provide a logical next step from the 1D models in chapter 5.

Figure 6.1d is the FE mesh generated for model F_1; the meshes for models F_2 and F_3 are similar to the one shown. These meshes are very similar in structure and size to the DHS mesh in chapter 5. The mesh in figure 6.1 contains N=1268 nodes and 2472 triangular elements.

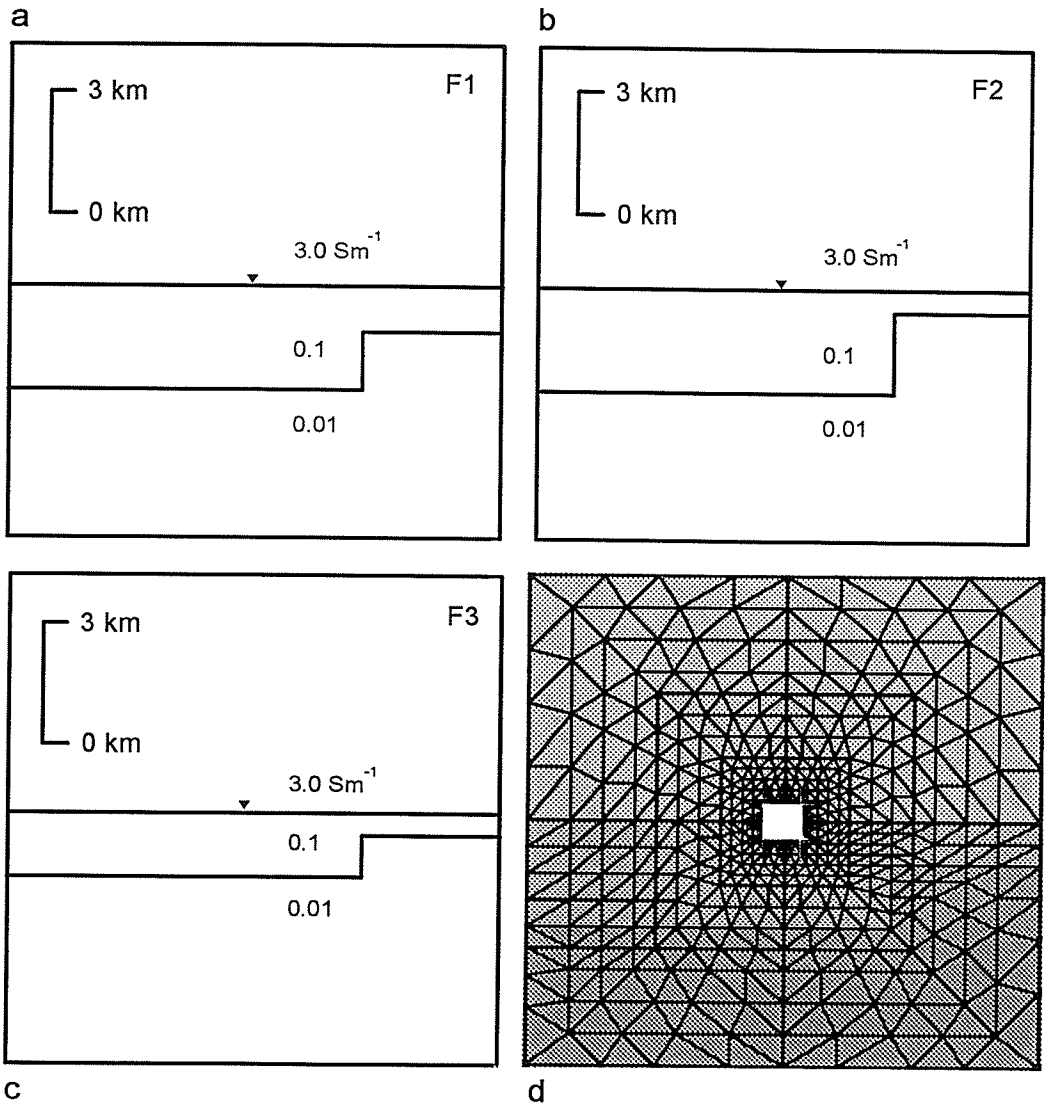

Figure 6.1 The three fault models showing variation in both the depth to the fault and fault displacement. (a) F_1 depth=1000 m, displacement=1500 m; (b) F_2 depth=500 m, displacement=2000 m; (c) F_3 depth=500 m, displacement=1000 m; (d) FE mesh generated for model in (a).

Figures 6.2-6.4 show contours of the along-strike magnetic $\mathbf{B}_y(t)$ and electric $\mathbf{E}_y(t)$ fields from model F_1 for a range of times 0.2 s $\leq t \leq$ 1.0 s after step-on of the x-directed HED. Each figure shows the fields for a range of distances 0 km $\leq y \leq$ 3 km in the along-strike direction. These plots illustrate, in three spatial dimensions and time, the patterns of electromagnetic diffusion through the two dimensional fault structure. Recall from §5.5, that very small fields are not shown on the contour plots (i.e. the fields outside the last contour are not zero). The field contours for models F_2 and F_3 are not sufficiently different from figures 6.2-6.4 to warrant their display. Figures 6.2b-6.4b show that the fault has a significant effect on the diffusion of the electric field. The field diffuses more rapidly towards the faulted side than the non-faulted side. This is because a faster diffusion path is provided by the up-faulted resistive block. This effect increases with increasing distance along-strike (increasing y). In contrast, the fault has a small effect on the magnetic field patterns: the contours are nearly symmetrical about x=0 m. Notice that the magnetic field is strongest at y=0 m, in-line with the transmitter, and decays with distance y along-strike. This is expected from the contour plots of the fields in the x-y plane shown in figure 2.5.

6.3 Geophysical Responses

To study the geophysical response, the fields $\mathbf{B}_y(x, y, 0, t)$ and $\mathbf{E}_y(x, y \neq 0, 0, t)$ must be extracted from the data set and plotted. Figure 6.5 shows how the magnetic step-response for model F_1 varies in time for several seafloor locations. To determine if a faulted two-layered earth provides a significantly different response than a non-faulted two-layer earth, the impulse-response for model F_1 is plotted against the FE response for two different layered half-spaces (shown in figure 6.6). The two layered half-spaces are denoted LHS_1 and LHS_2. Note that the conductivities of the two layers in LHS_1 and

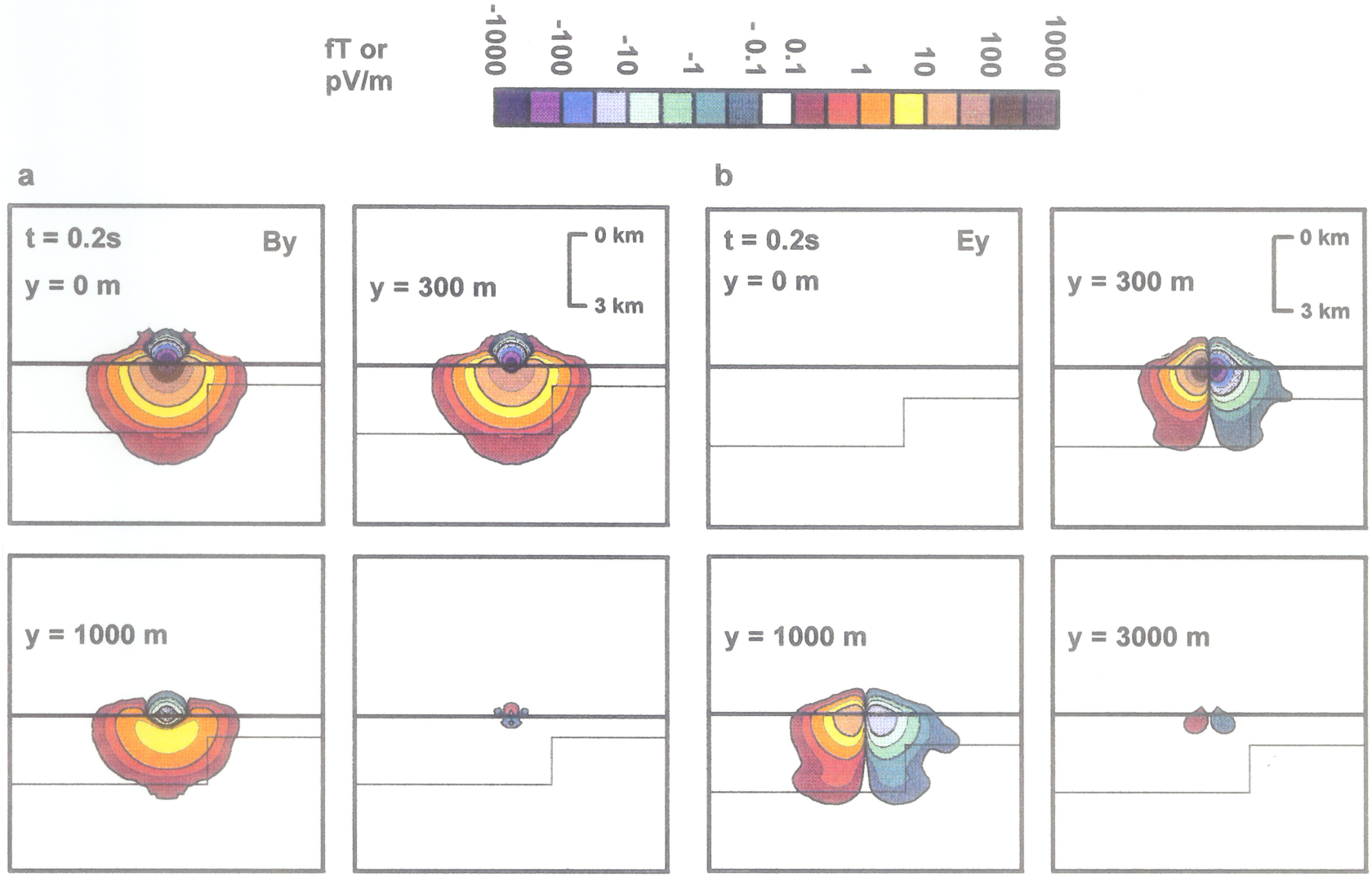

Figure 6.2 Contours of the (a) magnetic field and (b) electric field in three spatial dimensions showing diffusion into the faulted earth (model F_1) at time t=0.2 s after activation of the source. (σ_0=3.0 Sm^{-1}, σ_1=0.1 Sm^{-1}, σ_2= 0.01 Sm^{-1}).

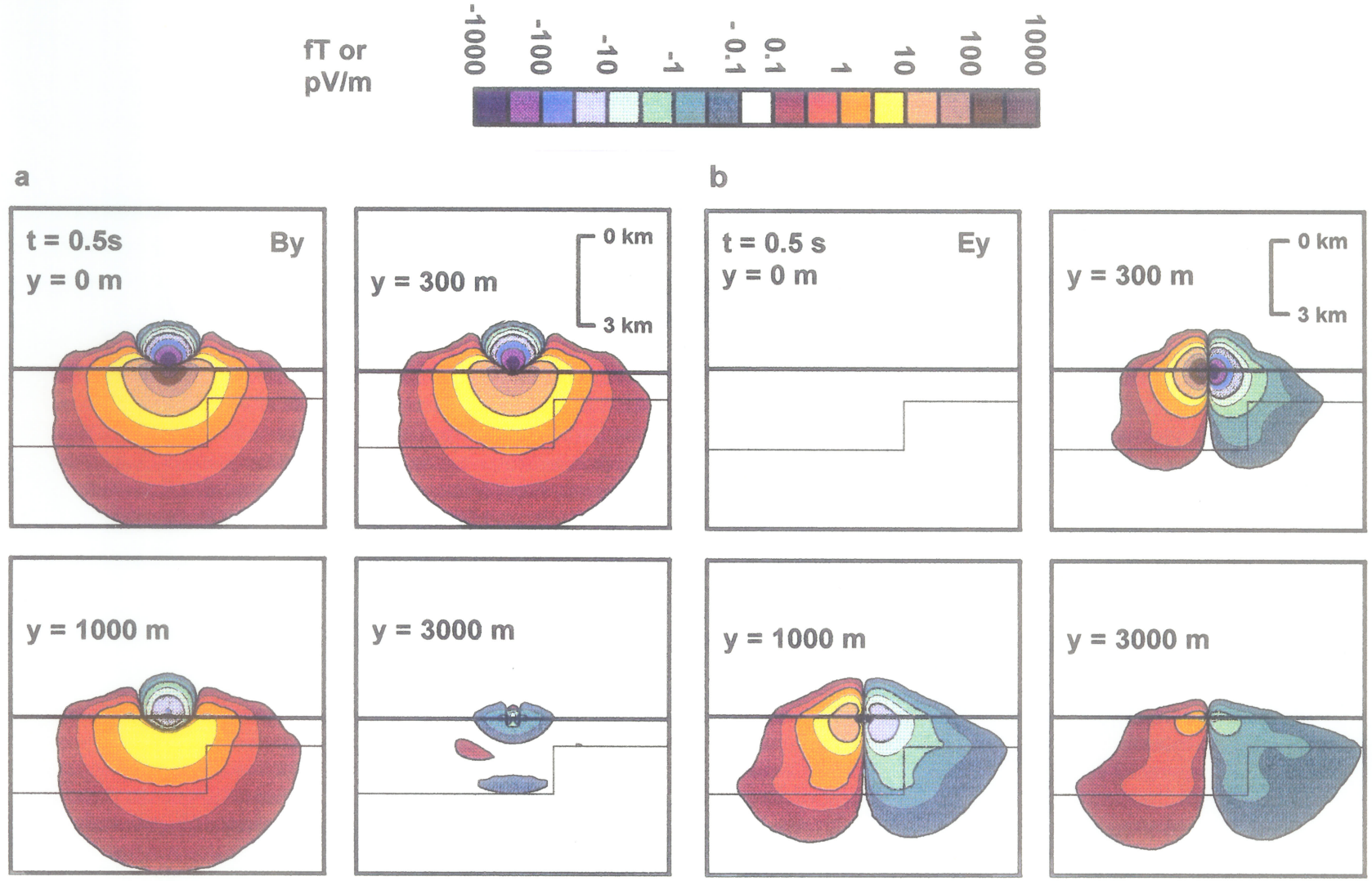

Figure 6.3 Contours of the (a) magnetic field and (b) electric field in three spatial dimensions showing diffusion into the faulted earth (model F_1) at time t=0.5 s after activation of the source. (σ_0=3.0 Sm^{-1}, σ_1=0.1 Sm^{-1}, σ_2= 0.01 Sm^{-1}).

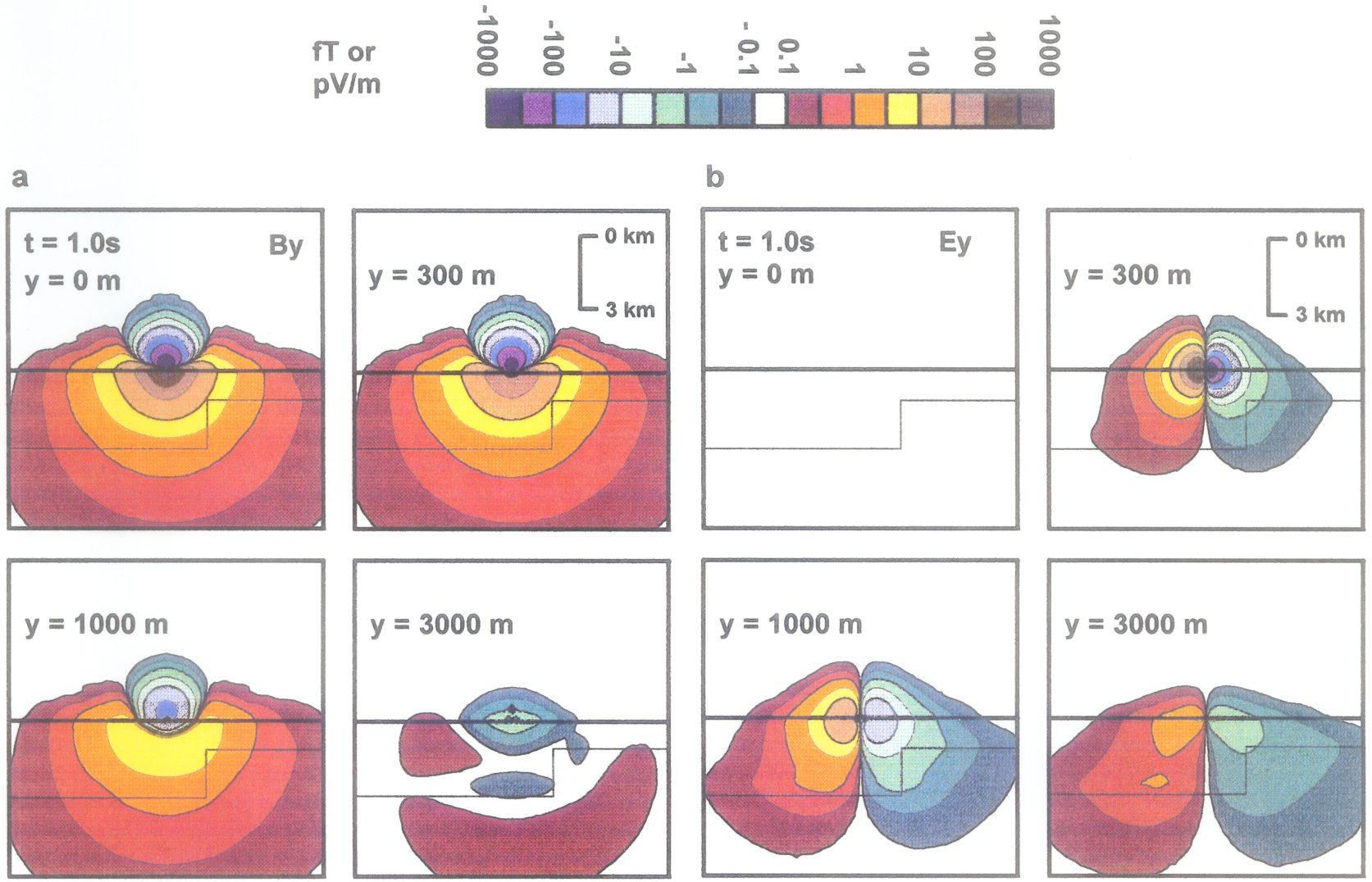

Figure 6.4 Contours of the (a) magnetic field and (b) electric field in three spatial dimensions showing diffusion into the faulted earth (model F_1) at time t=1.0 s after activation of the source. (σ_0=3.0 Sm^{-1}, σ_1=0.1 Sm^{-1}, σ_2= 0.01 Sm^{-1}).

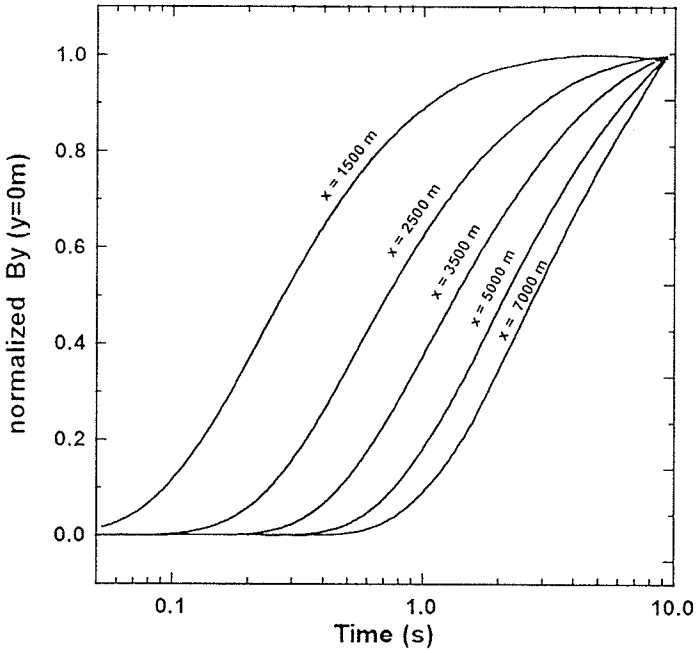

Figure 6.5 Magnetic step response for five seafloor receiver locations. The response is normalized by dividing by the late time response.

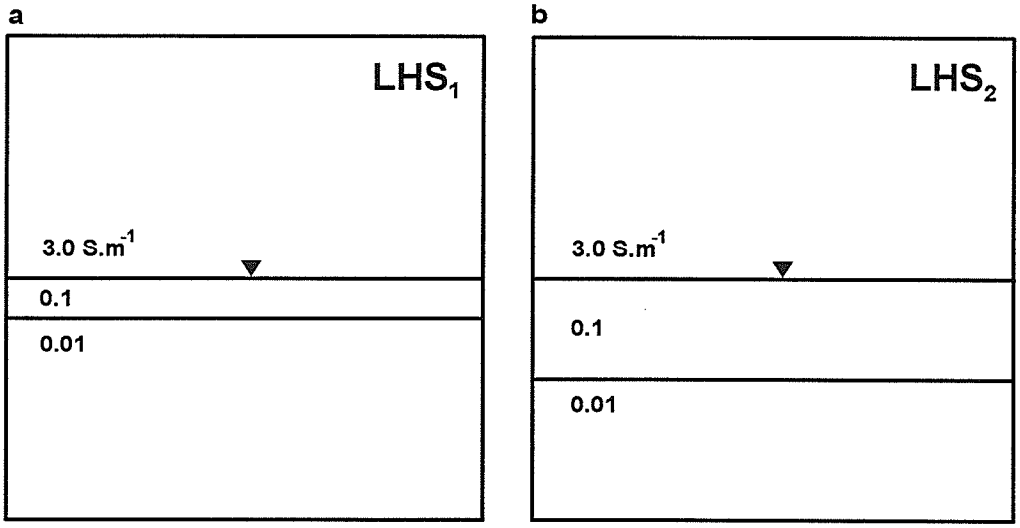

Figure 6.6 Two non-faulted layered earth models, (a) LHS_1 and (b) LHS_2 used to compare with the response of the faulted earth models in figure 6.1. (σ_0=3.0 Sm^{-1}, σ_1=0.1 Sm^{-1}, σ_2= 0.01 Sm^{-1}).

LHS_2 are the same as in the faulted models, corresponding to the structures to the east and west of the fault.

Figures 6.7-6.9 show $\dot{\mathbf{B}}_y$ (y=0 m), $\dot{\mathbf{B}}_y$ (y=1000 m), and $\dot{\mathbf{E}}_y$ (y=1000 m) for each of the three models, F_1, LHS_1, and LHS_2. The first point to note is that the shape of the curves for $\dot{\mathbf{B}}_y$ (y=0 m) and $\dot{\mathbf{B}}_y$ (y=1000 m) are almost identical. This shows that a survey can be performed with a line of receivers at an azimuth other than 0°. However, receiver locations should be as close to "in-line" as possible if both magnitude and arrival times are desired. It is also very important that the azimuth of the individual receivers be accurately known.

Although there is a relatively large difference in the amplitude of the impulse response between F_1 and LHS_1, there is virtually no difference when comparing F_1 with LHS_2. However, when the arrival time (τ) is examined, some differences become evident.

For examining the spatial relationship of the arrival time τ for each model, I use a method similar to the "refraction" method of Ferguson & Edwards (1994). For several seafloor locations, the square root of arrival time (τ) is plotted against distance from the source for both the magnetic and electric impulse-responses (figure 6.10). Doing this, the plotted arrival time curve for a half-space is a straight line with slope proportional to its conductivity. Plotting the arrival time this way is analogous to seismic arrival time versus distance curves (Ferguson & Edwards, 1994).

The arrival time curve for the F_1 magnetic field (figure 6.10a) is almost identical to the curve for LHS_2 within the first 4000 m of the source. Past 4000 m, the slope of the F_1 curve decreases, indicating a more resistive primary diffusion path (*i.e.* past 4000 m, the path of the diffusing magnetic field includes the up-faulted resistive layer 2). Although the shape of the F_1 curve is similar to that of the LHS_1 curve, multiple transmitter

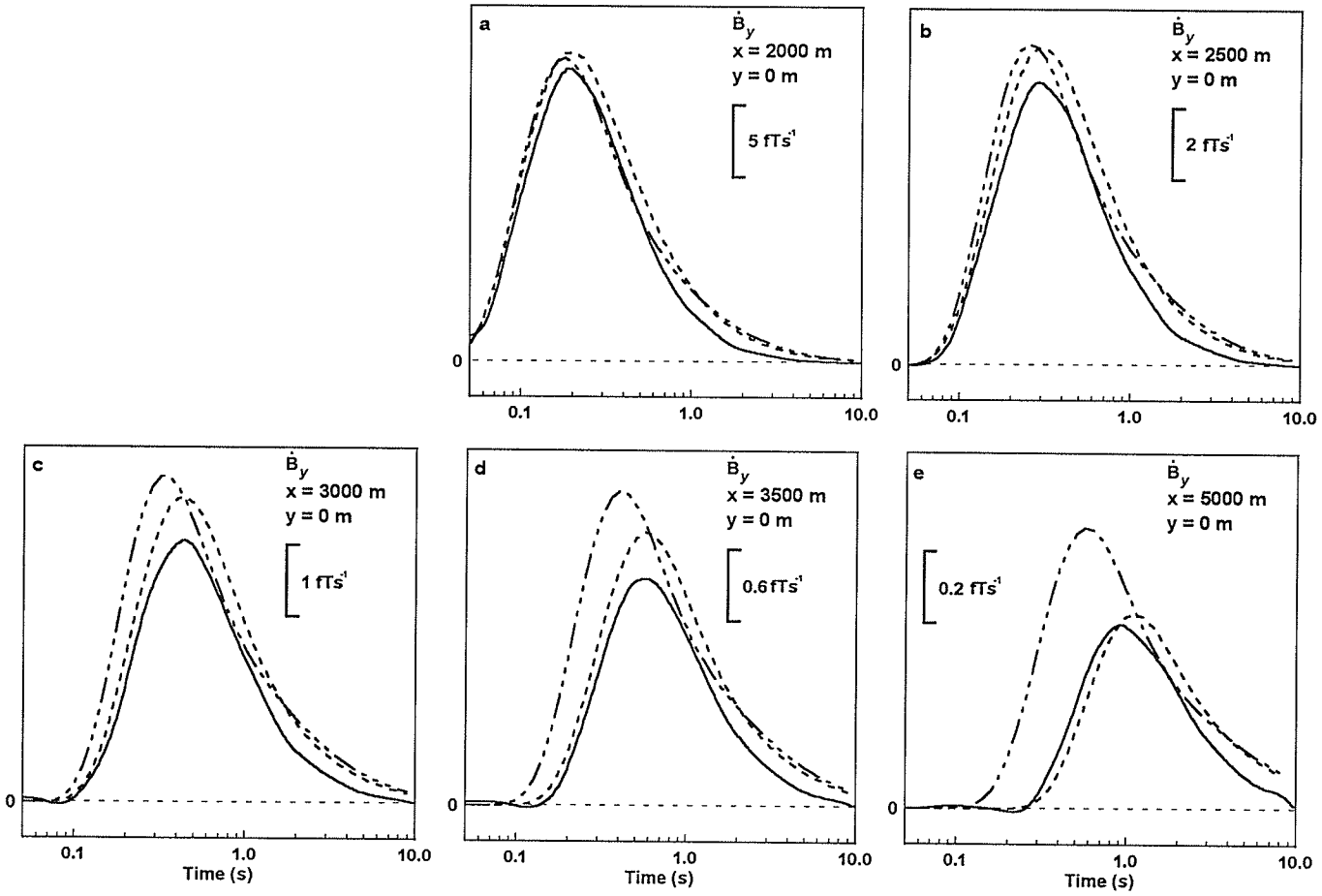

Figure 6.7 Magnetic impulse-response for fault model F_1 (solid) and the layered earth models LHS_1 (short dashes) and LHS_2 (long, short dashes) for y=0 m along-strike. There is very little difference in amplitude between F_1 and LHS_2 indicating that the amplitude of the response is not affected by the presence of the fault.

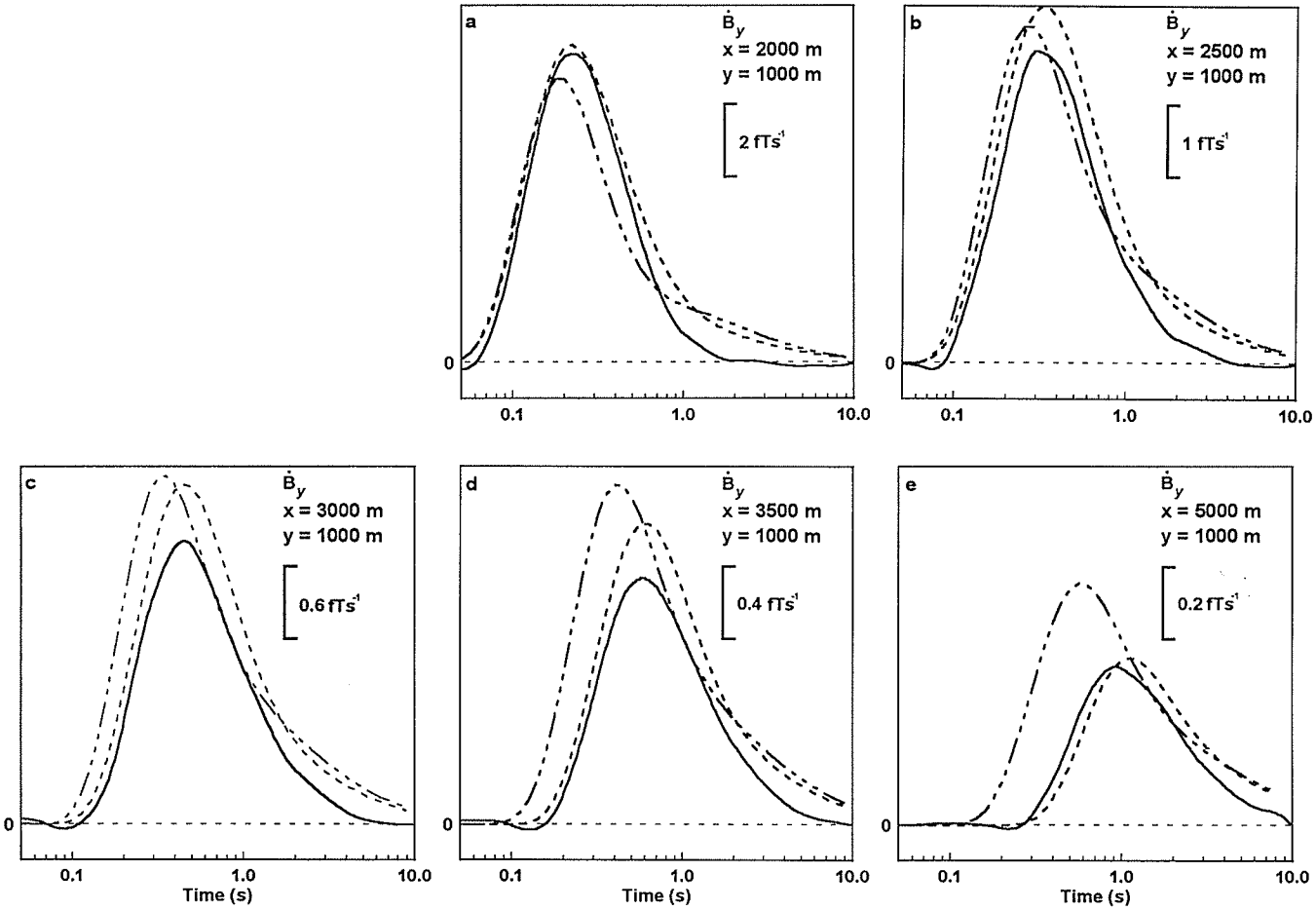

Figure 6.8 Magnetic impulse-response for fault model F_1 (solid) and the layered earth models LHS_1 (short dashes) and LHS_2 (long, short dashes) for y=1000 m along-strike. This response curve is very similar to that for y=0 m, suggesting that exact placement of the receiver in the along-strike direction is not critical.

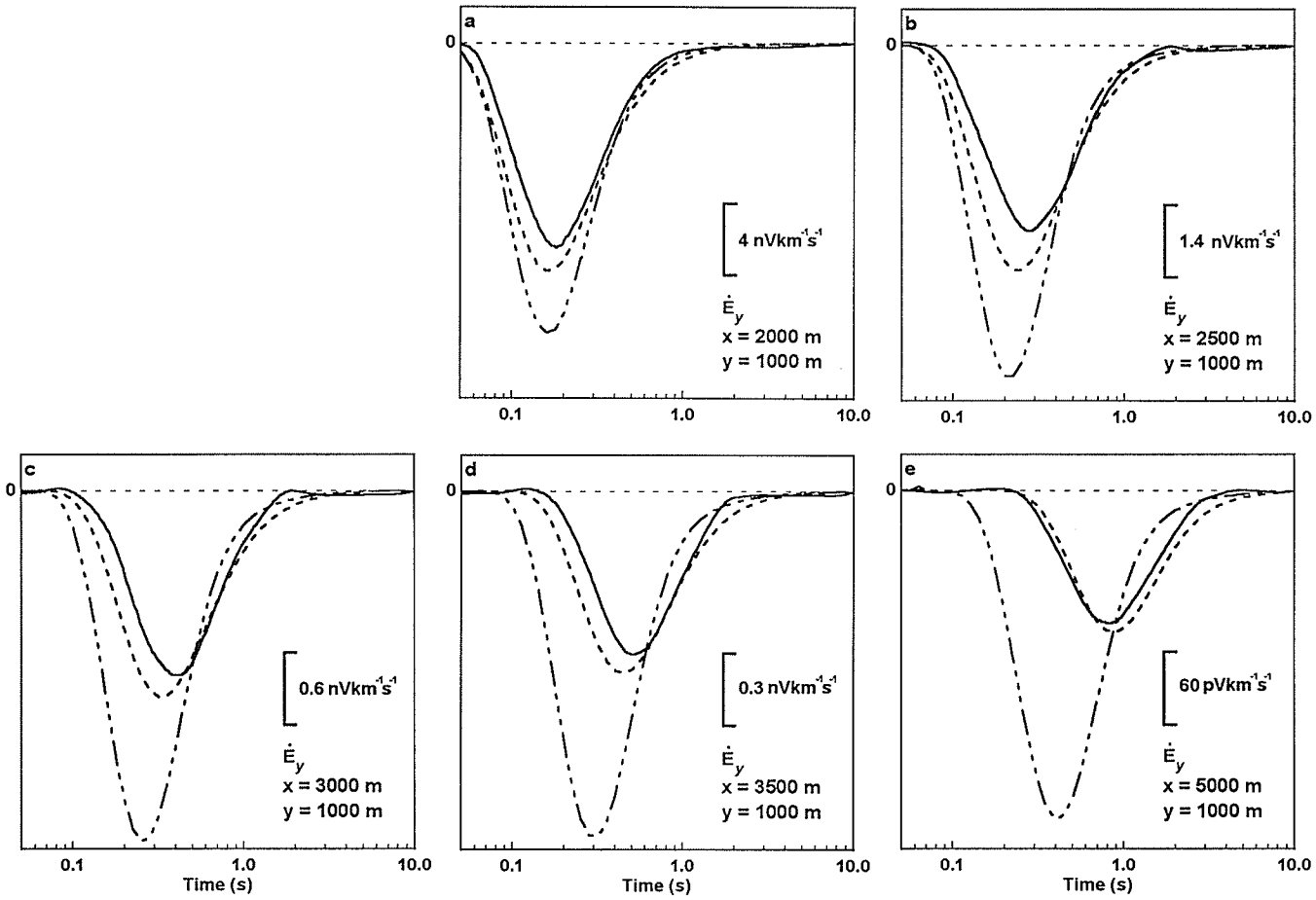

Figure 6.9 Electric impulse-response for fault model F_1 (solid) and the layered earth models LHS_1 (short dashes) and LHS_2 (long, short dashes) for y=1000 m along-strike. Similar to the magnetic impulse response, there is very little difference in amplitude between F_1 and LHS_2 indicating that the amplitude of the response is not affected by the presence of the fault.

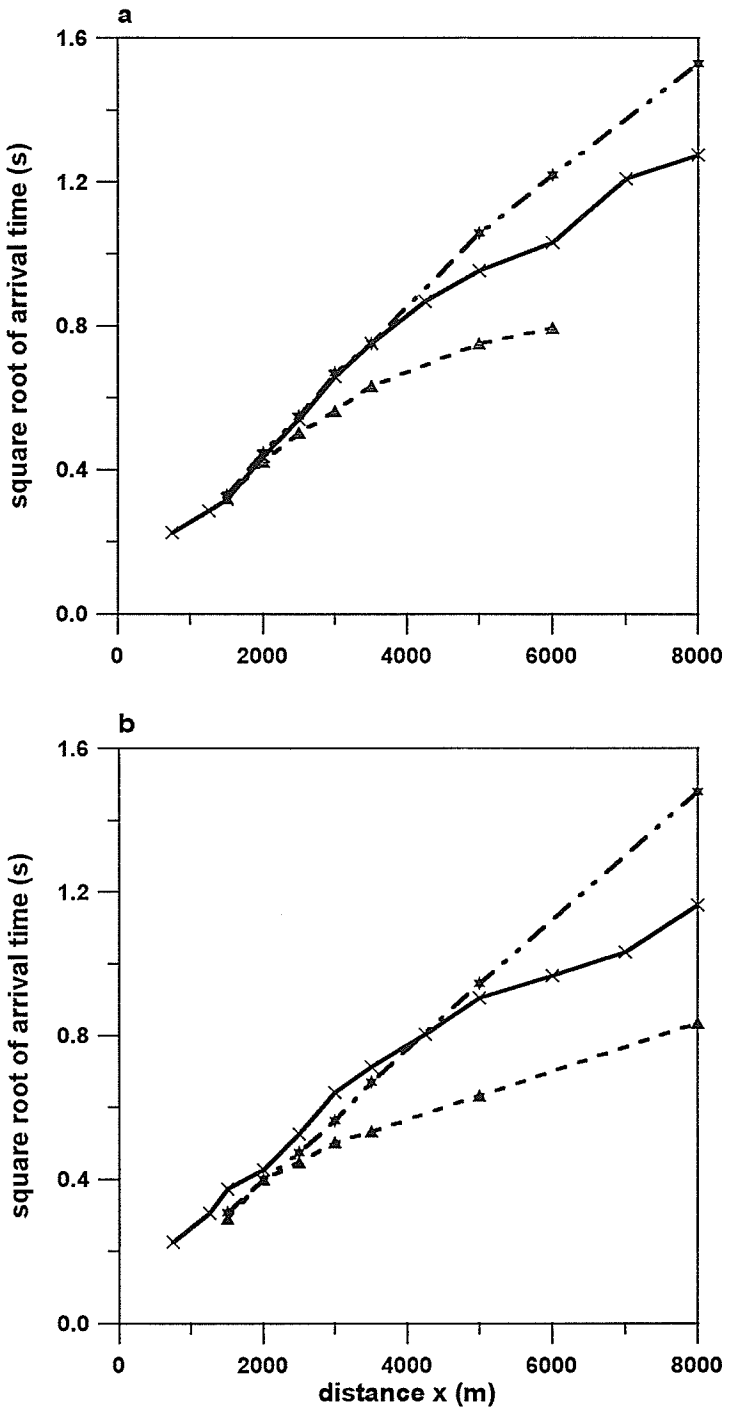

Figure 6.10 Square root of arrival time τ plotted against distance x from the source. (a) τ_{B} at y=0 m and (b) τ_{E} at y=1000 m, for fault model F_1 (solid) and the layered earth models LHS_1 (short dashes) and LHS_2 (long, short dashes) These plots are for y=0 m along-strike. The change in slope of the F_1 curve at $x \simeq$4000 m indicates a more resistive diffusion path than for LHS_2.

positions and extra receivers to the left of the transmitter would allow discrimination between the two cases in a real geophysical survey.

The arrival time curve for the F_1 electric field (figure 6.10b) shows a distinctly different shape from the LHS curves. Although the F_1 and LHS_2 curves have the same slope for the first 4000 m, indicating diffusion paths with similar conductivities, the F_1 curve demonstrates a slightly later arrival time. The reason for this time lag in the F_1 response is not clear, but it may be due to a build-up of electric charge on the fault surface. Although this affect appears to be due to the presence of the fault, it could easily be interpreted as a more conductive layer of a LHS. Again, multiple transmitter location would help discriminate. Past 4000 m, the slope of F_1 decreases just as in figure 6.10a, again indicating a more resistive diffusion path. The F_1 curve in figure 6.10b is not as easily mistaken for a simple unfaulted earth model, providing further evidence that the electric field is more sensitive to the presence of the fault structure than the magnetic field.

To develop an idea of the sensitivity of the method to fault depth and displacement, the magnetic and electric impulse responses are compared for F_1, F_2, and F_3 (figures 6.11-6.13). As was the case for the earlier comparison, the amplitude of the response does not change appreciably from model to model. These plots show that by decreasing the depth to the fault from 1000 m (F_1) to 500 m (F_2), the arrival time of the signal decreases for receiver locations past the fault. This indicates a more resistive diffusion path. These plots also show that decreasing the fault displacement from 2000 m (F_2) to 1000 m (F_3) decreases the arrival time. This is most likely because the most resistive diffusion path for receivers above or beyond the fault, is then through the lower layer.

Figure 6.14 shows the arrival times of both the magnetic and electric impulse-responses for all three fault models and both layered half-spaces from figure 6.6. The

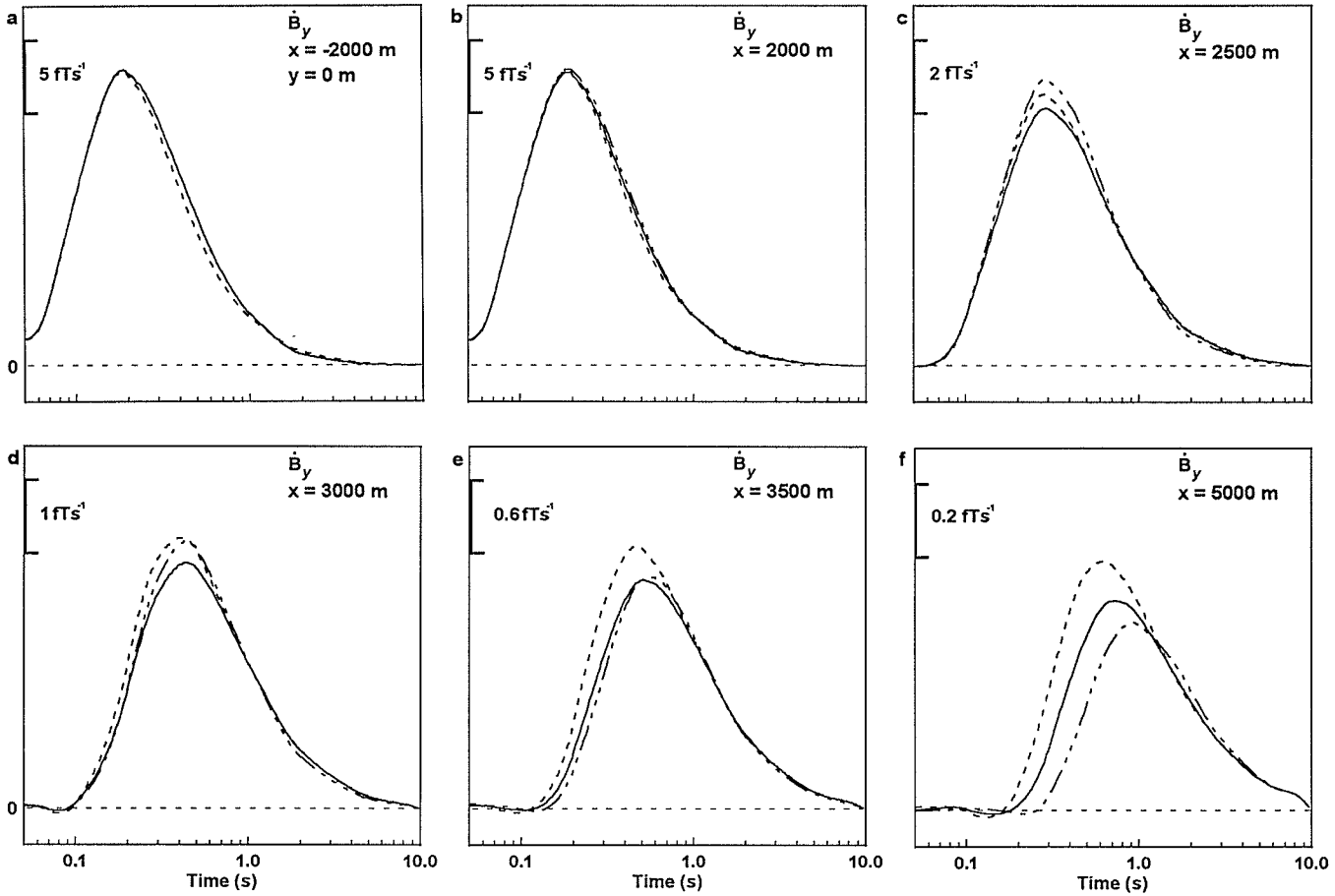

Figure 6.11 Magnetic-impulse response comparing fault models F_1 (short, long dashed), F_2 (solid), and F_3 (short dashed) for y=0 m along-strike. There is very little difference in amplitude between the three models indicating that the amplitude of the response is not affected greatly by the depth to the fault or the fault displacement.

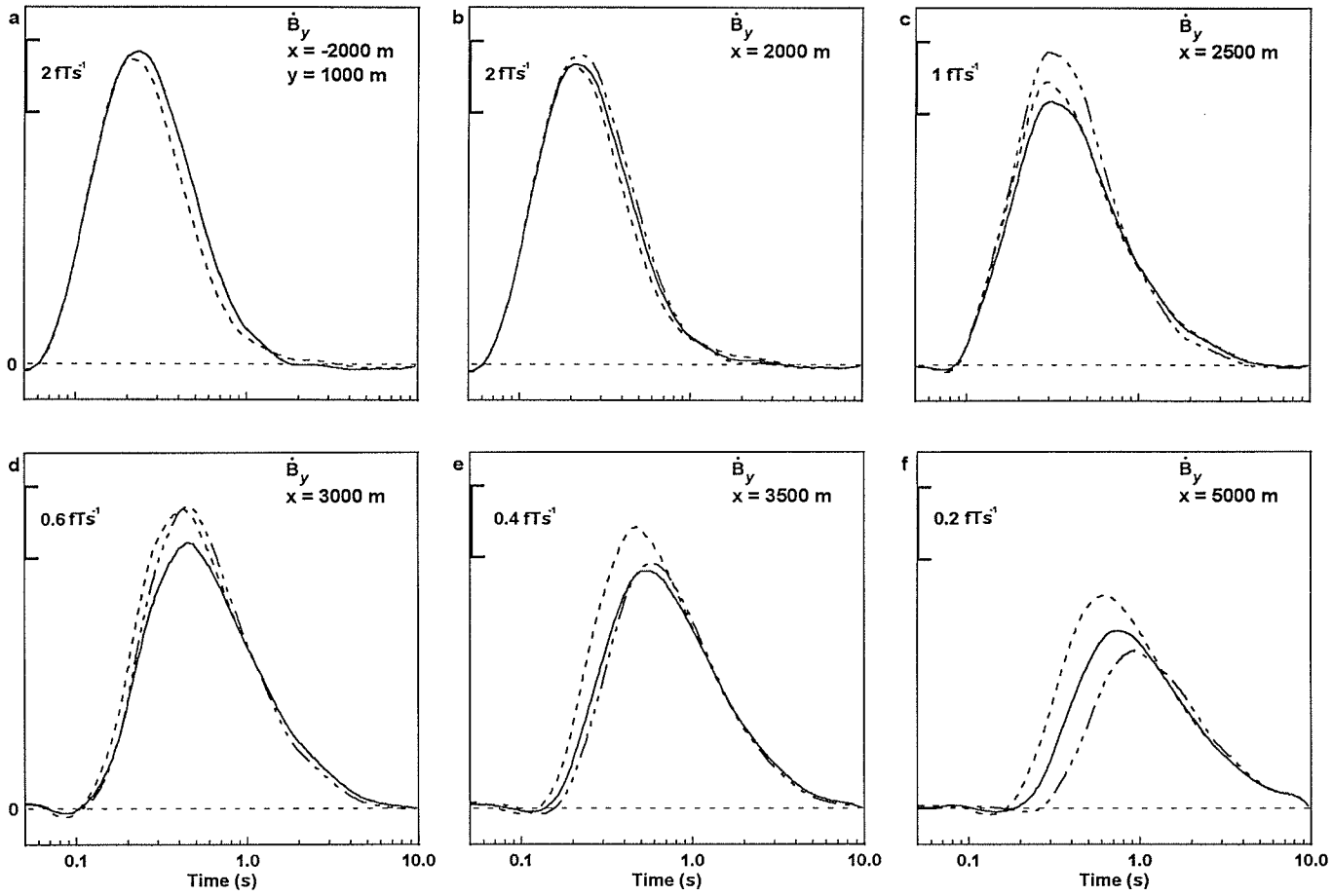

Figure 6.12 Magnetic-impulse response comparing fault models F_1 (short, long dashed), F_2 (solid), and F_3 (short dashed) for y=1000 m along-strike. This response curve is very similar to that for y=0 m, suggesting that exact placement of the receiver in the along-strike direction is not critical.

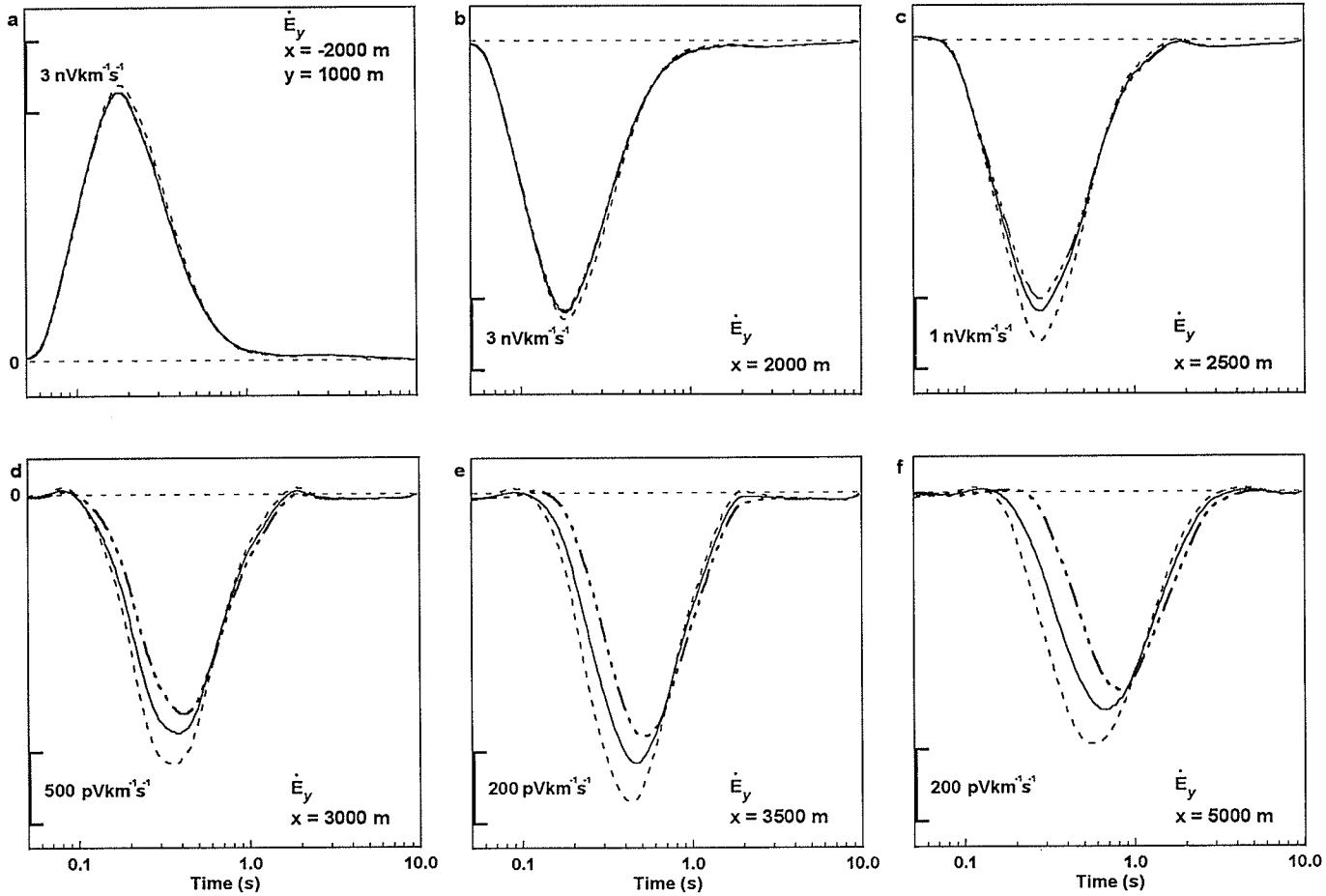

Figure 6.13 Electric impulse-response comparing fault models F_1 (short, long dashed), F_2 (solid), and F_3 (short dashed) for y=1000 m along-strike. Similar to the magnetic impulse response, there is very little difference in amplitude between the three models indicating that the amplitude of the electric response is not affected by the depth to the fault or the fault displacement.

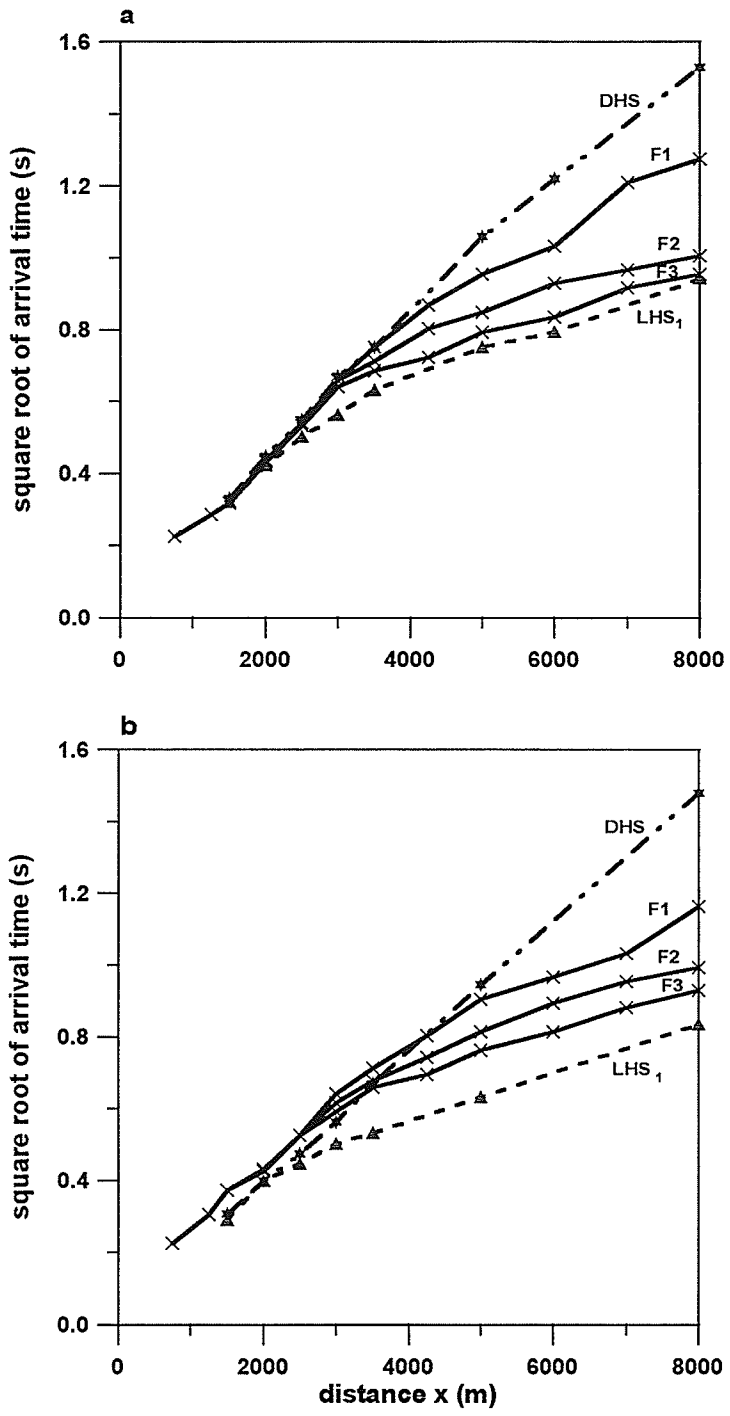

Figure 6.14 Square root of arrival time τ plotted against distance x from the source. (a) τ_B at y=0 m and (b) τ_E at y=1000 m, for fault models F_1, F_2, and F_3. These plots are for y=0 m along-strike. The decrease in slope of the F_2 and F_3 curves at $x \simeq$4000 m indicates that the CSEM method *is* sensitive to both fault depth and fault displacement. The curves for the DHS (long, short dashes) and LHS_1(short dashes) are plotted for reference.

arrival time curves for all three fault models are identical within the first 2500-3000 m from the source. The curves for F_2 and F_3 undergo a sharp decrease in slope at 3000 m, indicating that the diffusion path for these models is significantly more resistive than that of F_1 past this point. Although the F_2 and F_3 curves have the same slope past 4000 m, the F_3 signal has an earlier arrival time.

The results presented in figure 6.14 suggest that the CSEM method is sensitive to both the depth of the fault and to the displacement on the fault. However, the differences in the arrival time curves between the three fault models and the two unfaulted models are small. Based on the information from one source location alone, it may not be possible to determine whether there is a conductivity discontinuity associated with the fault or if the conductivity structure is continuous across the fault. Therefore, in a real seafloor EM survey, measurements would need to be collected for several source points located on both side of the fault. Further numerical modelling to study the response at different source locations would give an improved sense of the sensitivity of CSEM methods to a faulted environment.

As stated earlier in this chapter, seismics can usually locate a fault more accurately than the EM method being studied. However, in cases where seismics fails, or where information about the conductivity structure of an existing fault is desired, the CSEM method has been shown to be useful.

6.4 Implications for More Complex Modelling

Figures 6.8-6.10 show that the CSEM method is sensitive to a conductivity discontinuity associated with a fault, and figures 6.11-6.14 show that the method is sensitive to both the fault depth and displacement. However, the models used in this comparison all have large vertical displacements (between 1000 m and 2000 m) of the conductivity

structure at the fault. Furthermore, the structural *differences* between the models are not small. Thus, it can be implied that the CSEM method may not be sensitive to relatively small changes in structure, especially at depths greater than about 2000 m. The responses from figures 6.11-6.14 suggest that the sensitivity to relatively small structural change is greatest near the surface. Therefore, any modelling of more complex earth structures should restrict the depth of investigation to 1000 to 2000 m.

Chapter 7

Complex Layered Earth Models: A Stratigraphic Example

7.1 Introduction

An important class of problems in EM exploration for hydrocarbons is the measurement of the variations in electric conductivity within a stratigraphic horizon (see chapter 3). Such variations often represent changes from low-porosity sediments that are electrically resistive to zones of high porosity filled with conductive saline waters. Usually, the distinction between structural and stratigraphic is not clear, and in most cases models must contain both structural and stratigraphic elements. In this chapter, a combination structural/stratigraphic model is employed to determine the sensitivity of CSEM to conductivity changes within a single layer of the model. This type of model requires *a priori* information (*e.g.* seismics) of the structural details of the model, but a lack of knowledge about the porosity variations within individual layers of the model.

The prime motivation for this type of model is to provide variable diffusion paths from the source to receivers to study the interaction of the fields with complex structures.

7.2 A Complex Structural/Stratigraphic Model

The model used in this chapter is shown in figure 7.1. Structurally, the model contains four layers with the third layer having been displaced by a set of step faults:

the displacement on each fault is 500 m. The first and third layers are 250 m thick, and the second layer is 1500 m thick to the left of the source and 500 m thick to the far right. The source is located 3000 m to the left of the first fault. Two slight variations of this model are compared to determine if CSEM is capable of detecting a conductivity change in one part of the model. The shaded region of layer three in figure 7.1 is the part of the model that varies. For model S_1, the conductivity of the shaded region is the same as the rest of layer three, and for model S_2, the conductivity is reduced by an order of magnitude to equal that of layer 2.

The FE mesh in figure 7.1b is very large compared to the meshes generated for the fault models in chapter 6. This is caused by the relatively thin layers being represented. To keep the aspect ratios of the triangular elements below 5:1, the node density must be increased in and around the thin layers. The mesh for the models in figure 7.1 contains N=2238 nodes and 4424 triangular elements. This is in comparison to N=1268 for the models in chapter 6. The solution time for the magnetic and electric fields at one time on the Fujitsu VPX240/10 is approximately 10.5 cpu minutes with 55% vectorization being attained.

Figures 7.2 and 7.3 show contours of the along-strike magnetic and electric fields at t=0.5 s and y=300 m comparing models S_1 and S_2. Notice on the far left of figure 7.2a, the diffusion of the magnetic field is slowed considerably through the conductive layer three. This effect is not as noticeable to the right of the source presumably because the conductive layer has been displaced upwards 500 m, thus opening up a more resistive path for the fields to follow. Reducing the conductivity of the up-faulted portion of layer three in figure 7.2b appears to have virtually no affect on the diffusing magnetic field.

The electric field is affected by this change to a slightly greater degree than the magnetic field. First, notice that to the left of the source in figure 7.3a, the electric field

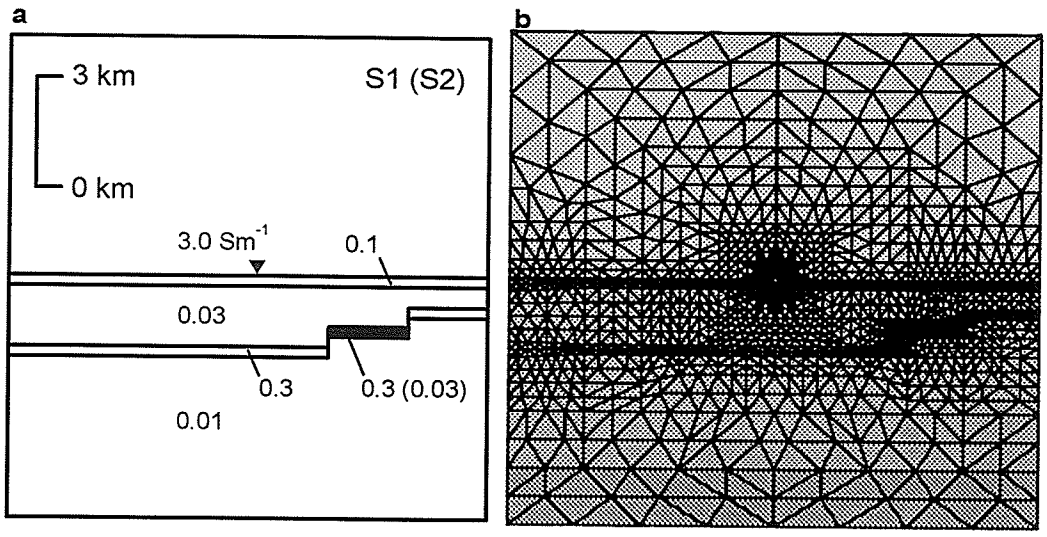

Figure 7.1 (a) Two relatively complex earth models. The conductivity structure is the same in both models except for the shaded region of layer three. In S_1, the conductivity of this up-faulted region of layer 3 is consistent with the rest of layer 3, whereas in S_2 the conductivity of this region is reduced by an order of magnitude. Together, these models represent a change in conductivity within a stratigraphic unit. (b) The FE mesh of the models in (a).

generally diffuses in a vertical path (the most resistive path) down into the lower most resistive layer and then laterally. The effect of the conductive layer three is to greatly reduce the rate of diffusion of the electric field. To the right of the source in figure 7.3a, the effect of the upwards displacement of layer three is to provide a generally more resistive path for diffusion. This is illustrated by the almost horizontal diffusion of the electric field here as compared to the mostly vertical diffusion path to the left of the receiver. Reducing the conductivity of the up-faulted portion of layer three in figure 7.3b enhances the lateral rate of diffusion to the right of the source even more. However, the values for both the magnetic and electric fields at the seafloor appear scarcely affected.

7.3 Geophysical Responses

The magnetic and electric impulse-responses for the stratigraphic models are shown

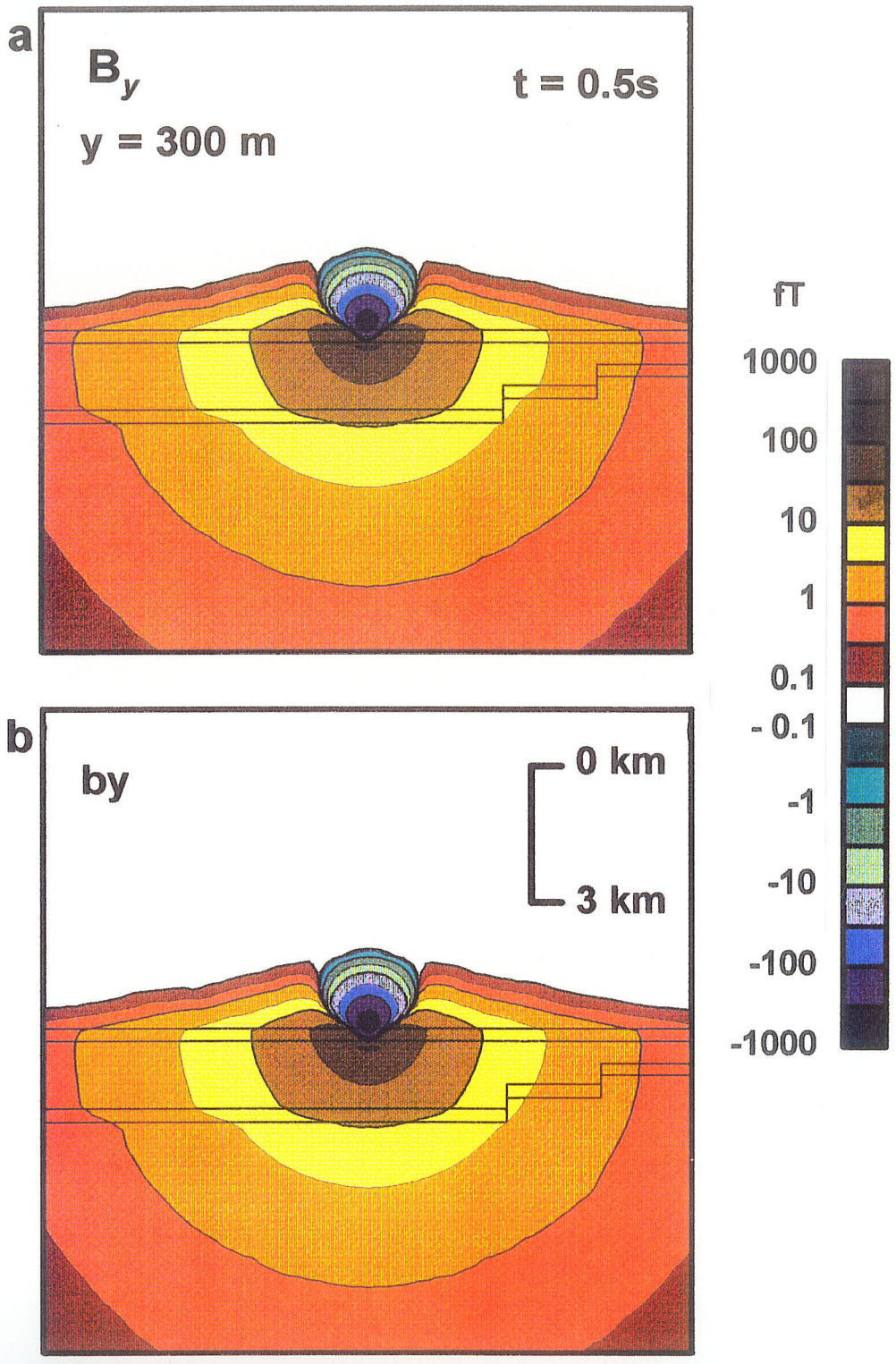

Figure 7.2 Contours of the magnetic field $B_y(x, y, z, t)$ for (a) model S_1 and (b) model S_2 for y=300 m at t=0.5 s after step-on of the HED source.

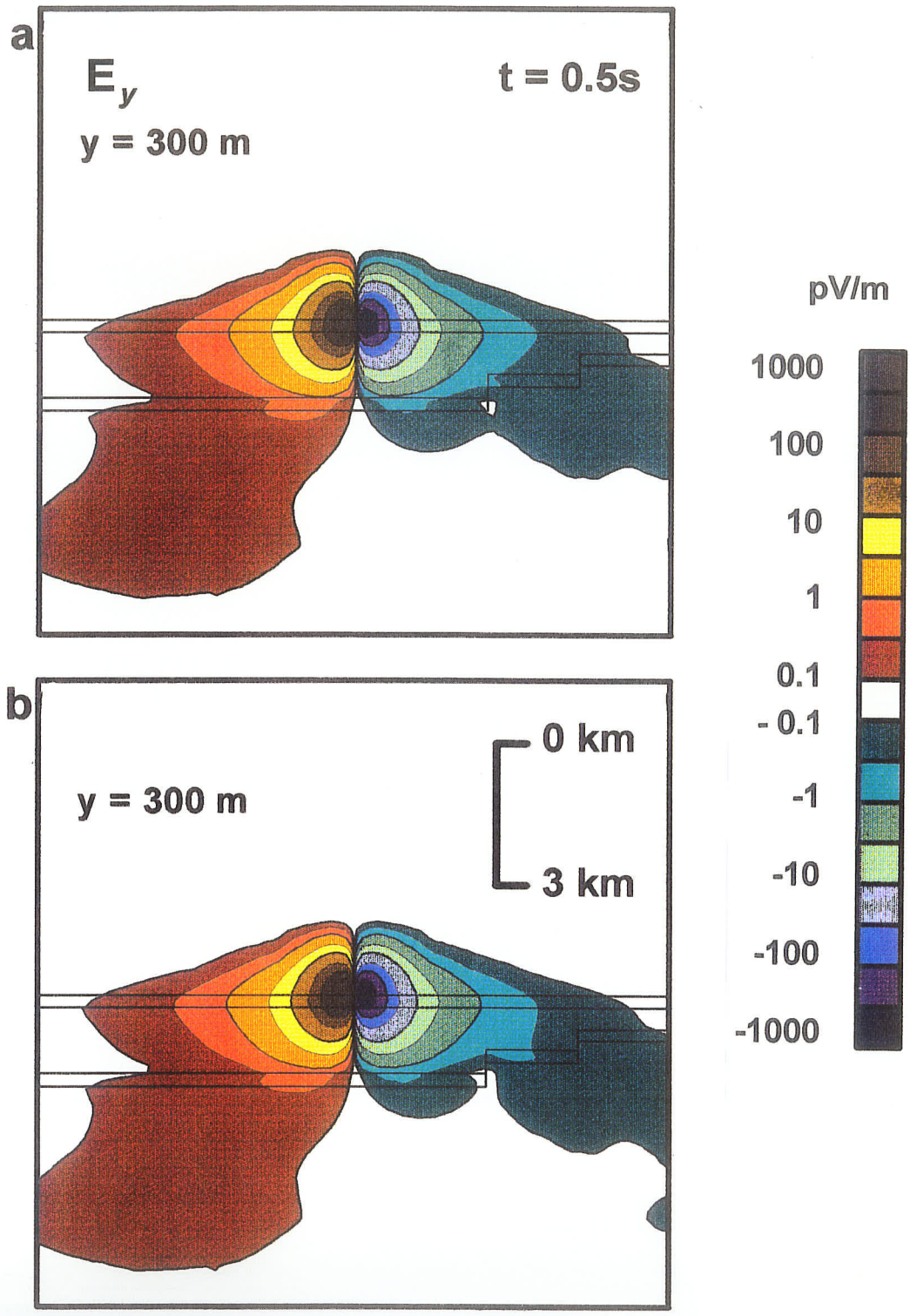

Figure 7.3 Contours of the electric field $\mathbf{E}_y(x, y, z, t)$ for (a) model S_1 and (b) model S_2 for y=300 m at t=0.5 s after step-on of the HED source. Some of the smallest features on the last illustrated contour level may be due to numerical error.

in figures 7.4 and 7.5. The magnetic impulse-response is only shown for y=0 m, as the signal strength is largest in line with the source and there is very little difference in signal shape along-strike. The electric impulse-response is shown for y=1000 m as the signal strength is zero in line with the source. The very early time response is not shown for x=3000-5000 m. These figures illustrate that there is a very small difference in signal amplitude between the two models. The largest amplitude difference appears to occur between 4000 m and 5000 m from the source; this is directly over the right-hand most fault. Interestingly, the amplitude only changes significantly at t $\approx \tau$.

Figure 7.6 shows the arrival time plotted against distance from the source for both the magnetic and electric fields. Figure 7.6a illustrates that there is virtually no difference in arrival time of the magnetic field for the two models at any seafloor location. Figure 7.6b shows a slight differences in arrival time for the electric field at 4500 m and 8000 m from the source. However, this contrast constitutes less than a 5% relative difference in arrival time. Therefore, it can be concluded that the CSEM method is not sensitive to the differences in conductivity structure of two stratigraphic models (at least at the depth studied here). It is not entirely clear why these curves have a distinct "stairstep" appearance, however, it is related to the sudden change of average conductivity of the diffusion path. That is, the average conductivity of the diffusion path of the first arriving signal changes dramatically several times as the distance from the source increases.

7.4 Implications for Hydrocarbon Exploration

The response amplitude and the arrival time of the EM fields for both stratigraphic models in this chapter are almost identical. One reason for the small differences between the models is most likely due to attenuation of the signals through the thin, relatively conductive layer near the surface of the seafloor. However, in the case of most real

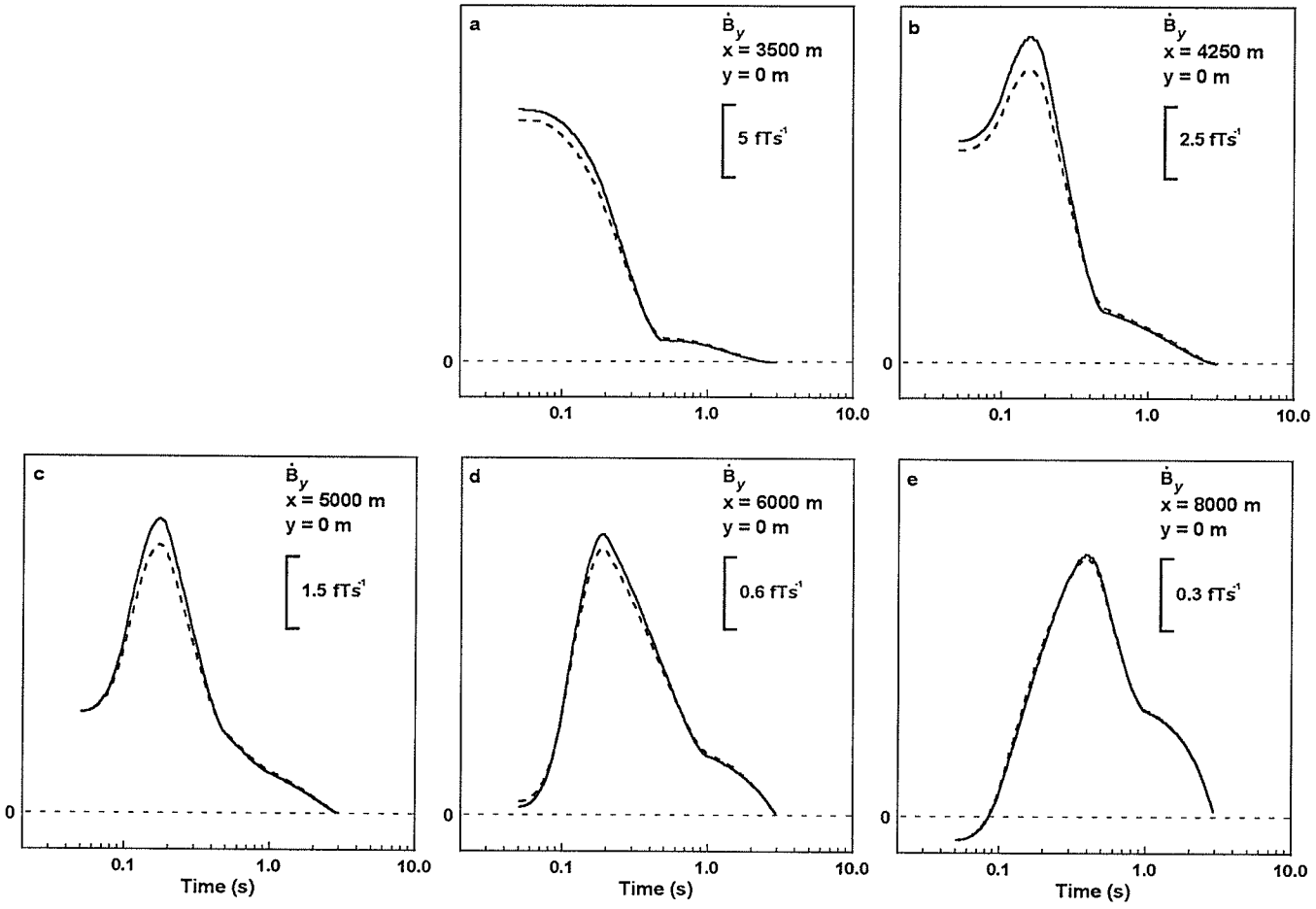

Figure 7.4 Magnetic impulse-response for several seafloor locations comparing the response of models S_1 (dashed) and S_2 (solid). These plots are for y=0 m in the along-strike (y) direction. There is very little difference in amplitude between the signals from the two models indicating that the amplitude of the response is not affected by the change in conductivity within a layer (a stratigraphic change).

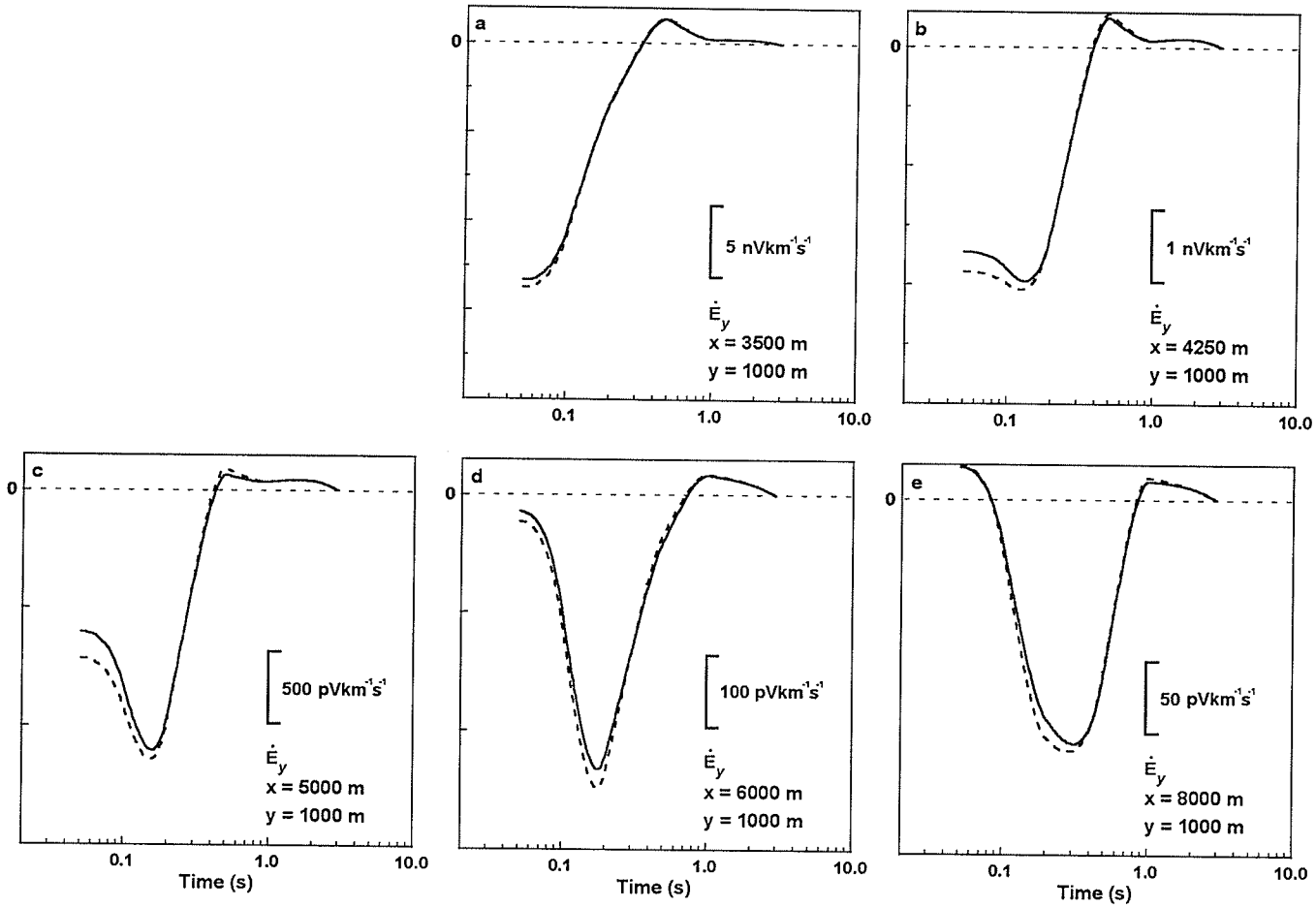

Figure 7.5 Electric impulse-response for several seafloor locations comparing the response of models S_1 (dashed) and S_2 (solid). These plots are for y=1000 m in the along-strike (y) direction. As for the magnetic fields, there is very little difference in the amplitude of the response between the two models, hence the amplitude is not affected by a small stratigraphic change in conductivity.

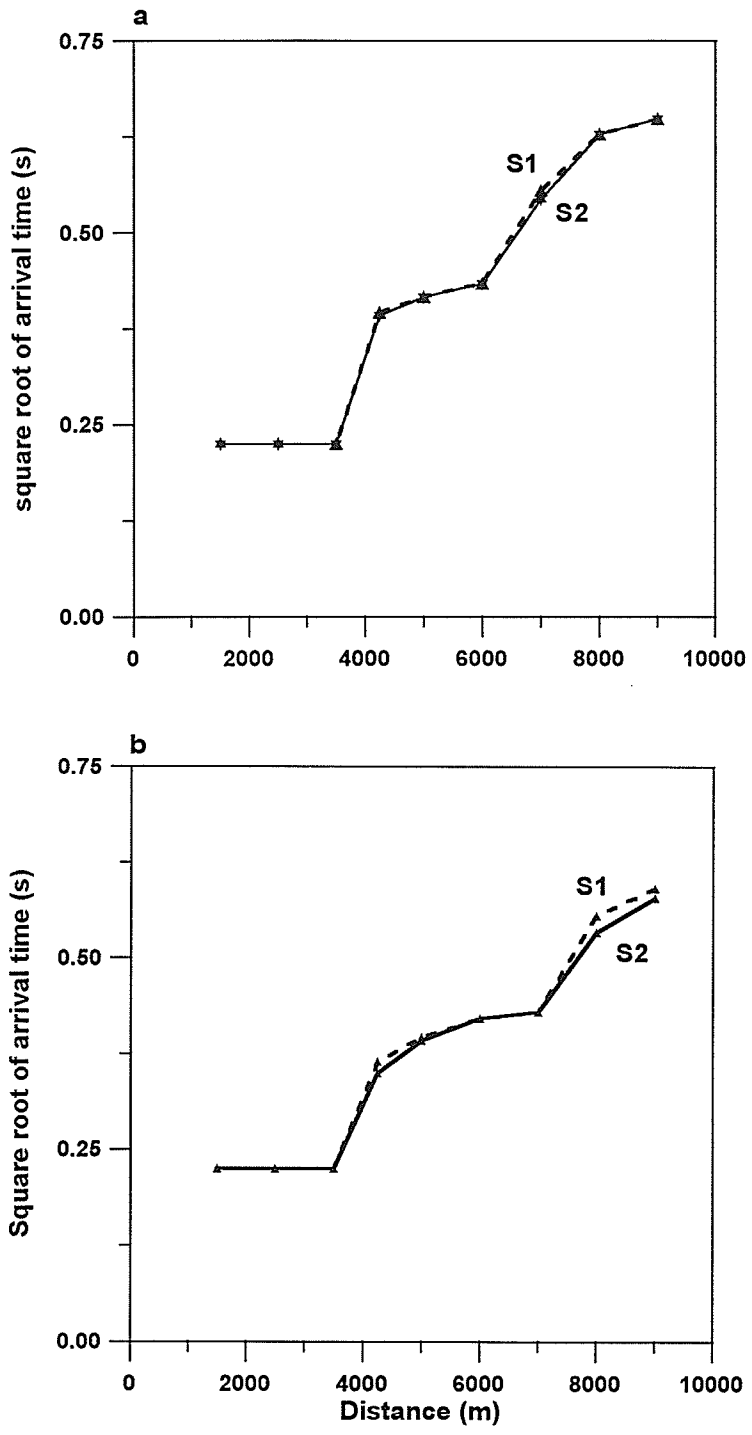

Figure 7.6 Square root of arrival time (a) τ_B for y=0 m and (b) τ_E for y=1000 m comparing models S_1 (dashed) and S_2 (solid). There is virtually no difference in the arrival time of either the magnetic or electric response for the two models, although the electric field does appear to be slightly more sensitive to the change in conductivity.

marine EM surveys, this conductive near surface layer cannot be avoided.

To determine whether changing the conductivity of the layers involved, and increasing the contrasts between the models does provide larger differences in the EM responses, the conductivities in layer 3 of the models in this chapter were increased by one, two, and three orders of magnitude for three diffusion times. Althought there were subtle changes in the shape of the diffusing fields, the amplitude and arrival times of the signals were not changed measureably at the seafloor. The results from this chapter generally show that this method is not sensitive to lateral conductivity changes in an approximately horizontally layered earth. It then follows that the CSEM method using an HED is not well suited to detecting conductivity changes within a single stratigraphic horizon, and therefore cannot be used effectively for hydrocarbon exploration in this type of situation.

Notwithstanding, the results from chapter 6 suggest that the CSEM method is sensitive to more "blocky" structures; the changes in conductivity in the model must change the resistivity of the primary diffusion path. Layered models of the type shown in this chapter do not fulfil this condition. Future modelling and seafloor experiments should concentrate on these types of structures.

A possible target for future modelling that is often associated with hydrocarbon accumulation is a salt dome structure. Such a structure is "blocky", usually has large vertical extent, is often somewhat 2D and provides a large conductivity contrast between the salt and surrounding country rock.

Chapter 8

Modelling of Near Surface Resistive Zones

8.1 Introduction

The modelling results described so far in this thesis have shown that the CSEM method is better suited to detecting conductivity differences in "blocky" earth structures. It has also been found that the method is most sensitive to near surface (less than 1500 m depth) changes in conductivity. Therefore, in this chapter attention is focused on two types of near surface "blocky" conductivity structures that are of recent interest in the exploration for hydrocarbons. The first of these is the presence of near-surface zones of hydrocarbon induced alteration above oil or gas fields (Nekut & Spies, 1989). The second is the occurence of gas hydrates in the near-surface seafloor sediments which have recently become a concern in regards to future global warming (*e.g.* Judge & Majorowicz, 1992) . Both of these anomalous zones may be represented by an electrically resistive block.

As described in chapter 3, it is known that in many sedimentary basins geochemically and geologically anomalous zones overlie petroleum deposits (*e.g.* Sternberg & Oehler, 1990). These zones are thought to be due to the upward migration of petroleum from leaking reservoirs. One consequence of these migrating hydrocarbons is an in-

crease in the concentration of bicarbonate ions. These ions react with the calcium in the near-surface sediment to produce carbonate cement, reducing the porosity of the sediment. This reduction in near-surface porosity often means an increased resistivity in the affected zone (Nekut & Spies, 1989).

Gas hydrates will also create a near-surface resistive zone. Gas hydrates are crystalline, ice-like solids that form when water and a sufficient quantity of certain gases of relatively small molecular size are combined under the right temperature and pressure conditions (*e.g.* Pearson *et al.*, 1986; Stoll & Bryan, 1979). The temperature conditions under which hydrates form and remain stable depends on the pressure of the system and the type of gas hydrate in question, however, many gas hydrates found below the seafloor are stable at temperatures well above 0°C (Shipley *et al.*, 1979). Figure 8.1 illustrates gas hydrate stability conditions for selected locations worldwide.

The occurrence of gas hydrates on the seafloor was first suspected due to an anomalous, bottom simulating seismic reflection (figure 8.2) on the eastern United States margin (Shipley *et al.*, 1979). Seismic evidence suggests that hydrates may be widespread on continental slopes and rises in water depths of 700 m to 4000 m and extend from the seafloor surface to depths of 1000 m subseafloor. Laboratory experiments have showed that the electrical conductivity of the seafloor sediments is decreased by nearly two orders of magnitude with the formation of gas hydrates (Pearson *et al.*, 1986). This decrease in conductivity continues as the temperature is decreased further, reducing the amount of unfrozen brine left in the rock. A large decrease in conductivity in areas containing gas hydrates may be detectable using CSEM methods.

This large decrease in conductivity in areas containing gas hydrates may be detectable using CSEM methods. In 1990, an experiment was conducted by Edwards and Law to attempt to detect gas hydrates in Bute Inlet, BC (Ferguson, Pers. comm.).

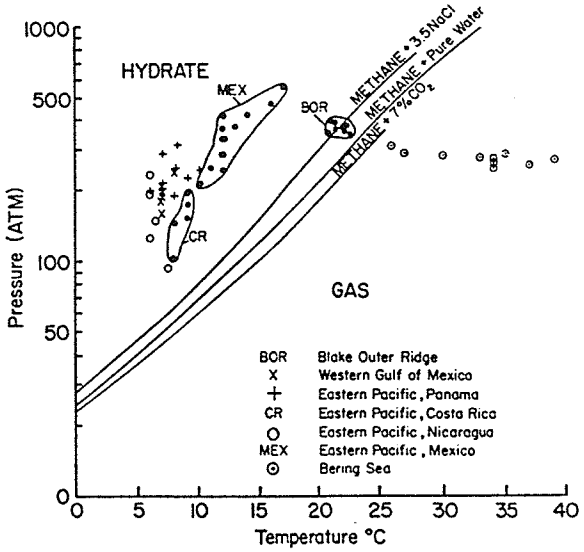

Figure 8.1 Gas hydrate stability relations (from Shipley *et al.*, 1979).

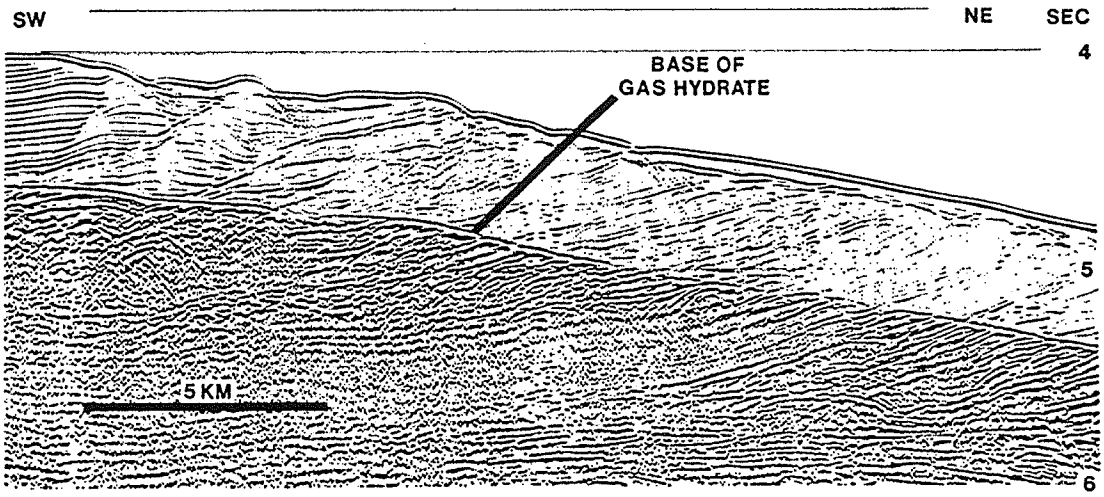

Figure 8.2 A 12-fold multichannel seismic reflection profile from the crest and eastern flank of Blake Outer Ridge (from Shipley *et al.*, 1979). Apparent lower amplitude above the hydrate base is probably real.

This survey employed an electric source and magnetometer receivers. However, due to instrumental problems, no data was recorded.

8.2 Model with Near Surface Resistive Zones

The zones of hydrocarbon induced alteration and gas hydrates will be represented with the same conductivity models. The four models for which the response is calculated are shown in figure 8.3. To provide a more geologically reasonable representation, all four models are based on a three layer earth with the conductivity decreasing as depth increases (*e.g.* Nobes *et al.*, 1986). For three of the models, a zone of low conductivity 200 m thick and 2500 m long is inserted into the model just below the seafloor surface. The fourth model has no resistive zone and is employed as a control model. This set of models is used 1) test whether CSEM methods are able to detect the *existence* and *location* of a near surface resistive zone, and 2) test the sensitivity of the method to differences in the conductivity of this anomalous zone.

In model A_1 (figure 8.3a), the top of the anomalous zone is located at the seafloor surface and the conductivity is one order of magnitude lower than the conductivity in the surounding layer. The conductivity of model A_2 (figure 8.3b) is the same as A_1, but the thin anomalous zone is moved 200 m down from the surface of the seafloor. The structure of model A_3 is the same as A_2, but the conductivity is increased so that the contrast with the surrounding layer is only one half an order of magnitude. Model A_4 (figure 8.3c) has no resistive zone near the surface, but is otherwise identical to the first three models discussed above. In all four models, the EM source is located 1000 m to the left of the anomalous zone.

The FE mesh in figure 8.3d is approximately the same size as the meshes generated for the fault models in chapter 6 but much smaller than the stratigraphic models in

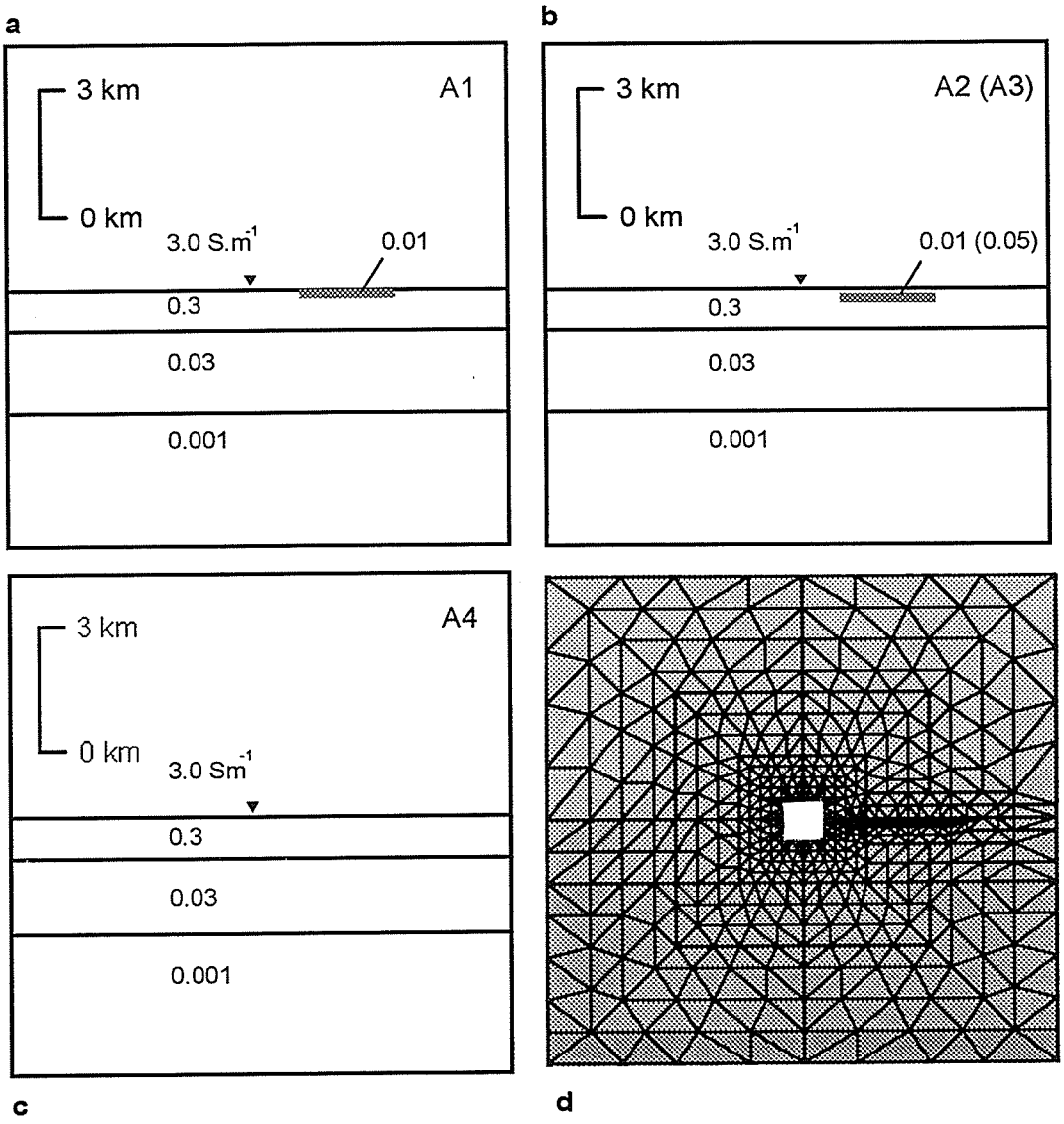

Figure 8.3 A layered earth model containing a near-surface resistive zone (shaded), representing two possibilities: hydrocarbon induced alteration, or gas hydrate deposits. The anomalous zone is 200 m thick and 2500 m wide. The zone is located (a) at the seafloor surface for model A_1, and (b) 200 m below the seafloor for models A_2 and A_3. The anomalous zone in model A_3 is not quite as resistive as in model A_2. (c) Model A_4 has no resistive zone. (d) The finite element mesh is shown for model A_1.

chapter 7. Since the resistive block being modelled is very thin, the node density around it must be increased to keep the aspect ratio of the elements from becoming too large as discussed in chapter 7. The mesh for model A_1 has N=1300 nodes and 2536 triangular elements. The solution time for one "snapshot" of the magnetic and electric fields requires approximately 5.7 cpu minutes on the Fujitsu VPX240/10 supercomputer. The computer program attains approximately 45% vectorization for these models.

Contour plots showing the diffusion patterns of the along-strike magnetic $\mathbf{B}_y$ and electric $\mathbf{E}_y$ fields for model A_1 are shown in figures 8.4-8.6. The fields are displayed for a range of times 0.1 s $\leq$t$\leq$ 0.5 s after activation of the HED source, and for a range of distances 0 km $\leq$y$\leq$ 3 km in the along-strike direction. Figures 8.4b-8.6b show that the electric field diffuses much faster through the resistor than through the more conductive material to the left of the source. However, the pattern of the contours shows a complex interaction of the electric field with the resistive layer much like those of the layered half spaces in chapter 5. Near the bottom of the resistive layer, there is a group of field contours with the opposite sign (positive) as the fields in the surrounding area. This change of sign of the electric field is due to electric currents induced by the rapidly changing magnetic field. These currents are located in the conductive layer just below the resistive layer and are in the opposite direction as those in the HED source. These currents are a *secondary* EM source.

Figures 8.4a-8.6a show that the magnetic field also diffuses much faster through the resistive zone to the right of the source than through the more conductive earth to the left. This effect is most obvious at earlier times (*e.g.* t=0.2 s). At later times (*e.g.* $t \geq$0.5 s) and large distance along-strike (y=3000 m) the magnetic field also displays some of the complexity seen in the electric field contours. This affect is presumably related to the change in sign of the electric field near the resistor. The small scale structures on

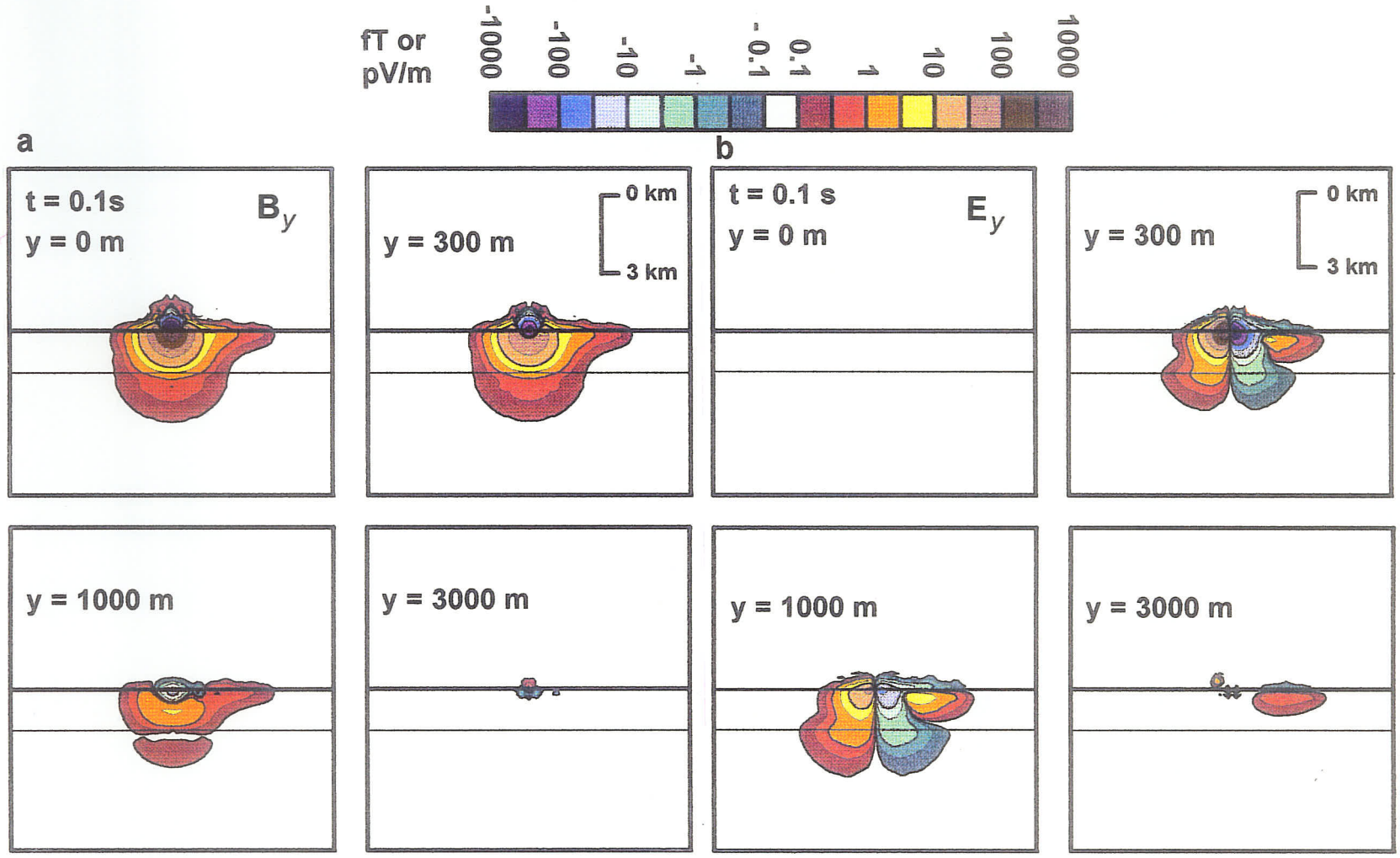

Figure 8.4 Contours of (a) $\mathrm{B}_y(x, y, z, t)$, and (b) $\mathrm{E}_y(x, y, z, t)$ in three spatial dimensions showing diffusion of EM fields into model A_1 at time t=0.1 s after step-on of the HED source.

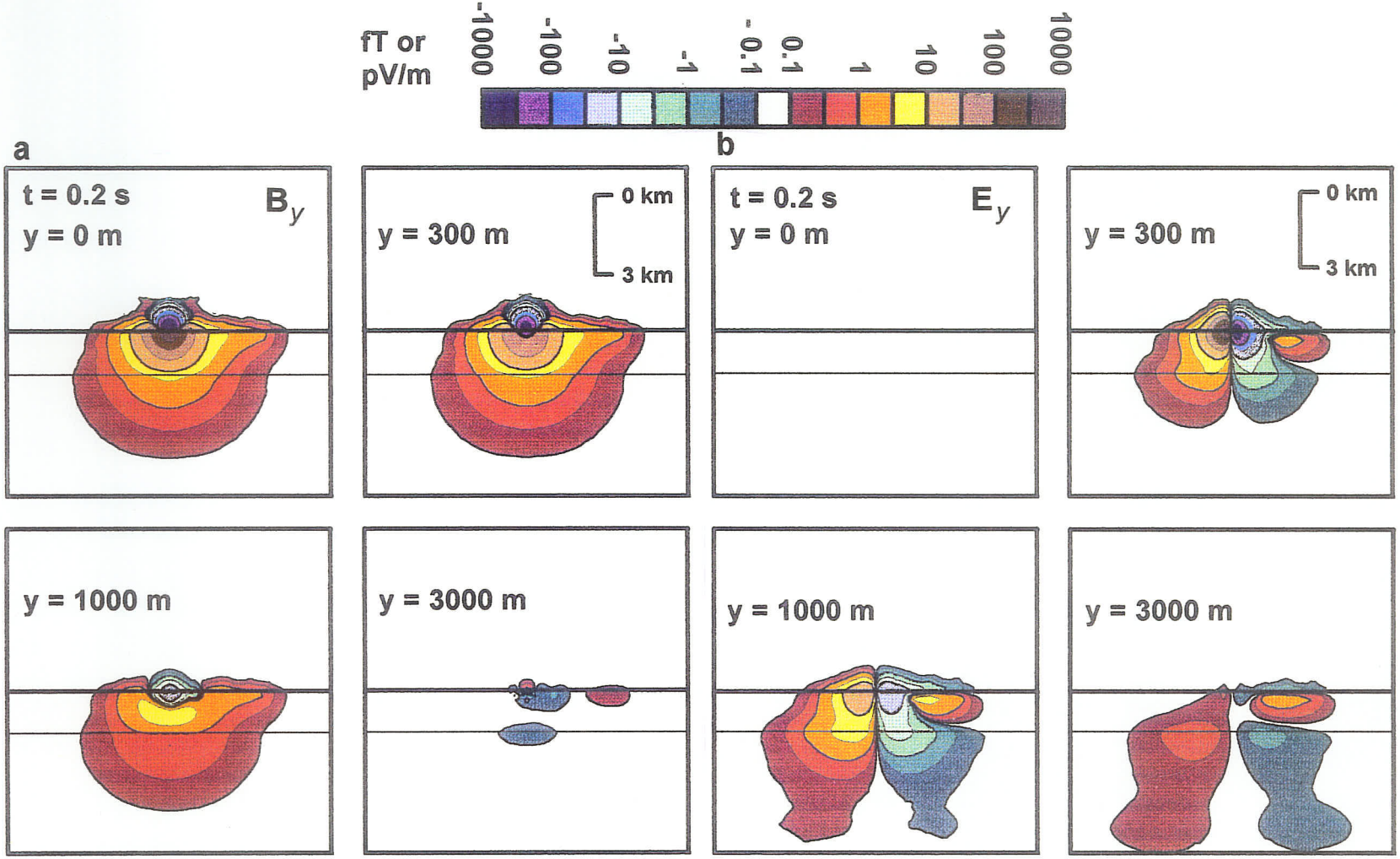

Figure 8.5 Contours of (a) $\mathrm{B}_y(x, y, z, t)$, and (b) $\mathrm{E}_y(x, y, z, t)$ in three spatial dimensions showing diffusion of EM fields into model A_1 at time t=0.2 s after step-on of the HED source.

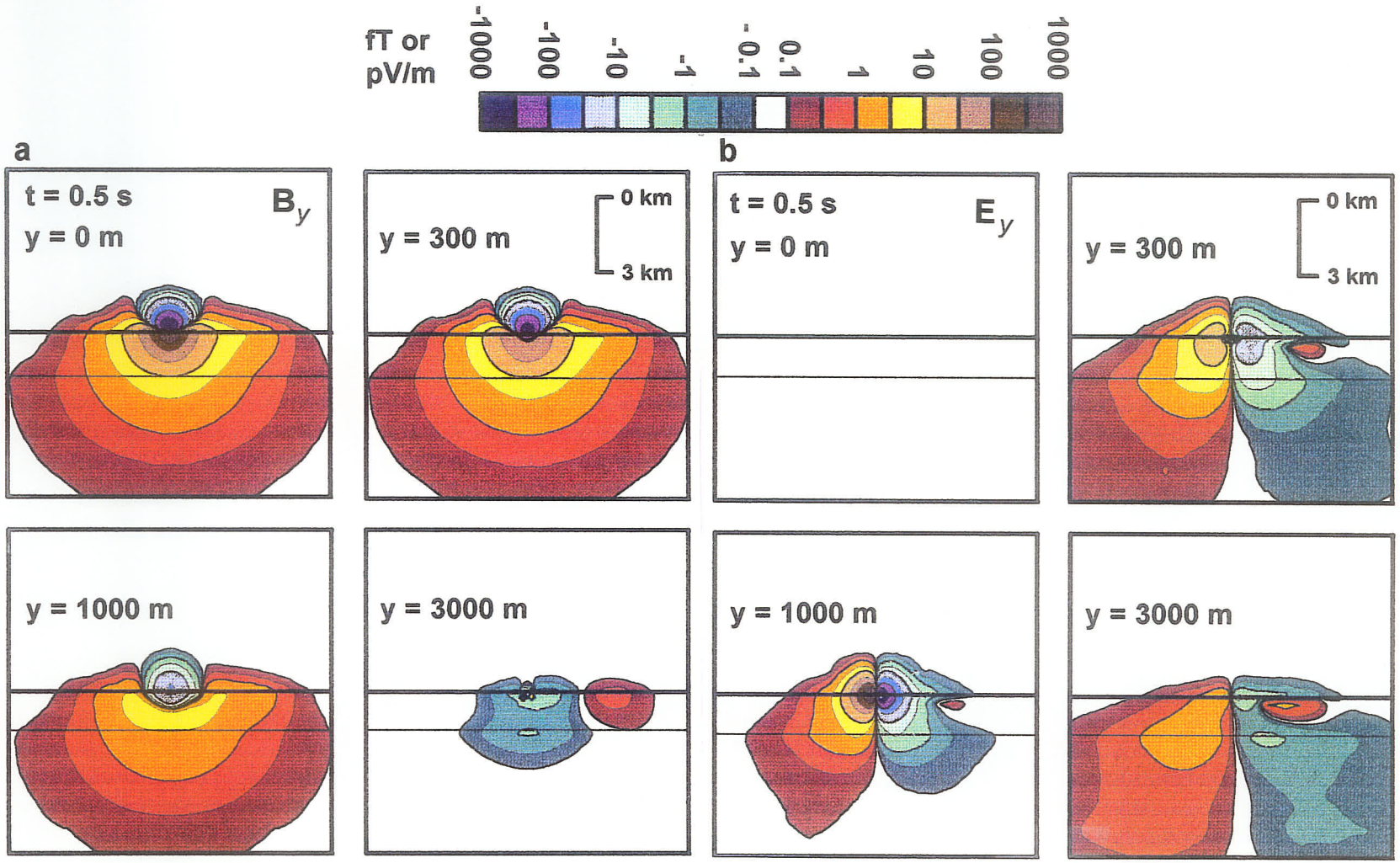

Figure 8.6 Contours of (a) $\mathrm{B}_y(x, y, z, t)$, and (b) $\mathrm{E}_y(x, y, z, t)$ in three spatial dimensions showing diffusion of EM fields into model A_1 at time t=0.5 s after step-on of the HED source.

the last contour level in the seafloor fields are most likely due to numerical noise.

8.3 Geophysical Responses

The magnetic and electric impulse responses for all four models are shown in figures 8.7 and 8.8 respectively. The first plot shows the response at a seafloor location over the left end of the resistive zone. The last plot is for a location over the conductive layer, 750 m to the right of the resistive zone. Recall from chapter 2, that the detection limits of currently available magnetic and electric field receivers is about 10^{-5} nT and 1 pVm^{-1} respectively. Recall also that a typical seafloor survey may employ a source with a dipole moment of 5×10^4 Am. This value will be used for scaling the EM responses.

To the left of the resistive target, the response curves for all of the models are virtually identical and therefore are not shown. As the receiver locations move to the right, over the resistor, differences in amplitude and arrival time become evident from one model to the next. These differences between models increases toward the right side of the resistor. Three comparisons will be made below: models A_1-A_4 (determination of existance/location of the resistor), models A_2-A_3 (determination of conductivity resolution), and models A_1-A_2 (determination of depth resolution).

Models A_1 and A_4 are the least similar of the four models in this chapter. Therefore, these two models are the first to be compared to determine whether or not the CSEM system modelled is capable of resolving the existance of a resistive body in the near subsurface. At x=1250 m, the impulse response curves for the models do not seem to differ much. However, by x=2000 m (directly over the resistor), the amplitude of the magnetic impulse curves differ by 11 fTs^{-1} and the amplitude of the electric impulse curves differ by 9 $\mu Vkm^{-1}s^{-1}$. Using the source described above, these differences translate to 550 nTs^{-1} and 45 $\mu Vm^{-1}s^{-1}$ respectively; well within the detectable limits

of today's receivers. In fact, even the relatively small differences in response curves at x=1250 m are easily resolveable using present technology. Although there are fairly large differences in response amplitude from one model to the next, it is unlikely that two models would be discernable using this information alone. The arrival time differences between models ranges from 0.02 s at the first receiver location to as much as 0.3 s at the last location. Figure 8.9 illustrates this large difference in arrival time between the two models. Over the resistor, the arrival time curve for A_1 has a much smaller slope than the curve for A_4. To the right of the resistor, the slope of the A_1 curve increases to parallel the A_4 curve. These two observations indicate that the two models have different conductivity where their respective slopes differ. Thus, the CSEM system is capable of detecting the existance *and* location of a near-surface resistive zone.

Models A_2 and A_3 differ only in the conductivity of the target. Similar to the above comparison, the magnetic and electric impulse response curves differ by 4 fTs^{-1} and 4 $\mu Vkm^{-1}s^{-1}$ respectively at x=2500 m. Using the above source, this translates to 200 nTs^{-1} and 20 $\mu Vm^{-1}s^{-1}$, again well within the limits of today's receivers. The arrival time differences range from 0.02 s at the first receiver to 0.35 s at the last receiver. Figure 8.9 shows that the slope of the A_2 arrival time curve is less than the A_3 curve only over the resistor. However, past the end of the resistor, the slope of the two curves is equal. Although the differences in model response are not as large as in the first comparison, the CSEM system is sensitive to even small changes of conductivity in the near subsurface.

Models A_1 and A_2 have the same size resistive block, but differ in the depth to this resistor. Although the response curves for these models *appear* similar at every receiver location, there are measurable differences. The magnetic and electric impulse responses never differ by more than 3.5 fTs^{-1} and 5 $\mu Vkm^{-1}s^{-1}$ respectively. These

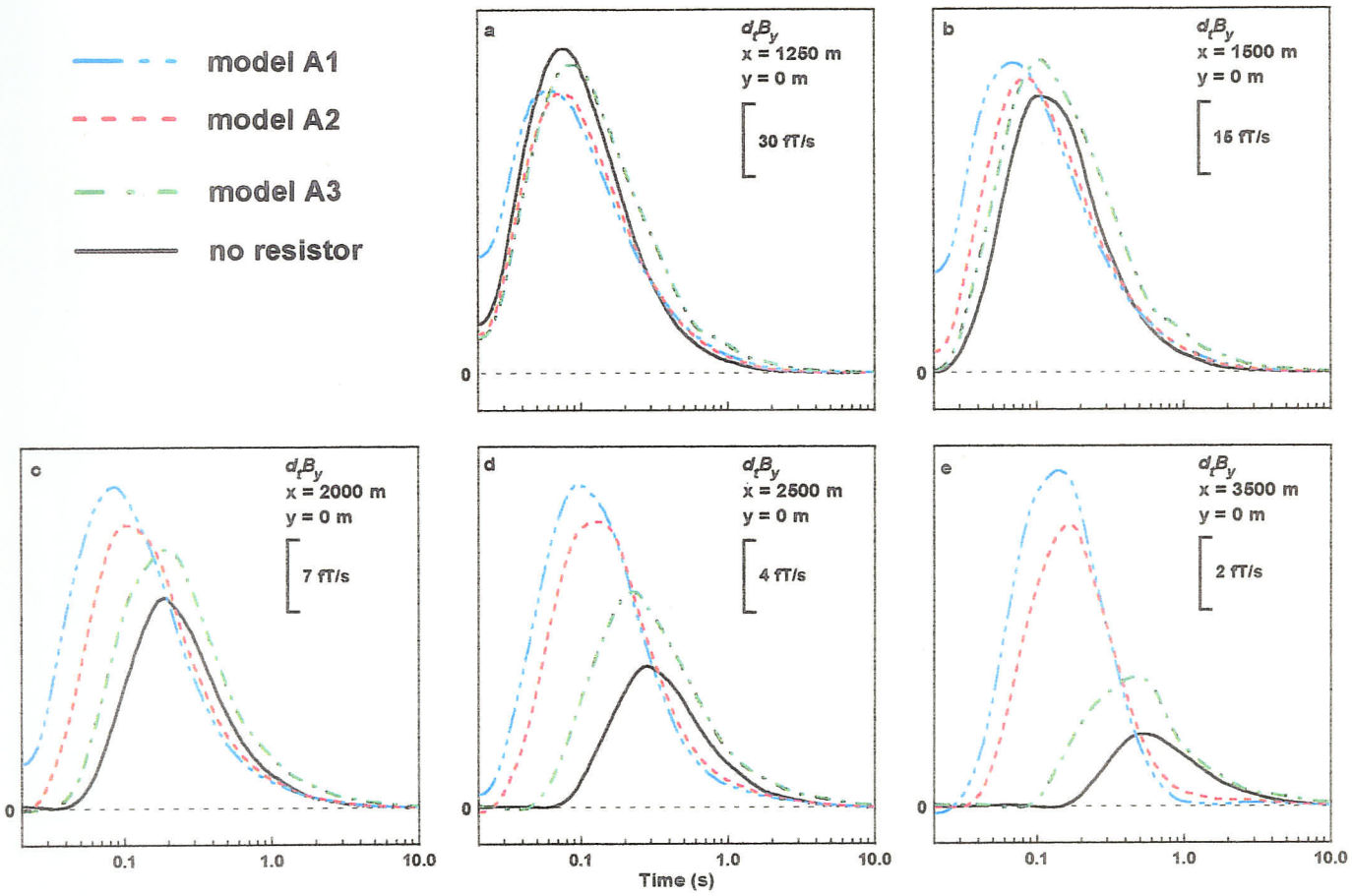

Figure 8.7 Magnetic impulse-response for several seafloor locations comparing the response of models A_1,A_2, A_3, and a layered earth without the resistive zone present (A_4). These plots are for y=0 m in the along-strike direction. There is very little difference in amplitude between the signals from models A_1 and A_2. However, there is a large difference between these first two models and the response when no resistive zone is present (A_4).

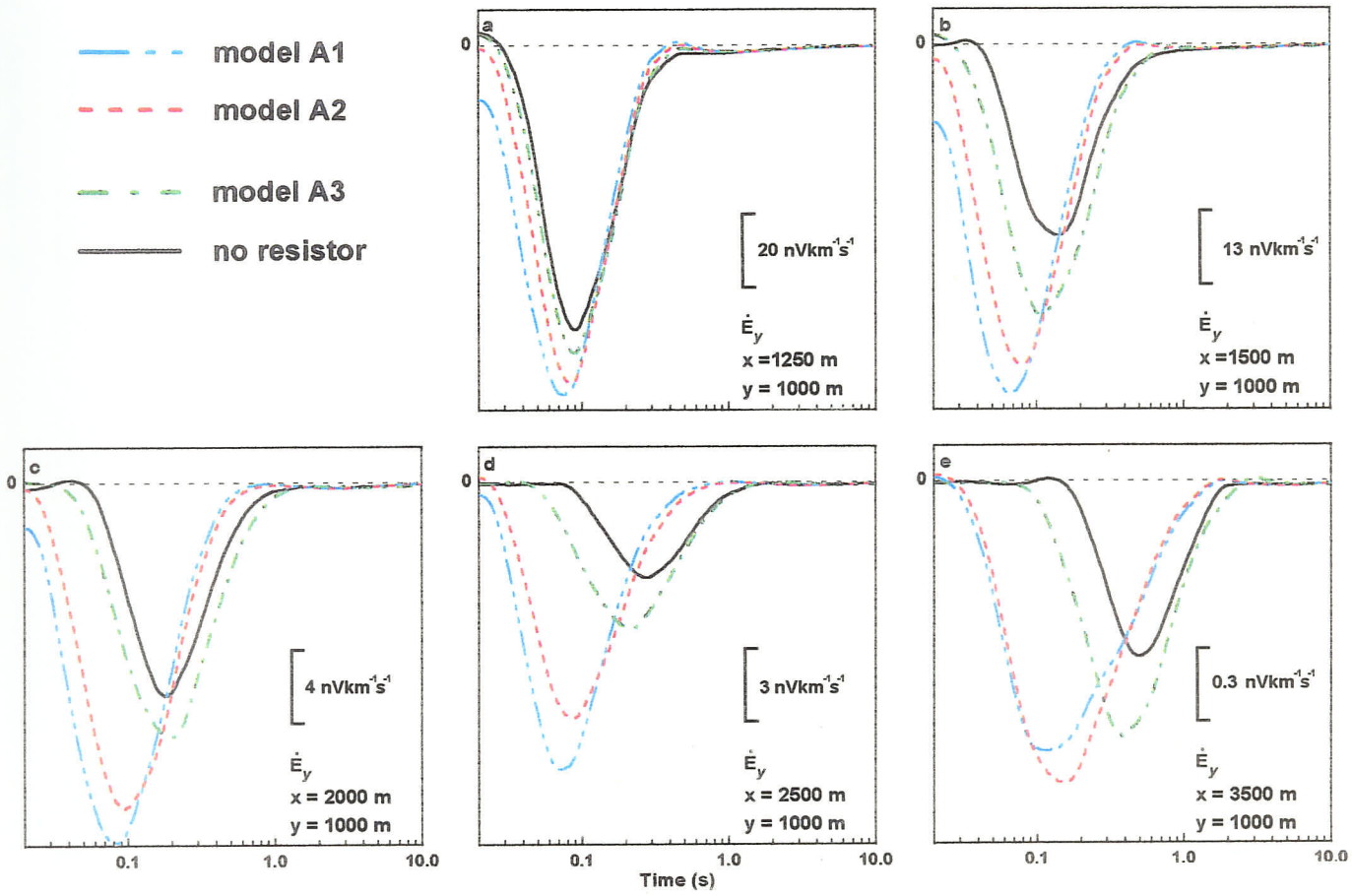

Figure 8.8 Electric impulse-response for several seafloor locations comparing the response of models A_1, A_2, A_3, and a layered earth without a resistive zone present (A_4). These plots are for y=1000 m in the along-strike direction. As for the magnetic fields, there is very little difference in the amplitude of the response between the first two models, however, there is a marked contrast between the response from these models and that when no resistive zone is present (A_4).

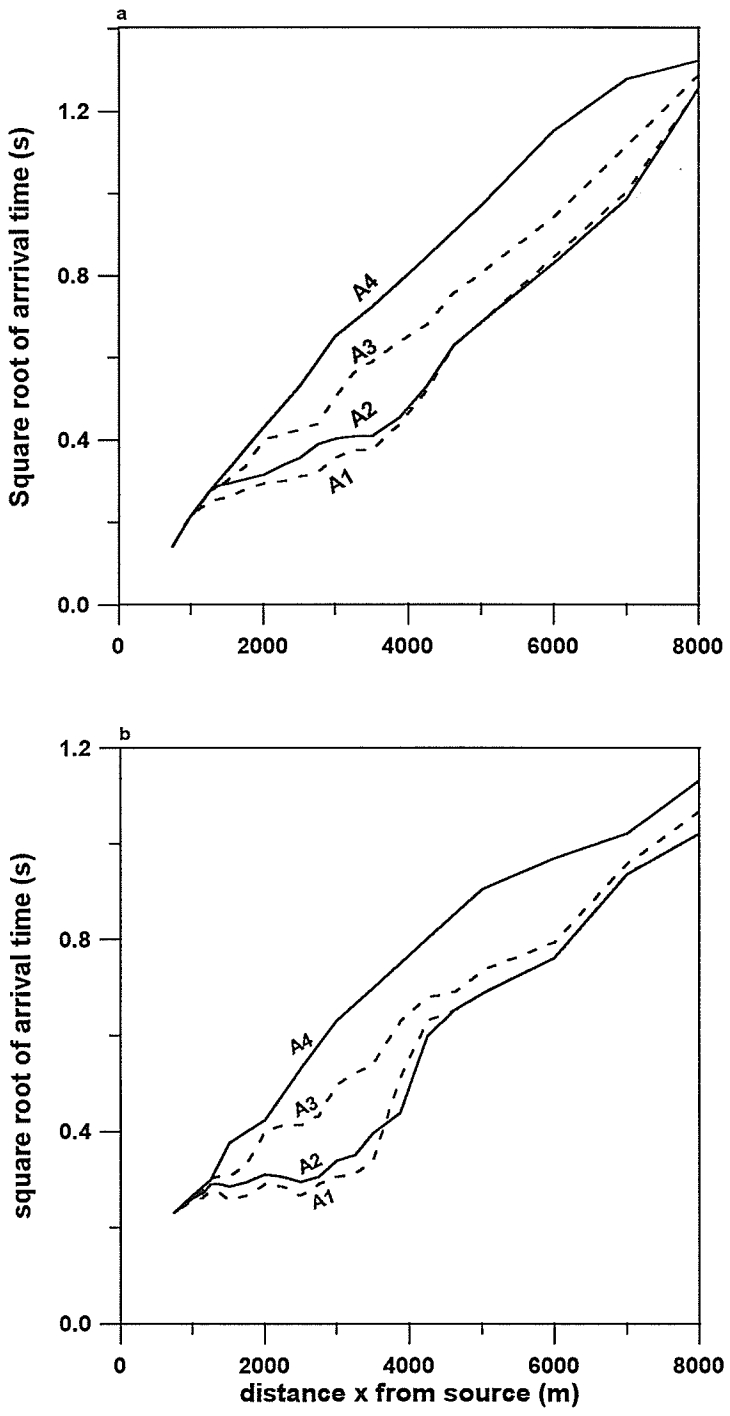

Figure 8.9 Square root of arrival time for (a) τ_B at y=0 m and (b) τ_E at y=1000 m comparing models A_1, A_2, A_3 and a layered earth without a resistive zone present (A_4). The slope of the arrival time curves for A_1 and A_2 are significantly lower over the resistive zone than over the non-resistive zone. However, there is relatively little difference in the arrival time of either the magnetic or electric response for models A_1 and A_2.

differences are similar to those in the second comparison. The largest arrival time difference is approximately 0.02 s. Although these differences in arrival time are noticable in figure 8.9, the shape of the respective curves are very similar looking, making a depth interpretation based on one source not likely. However, these results suggest that by using numerous source locations on the seafloor, a CSEM system is capable of resolving significant changes in the depth to a resistive target.

8.4 Implications for Hydrocarbon Exploration

The results discussed in §8.3 clearly demonstrate the sensitivity of the CSEM method to near-surface zones of high resistivity below the seafloor. However, the resistive zones modelled in this chapter are only 200 m in thickness, and as discussed in this chapter and chapter 3, gas hydrates and near-surface alteration often occur in much thicker zones. Therefore, it may be concluded that the CSEM system could be used for locating zones of gas hydrates or hydrocarbon alteration below the seafloor.

The survey parameters required for an EM experiment to detect a near-surface resistive zone as in model A_1 are not extreme. A source dipole moment of 10^4Am and electric receiver dipoles of 100 m in length would be sufficient. This configuration is much smaller than the maximum possible and would therefore be less expensive. The magnetic fields being measured are larger than 1 nTs^{-1}, therefore induction coils could be used instead of the more expensive and tempermental SQUID magnetometers. The receivers and recording equipment must be capable of sampling the fields at a minimum of 50 Hz.

For convenience, the electric and magnetic responses described in chapters 6 to 8 are summarized in table 8.1. Recall that all of the values presented thus far are for a unit dipole source and must be scaled accordingly.

Table 8.1: Summary of EM responses for Thesis

Model	Distance from Source (m)	B or E	τ (s)	Max Difference (s)	By or Ey (fT/s or nV/km.s)	Max. Difference (fT/s or nV/km.s)
Structural	2000	B	0.18	very small	20	~ 0.1
	3500	B	0.5	0.07	1.8	0.3
	5000	B	0.9	0.3	0.6	0.2
	2000	E	0.18	very small	11	1
	3500	E	0.5	0.1	0.65	0.2
	5000	E	0.85	0.3	0.5	0.1
Stratigraphic	4250	B	0.15	very small	11	1
	5000	B	0.18	very small	6	0.5
	8000	B	0.35	very small	1	~ 0.01
	4250	E	0.15	very small	3.3	0.2
	5000	E	0.18	very small	1.8	0.05
	8000	E	0.35	very small	0.2	~ 0.005
Gas Hydrates	1250	B	0.06	0.03	130	15
	2000	B	0.09	0.11	30	5
	3500	B	0.15	0.35	9	5.5
	1250	E	0.07	0.02	90	18
	2000	E	0.085	0.12	18	8
	3500	E	0.12	0.3	1.1	0.4

Chapter 9

Conclusions

Controlled-source EM surveys are logistically complex and expensive to perform in a marine environment. These surveys require the use of a large ocean-going ship for an extended period of time and many seafloor magnetic and electric field receivers, all of which are very costly. Therefore, numerical design studies are needed before an experimental survey is considered, both to examine the feasibility of the method as an exploration tool for hydrocarbons and to provide estimates of the signal levels to be expected at the EM receivers. The aim of this research was to use a finite element modelling program to predict the EM fields which would be measured in realistic seafloor EM soundings, to investigate the sensitivity of the response to the underlying geological structure, and furthermore, to provide some constraints on survey parameters for future seafloor EM surveys.

The CSEM system modelled consists of a horizontal electric source dipole and inline horizontal electric and magnetic field receivers oriented perpendicular to the source dipole. Several different scenarios were studied: single layers, multiple layers, faults, stratigraphic changes, and near-surface resistive layers.

The finite element meshes for the simpler models contained about N=1200 nodes, 2500 triangles, and were reasonably simple to generate. However, the models in chapters

7 and 8 are more complex and their meshes require more time and experience to generate. Due to the relatively thin layers being represented, the meshes have as many as N=2240 nodes and 4420 elements. This is because the interpolating polynomials work best if the aspect ratios of the triangular elements is less than 5:1; therefore the node density must be increased in and around the thin layers.

The computer time required for solving the fields over the finite element meshes and the level of vectorization of the computer code both increase as the number of nodes increases. A typical "snapshot" of the fields at one time requires between 4.5 and 10.5 cpu minutes on the Fujitsu VPX240/10 supercomputer with a 45-55% vectorization rate being attained. This is a very low level of vectorization, suggesting that significant improvement in the computer code is possible.

The geophysical response curves from the fault models show that there is little difference in signal amplitude from model to model. However, there are small, yet resolveable differences in signal arrival time between models. These differences suggest that by using more than one source location, the CSEM method is capable of determining whether there is a significant conductivity discontinuity associated with a fault, and where that discontinuity is located.

The geophysical results from the stratigraphic model indicate that there is virtually no difference in signal amplitude or arrival time between the two models tested. When the conductivity contrast within the stratigraphic test layer was increased substantially, there was still no significant difference in response. Therefore, it may be concluded that, at the depth in question (> 1500m), the CSEM system modelled is not sensitive to the differences in conductivity within a single layer caused by a stratigraphic change. Presumably, a much shallower stratigraphic target would provide a more notable response.

The response curves from the series of models containing near-surface resistive

layers show the greatest sensitivity to changes in model conductivity and structure. This is largely due to the shallow depth of the structure being modelled. The response indicated that the CSEM method is capable of not only detecting the existance and location of a near-surface resistive zone, but also the depth to the resistor and its conductivity contrast with the surrounding rock. These targets appear to be the most promising in terms of hydrocarbon exploration. Further work on this type of model might include changing the thickness of the resistive block.

Generally, the results from the modelling show that the CSEM method is more sensitive to conductivity structures with large vertical extent than to thin, layered structures. That is, to provide a significant response, the structure must lie in the primary diffusion path of the EM fields. As might be expected, the modelling also showed larger response differences for near surface changes in conducitivity than for deeper changes.

To detect a near-surface resistive layer such as a deposit of gas hydrates, a moderate CSEM system is sufficient. A source dipole moment of 10^4A.m and electric receiver dipoles of 100 m in length are more than adequate. An induction coil is sufficient to measure the magnetic fields, thus sparing the expense of using SQUID magnetometers. The receivers and recording equipment must be capable of sampling the fields at a minimum of 100 Hz. These survey parameters are much smaller than possible, thereby greatly reducing the cost of performing an experiment.

References

Bannister, P.R., 1968, Determination of the electrical conductivity of the sea bed in shallow water, *Geophys.*, **33**, 995-1003.

Bindoff, N.L., Filloux, J.H., Mulhearn, P.J., Lilley, F.E.M., and Ferguson, I.J., 1986, Vertical electric field fluctuations at the floor of the Tasman Abyssal Plain, *Deep-Sea Res.*, **33**, 587-600.

Boyce, T.T., and Ferguson, I.J., 1994, Marine controlled-source electromagnetics for hydrocarbon exploration, *Proc. Supercomputing Symp. '94*, J.W. Ross *ed.*, 61-68.

Boyce, T.T., and Ferguson, I.J., 1995, Finite element modelling for marine petroleum exploration, *Proc. Supercomputing Symp. '95*, V. Van Dongen *ed.*, 159-173.

Breiner, S., 1981, Magnetometers for geophysical applications, in *SQUID Applications to Geophysics*, H. Weinstock and W. Overton *eds.*, Soc. Expl. Geoph., Tulsa, OK, 3-10.

Chave, A.D., 1983, Numerical integration of related Hankel transforms by quadrature and continued fraction expansion, *Geophys.*, **48**, 1671-1686.

Chave, A.D., and Cox, S.C., 1982, Controlled electromagnetic sources for measuring electrical conductivity beneath the oceans. 1. Forward problem and model study, *J.Geoph.Res.*, **87**, 5327-5338.

Chave, A.D., Constable, S.C., and Edwards, R.N., 1991, Electromagnetic exploration methods for the seafloor, in *Electromagnetic Methods in Applied Geophysics, vol. 2, Application, Part B*, M.N. Nabighian *ed.*, Soc. Expl. Geoph., Tulsa, OK, 931-966.

Cheesman, S.J., Edwards, R.N., and Chave, A.D., 1987, On the theory of sea-floor conductivity mapping using transient electromagnetic systems, *Geophys.*, **52**, 204-217.

Cheesman, S.J., Edwards, R.N., and Law, L.K., 1990, A test of a short-baseline sea-floor transient electromagnetic system, *Geoph. J. Int.*, **103**, 431-437.

Coggon, J.H., and Morrison, H.F., 1970, Electromagnetic investigation of the sea floor,

Geophys., **35**, 476-489.

Constable, S.C., 1990, Marine electromagnetic induction studies, *Surv. in Geophys.*, **11**, 303-327.

Constable, S.C., Hoverston, M., Morrison, F., and Orange, A., 1994, Seafloor MT for petroleum exploration, *Proc. of Electromagnetic Induction in the Earth, 12th Workshop*, Brest, France, p52.

Cox, C.S., Constable, C.S., Chave, A.D., and Webb, S.C., 1986, Controlled-source electromagnetic sounding of the oceanic lithosphere, *Nature*, **320**, 52-54.

Edwards, R.N., and Chave, A.D., 1986, A Transient electric dipole-dipole method for mapping the conductivity of the sea floor, *Geophys.*, **51**, 984-987.

Edwards, R.N., and Cheesman, S.J., 1987, Two-dimensional modelling of a towed transient mangetic dipole-dipole sea floor EM system, *J. Geoph.*, **61**, 110-121.

Evans, R.L., Constable, S.C., Sinha, M.C., Cox, C.S., and Unsworth, M.J., 1991, Upper crustal resistivity structure of the east pacific rise near 13° N, *Geophys. Res. Let.*, **18**, 1917-1920.

Everett, M.E., 1990, *Active electromagnetics at the mid-ocean ridge, PhD. Thesis,* Toronto, University of Toronto, 139 pp.

Everett, M.E., and Edwards, R.N., 1989, Electromagnetic diffusion computations with applications to geophysical exploration of midocean ridge structures, *Proc. Supercomputer Symp.* '89

Everett, M.E., and Edwards, R.N., 1992, Transient marine electromagnetics: the 2.5-D forward problem, *Geophys. J. Int.*, **113**, 545-561.

Ferguson, I.J., and Edwards, R.N., 1994, Electromagnetic mode conversion by surface-conductivity anomalies: applications for conductivity soundings, *Geophys. J. Int.*, **117**, 48-68.

Filloux, J.H., 1974, Electric field recording on the sea floor with short span instruments, *J. Geomag. Geoelectr.*, **26**, 269-279.

Filloux, J.H., 1987, Instrumentation and experimental methods for oceanic studies, in *Geomagnetism, Vol. 1*, J.A. Jacobs *ed.*, London, 627pp.

Judge, A.S., and Majorowicz, J.A., 1992, Geothermal conditions for gas hydrate stability in the Beaufort-Mackenzie area: the global change aspect, *Palaeogeog.*,

Palaeoclim., and Palaeoecol., **98**, 251-263.

Keller, G.V., 1983, Use of EM sounding for oil exploration, *Abstracts, Aust. S.E.G. Biennial Conf.*, 97-98.

Keller, G.V., 1987, Rock and Mineral Properties, in *Electromagnetic Methods in Applied Geophysics, Vol. 1, Theory*, M.N. Nabighian *ed.*, Soc. Expl. Geoph., Tulsa, OK, 13-51.

LeRoy, G.V., 1977, Classification of oil and gas traps - a summary, in *Subsurface Geology; Petroleum, Mining, Construction*, L.W. Leroy, D.O. LeRoy, and J.W. Raese *eds.*, Golden, Colorado School of Mines, 941pp.

McNeill, J.D., 1990, Use of electromagnetic methods for groundwater studies, in *Geotechnical and Environmental Geophysics*, Vol. I Review & Tutorial, S.H. Ward *ed.*, Soc. Expl. Geoph., Tulsa, OK, 191-218.

Mitchell, A.R., and Wait, R., 1977, *The Finite Element Method in Partial Differential Equations*, London, John Wiley & Sons, 198pp.

Nabighian, M.N., 1979, Quasi-static transient response of a conducting half-space - an approximate representation, *Geophys.*, **44**, 1700-1705.

Nekut, A.G., 1987, Direct inversion of time-domain electromagnetic data (short note), *Geophys.*, **52**, 1431-1435.

Nekut, A.G., and Spies, B.R., 1989, Petroleum exploration using controlled-source electromagnetic methods, *Proc. of the IEEE*, **77**, no. 2., 338-362.

Nobes, D.C., Villinger, H., Davis, E.E., and Law, L.K., 1986, Estimation of marine sediment bulk physical properties at depth from seafloor geophysical measurements, *J.G.R.*, **91**, 14033-14043.

North, F.K., 1985, *Petroleum Geology*, Unwin Hyman, Boston, 631pp.

Oehler, D.Z., and Sternberg, B.K., 1984, Seepage-induced anomalies, "false" anomalies, and implications for electrical prospecting, *AAPG Bull.*, **68**, 1121-1145.

Orange, A.S., 1989, Magnetotelluric exploration for hydrocarbons, *Proc. of the IEEE*, **77**, no. 2., 287-317.

Ostrander, A.G., 1990, Structural mapping at the Tomera Ranch Oil Field using CSAMT: a case history, *Nevada Petrol. Soc. 1990 Fieldtrip Guidebook.*, 57-67.

Palacky, G.J., 1987, Resistivity characteristics of geological targets, in *Electromagnetic Methods in Applied Geophysics, Vol.1, Theory*, M.N. Nabighian *ed.*, Soc. Expl. Geoph., Tulsa, OK, 53-129.

Pearson, C., Murphy, J., and Hermes, R., 1986, Acoustic and resistivity measurements on rock samples containing Tetrahydrofuran Hydrates: laboratory analogues to natural gas hydrate deposits, *J.G.R.*, **91**, 14132-14138.

Shipley, T.H., Houston, M.H., Buffler, R.T., Shaub, F.J., McMillen, K.J., Ladd, J.W., and Worzel, J.L., 1979, Seismic evidence for widespread possible gas hydrate horizons on continental slopes and rises, *AAPG Bull.*, **63**, 2204-2213.

Spies, B.R., 1983, Recent developments in the use of surface electrical methods for oil and gas exploration in the Soviet Union, *Geophys.*, **48**, 1102-1112.

Spies, B.R. and Frischkneckt, F.C., 1991, Electromagnetic sounding, in *Electromagnetic Methods in Applied Geophysics, Vol.2, Applications*, M.N. Nabighian *ed.*, Soc. Expl. Geoph., Tulsa, OK, 285-425.

Sternberg, B.K., and Oehler, D.Z., 1990, Induced-polarization hydrocarbon surveys: Arkoma Basin case histories, in *Induced Polarization: Applications and Case Histories*, Fink, J.B, Sternberg, B.K., McAlister, E.O., Weiduwilt, W.G., & S.H. Ward *eds.*, Soc. Expl. Geoph., Tulsa, OK, 354-378.

Stoll, R.D., and Bryan, G.M., 1979, Physical properties of sediments containing gas hydrates, *J.G.R.*, **84**, 1629-1634.

Stoyer, C.H., and Greenfield, R.J., 1976, Numerical solutions of the response of a two-dimensional Earth to an oscillating magnetic dipole source, *Geophys.*, **41**, 519-530.

Strack, K.M., Hoerdt, A., and Wolfgram, P.A., 1991, Integrated electromagnetic and seismic methods for petroleum exploration, *Expl. Geop.*, **22**, 375-378.

Swift, C.M., 1987, Fundamentals of the electromagnetic method, in *Electromagnetic Methods in Applied Geophysics, Vol.1, Theory*, M.N. Nabighian *ed.*, Soc. Expl. Geoph., Tulsa, OK, 5-12.

Tissot, B.P., and Welte, D.H., 1978, *Petroleum Formation and Occurence*, Berlin, Springer-Verlag, 538pp.

Travis, B.J., 1987, TRIMESH: an automatic mesh generator for finite element programs, unpublished software.

Unsworth, M.J., Travis, B.J., and Chave, A.D., 1993, Electromagnetic induction by a finite electric dipole source over a 2-D earth, *Geophys.*, **58**, 198-214.

Vozoff, K., 1991, The magnetotelluric method, in *Electromagnetic Methods in Applied Geophysics, Vol.2, Application, Part B*, M.N. Nabighian *ed.*, Soc. Expl. Geoph., Tulsa, OK, 641-712.

Vozoff, K., Moss, D., LeBrocq, K.L., and McAllister, K., 1985, LOTEM electric field measurements for mapping resistive horizons in petroleum exploration, *4th ASEG conf.*, 309-312.

Wangsness, R.K., 1986, *Electromagnetic Fields*, New York, John Wiley & Sons, 587pp.

Ward, S.H., 1980, Electrical, electromagnetic, and magnetotelluric methods, *Geophys.*, **45**, 1659-1666.

Ward, S.H., and Hohmann, G.W., 1987, in *Electromagnetic Methods in Applied Geophysics, Vol.1, Theory*, M.N. Nabighian *ed.*, Soc. Expl. Geoph., Tulsa, OK, 131-311.

Webb, S.C., Contstable, S.C., Cox, C.S., and Deaton, T.K., 1985, A seafloor electric field instrument, *J. Geomag. Geoelectr.*, **37**, 1115-1129.

Webb, S., Edwards, R.N., and Yu, L., 1993, First measurements from a deep-tow transient electromagnetic sounding system, *Marine Geophys. Res.*, **15**, 13-26.

West, G.F. , Macnae, J.C., 1991, Physics of electromagnetic induction exploration method, in *Electromagnetic Methods in Applied Geophysics, Vol.2, Applications*, M.N. Nabighian *ed.*, Soc. Expl. Geoph., Tulsa, OK, 5-45.

Wolfgram, P.A., Edwards, R.N., Law, L.K., and Bone, M.N., 1986, Polymetallic sulfide exploration on the deep sea floor: The feasability of the MINI-MOSES experiment, *Geophys.*, **51**, 1808-1818.

Young, P.D., and Cox, C.S., 1981, Electromagnetic active source sounding near the East Pacific Rise, *Geophys. Res. Let.*, **8**, 1043-1046.

Young, R.A., and Lucas, J.E., 1988, Exploration beneath volcanics: Snake River plain, Idaho, *Geophys.*, **53**, 444-452.

Zienkiewicz, O.C., and Taylor, R.L., 1989, *The Finite Element Method, 4th ed., Vol. 1, Basic Formulation and Linear Problems*, London, McGraw-Hill, 648pp.